CO_2 Sequestration: The effect of carbonate dissolution on reservoir rock integrity

Kristian Engen Eide

Kristian Engen Eide

CO$_2$ Sequestration: The effect of carbonate dissolution on reservoir rock integrity

Rijswijk, The Netherlands, 25/04, 2012

NTNU
Norwegian University of
Science and Technology

Preface

The current report is the Master's Thesis of Kristian Engen Eide. The study is a result of a 7 months internship at Shell Research Center in Rijswijk, The Netherlands. The report was written as the final thesis of 5-year Master of Science Degree in Reservoir Engineering. The report addresses some of the important questions in terms of CO_2 storage, and the long-term effects that this has on the reservoir integrity. Established experimental protocol and performed experiments at Shell Research Center have enabled me to investigate alteration of rock mechanical and acoustic properties due to acid exposure.

I would especially like to acknowledge Sell Global Solution for allowing the use of allowing the use of laboratories and material, together with all the resources that were invested in the current study.

A special appreciation is directed to Andreas Bauer for supervising me throughout the process, Arjan van der Linden for assisting with laboratory work and the other co-workers at Shell Global Solution for performing other services required for the study.

I would also like to show my appreciation to Axel Makurat, Rune Martin Holt and NTNU for making it possible to make the internship as a part of my Master's Thesis. Cor Kenter should also be acknowledged for his effort of putting me in contact with the proper people in Shell.

April 25th 2012, Trondheim

Kristian Engen Eide

Abstract

Since the environmental focus only becomes stronger and stronger in today's society, industries like the oil and gas sector face some difficult challenges. Being the primary industry for CO_2 production in the world requires them to invest a lot of resources in finding alternative methods to prevent venting to the atmosphere. Governments around the world are initiating measures and imposing taxes in order to compel the companies to do this.

Injecting CO_2 for EOR purposes has been around for several decades and is very well known to the industry. However, in more recent years, the idea of injecting CO_2 for storage has become a promising method. Currently, there are several ongoing Carbon Capture and Storage (CCS) projects around the world, with more to come. The idea is to inject the CO_2 into depleted reservoirs of aquifers, allowing different trapping mechanisms to react with the CO_2 and prevent it from reaching the surface.

CO_2 features the ability to form an acid when dissolved in brine. At high pressures, the acid is very aggressive and could induce a strong dissolution reaction with carbonates. This could lead to severe consequence in a CCS project since carbonates are common material in oil and gas reservoirs. Dissolving the reservoir rock could increase the porosity. The fact that the rock's stiffness and strength are strongly related to its porosity implies that alteration of the porosity could have a softening and weakening effect on the stiffness and strength in terms of softening and weakening. In addition to the porosity increase, other effects, such as chemical effects, can also be present, contributing to further alteration of the rock.

In the assessment of CCS projects, geomechanical modeling requires input data describing the effects that the acid has on the rock mechanical properties. A correct representation of the reservoir requires a comprehensive understanding of every aspect. This requires a lot of research and studies on the rock mechanical alteration.

Simulating subsurface processes in the laboratory is the first difficult challenge that has to be solved. Wormhole formation is dominates the dissolution pattern when acidic solutions are injected into core samples, but this is considered to be less representative for the reservoir processes, as a more homogeneous dissolution is assumed. The current project has successfully established that injecting a retarded acid allows full saturation before reaction takes place. Pre and post CT scanning has been performed together with special core analysis and mercury injection capillary pressure (MICP).

A significant increase in porosity is seen in the tested rock material, Euville limestone, as a result of the treatments using retarded acid. After 6 treatments, an increase of 3 porosity units is observed. The study has emphasized the effect that chemical dissolution has on the rock mechanical properties, in terms of stiffness and strength. Failure tests have been performed for determining the Mohr – Coulomb failure envelope after a certain degree of alteration.

Beside from the porosity increase, it also follows that the acid exposure also affects the stiffness and strength. A significant change is observed in the Young's modulus, bulk modulus, shear modulus and Poisson's ratio, having an average change of 9.4 ± 3.6 GPa, 1.8 ± 2.7 GPa, 4.5 ± 1.2 GPa and 0.12 ± 0.04, respectively, after 6 acid treatments. The failure line, for the treated rock, shows a clear reduction in strength with a 77 % decrease in the friction angle and a 26 % decrease in uniaxial compressive strength.

Intuitively, since porosity, stiffness and strength are closely related, most of the effect is caused by the porosity increase. However, there are indications of that also other effects are causing the evolution for the stiffness parameters to deviate from the stiffness–porosity trends.

The study has also approached the assessment of rock alteration from an acoustic velocity point of view. Increasing the porosity also results in reduced P- and S-wave velocities, as expected. Deviation from the porosity trend does, however, also suggest, that other effects influence the acoustic properties, in addition to the porosity increase. An evaluation of the dynamic moduli shows that fluid substitution is only effecting the measurements to a minor extent.

The established protocol is necessary for further studies of the rock mechanical alteration that CO_2 induces as it is injected into the reservoir. Our findings are important steps toward implementing knowledge on how the reservoir is affected by CO_2 injection into geomechanical models and seismic monitoring. Being able to predict possible consequences and outcomes as well as monitoring of the reservoir, are very important tools for CCS projects and could potentially be the key to the license to operate.

Contents

---

1.   Introduction

As the world continues to develop, and the third-world countries catch up with the western world's standard of living, energy demand is climbing to new heights. For the time being, the only sources of energy that are capable of meeting these demands are fossil fuels: the amount of energy they deliver is far greater than that of renewable energy sources. Despite huge investments throughout the world in developing renewable energy, oil and gas will continue to be one of the dominating sources for several decades.

The controversial consequence of burning fossil fuels is the increase in CO_2 emissions. The focus on Green House Gas emissions is enhanced along with the increasing production of CO_2. Venting the CO_2 to the atmosphere is by far the easiest method of disposing of CO_2. The result could be global warming followed by severe consequences such as extreme weather and rising sea levels. Finding alternative ways of handling the CO_2 is therefore a major area within research and the oil companies are investing a lot of resources in this topic.

One of the most promising and already applied methods is to inject and store the CO_2 in aquifers and depleted reservoirs, also known as Carbon Capture and Sequestration (CCS). The idea is that various trapping mechanisms prevent the CO_2 from reaching the surface and venting to the atmosphere. In theory, injecting a gas such as CO_2 into a depleted reservoir should be simple. The reservoir has already trapped oil and gas for millions of years. In reality, this is not as simple as it sounds due to the number of risks related to subsurface injection of CO_2.

CO_2 features the ability to form an acid when dissolved in water. At the surface, its solubility is low and the solution is not aggressive. At elevated pressures and temperatures, solubility and the aggressiveness become significantly enhanced. Acids are known to dissolve carbonates, hence the CO_2 saturated brine has the potential of dissolving the reservoir rock as it is injected. The reaction is extremely fast, so most of the acid would be neutralized close to the injection well before settling in the reservoir.

In terms of CO_2 storage, long-term consequences are the aspects of greatest concern. Dissolution of the rock implies an increase in porosity, to which both stiffness and strength are strongly related. Altering the stiffness and strength could have severe consequences in terms of (i) reservoir compaction and surface subsidence, (ii) induced seismic activity and (iii) leakage of CO_2 to the surface.

In the assessment of CCS projects, geomechanical models require knowledge and input about the alteration of the reservoir rock caused by the injected CO_2. The current project aims to find an experimental protocol simulating the long-term subsurface processes. It is therefore necessary to achieve homogeneous alteration of the rock in the laboratory. Further on, based on the experimental protocol, an assessment of the effect that the acid exposure has on the rock mechanical properties will be carried out. The alteration is also assessed from an acoustic velocity point of view because reservoir surveillance requires this understanding. Reservoir surveillance is important in terms of the "license to operate" needed for CCS projects.

The following workflow for assessing CCS projects, and also other projects requiring similar modeling, shows the significance and importance of the current study:

1. Reservoir simulation + geochemical modeling: how much carbonate is dissolved (not part of present study).

2. Determine dependence of rock stiffness and strength on amount of carbonate dissolved.
3. Use geomechanical model to assess reservoir and caprock integrity (not part of present study).

The study starts of by presenting a general overview of Carbon Capture and Sequestration in Chapter 2. The overview addresses some of the challenges that the world faces in terms of CO_2 emissions and the consequences that could follow. In addition, a brief introduction to the technology and theory is given, together with the current status of worldwide CCS projects.

The basic theory on carbonate and acid interaction is addressed in Chapter 3 together with a brief introduction to the rock mechanical properties, and acoustic velocity and porosity correlations. Chapter 4 highlights some of the work done on this topic in the past, followed by an overview of the challenges related to rock mechanical testing in Chapter 5. The intention of this Chapter is to explain, and emphasize the uncertainties related to experimental measurements on core material in the laboratory.

The experimental setup and protocol are presented in Chapter 6 together with some of the procedures used in special core analysis. Experimental results can be found in Chapter 7, whereas a thorough discussion and assessment of the results are made in Chapter 8. Finally, a conclusion and an outlook are presented in Chapter 9.

2. CO₂ and carbon sequestration in general

2.1 Why carbon capture and storage?

The climate has changed a lot over the last decades. Global warming has gone from being a term used only by the specialists to become a well-known phenomenon among the general public. There is no doubt that the average temperature on the earth has risen and that the overall weather has become more extreme. However, scientists are somewhat divided on what the cause could be are rather divided among the scientists. The media has chosen to focus on blaming mankind and people's lifestyle as the primary cause. One cannot argue on that the lifestyle of the western world, and now the following third world, is imposing demands and affecting the environment significantly. Severe climate changes have occurred several times throughout the Earth's history, and so the big question is whether the change that we are experiencing now is a part of a natural change or something that mankind is causing.

In general, people and nations have become more and more focused on environmental issues. This is a consequence of blaming mankind for what is happening with the climate. Research claims that the significant increase in greenhouse gas (GHG) emissions is triggering the global warming. The primary greenhouse gases are water vapor (H_2O) and carbon dioxide (CO_2) together with methane (CH_4), nitrous oxide (N_2O) and ozone (O_3). It is CO_2 resulting from fossil fuel burning that is drawing much of the attention with respect to pollution and enhanced global warming, as this leads to an increase in global temperature and concomitantly to sea level rise and extreme weather. The emission of CO_2 has increased significantly and the increase is ongoing. Annual emissions between 1970 and 2004 have grown by 80%, going from 21 to 38 gigatons (Gt) [1]. In the worst case, *i.e.* in a world with high population growth and slow economical and technical development, an annual CO_2 emission of close to 140 gigatons [2] is predicted (See Figure 1, scenario A2). In order to curb the predicted CO_2 emission trends, it is important to reduce anthropogenic CO_2 emissions. One possible option is via Carbon Capture and Storage (CCS), which consist of capturing of CO_2, transporting it to a suitable storage location and storing it by various methods.
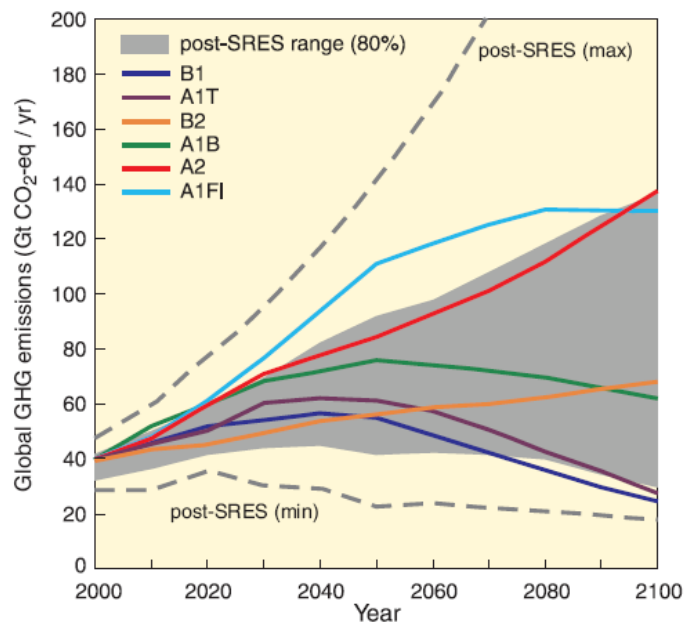

Figure 1: Shows the predicted CO2 emissions based on different world development scenarios. Worst-case scenario, A2, corresponds to a heterogeneous world with high population growth and slow economical and technical development [1].

What concerns the experts is not the fact that the climate is changing, because this is, as already mentioned, a natural process. In a recent publication by the Intergovernmental Panel on Climate Change, several aspects regarding climate change are highlighted. Here, it is clearly shown that it is the changes in the trends that are of concern. Especially the temperature change is quite severe. The increase in average temperature around the arctic poles is even more severe than elsewhere, resulting in a significant decrease in the ice extent. The arctic ice extent has decreased with as much as 2.8% per decade since 1980 [1]. Temperature changes are also affecting the sea level, which rose at an average rate of 1.8mm annually from 1961 to 2003, while between 1993 and 2003 the annual average increase was 3.8mm [1]. Whether this trend is a decadal exception or a picture of the longer-term trend is uncertain. The overall frequency of extreme weather has also increased significantly, and is noticed all around the world. The climate change is not only affecting the weather, but also agriculture and the earth's biological system in which the natural living patterns of different animals are disturbed. There is, however, great uncertainty to whether these changes are mainly caused by the increased CO_2 emissions. Variables such as the meridional overturning circulation (MOC) could have a major influence as well.

Although there are many uncertainties regarding what is causing the changes in the climate, comparing the trend in emissions with the climate observations strongly suggests that there is a relationship. However, regardless of whether CO_2 emissions are causing the dramatic changes seen in the climate, reducing emissions is essential for the environment and is something that should be taken seriously. Continuing the current trend without applying any countermeasures would have severe consequences thus working towards a low-emission society should therefore be a high priority goal. Global leaders agreed on a maximum of a 2 ℃ increase in Copenhagen 2010, but the road towards achieving this is still a long one, given that the IEA World Energy Projection for 2010 predicts an increase of 3.5 ℃ by 2035 based on today's trend. The future does, however, look brighter with regard to reducing the emissions of CO_2 to the atmosphere. Both the industry and governments worldwide are taking measures, and we see a significant increase in the number of carbon capture and storage projects. This will be addressed in more detail in Sections 1.4 and 1.5.

Fossil fuels are considered to be the easiest source of energy, making up 80% of the current energy demand, as of 2010 [3]. They are a non-renewable source that when burned, significant amounts of energy is released per unit weight, making them so attractive as an energy source. Today's society requires huge amounts of energy and together with the rapid development of the third world, future demands will be far from decrease. An extreme development has been seen over the last couple of decades, with explosive increases in the demand of electricity and in the number of cars on the roads. Currently, renewable energy sources and technology are far from being capable of meeting present and future demands. Burning coal and gas is therefore the primary source for acquiring electric energy, while oil is less used to generate electric power. Despite not being used as a primary source for electricity, oil plays a significant role. We are surrounded by consumer products that require oil in one way or another, everything from cars to make-up. Thus a life without oil and gas is unimaginable.

Such a high value energy source does not come without a cost. CO_2 is not only a bi-product of the combustion reaction, but constitutes a certain fraction of the crude oil composition as well. Carbon dioxide is already a part of the natural carbon cycle in the earth's atmosphere.

CO_2 from fossil fuels is considered not to be a part of the natural cycle. Releasing the CO_2 into the atmosphere disturbs the natural cycle causing severe environmental consequences. It is believed that the increase seen in CO_2 emissions over the last decades is causing the climate changes that the earth is facing. As the primary source of CO_2 is coming from oil and gas, the oil industry is being considered as "the big bad wolf" in terms of CO_2 emissions. Thus, a lot of pressure is therefore put on the companies in order to find alternative ways of reducing the emissions.

2.2 How to capture and store CO_2?

Carbon capture and storage (CCS) is the term for describing the technologies used in the 3-stage process of capturing, transporting and storing carbon in the form of CO_2. The capture and transportation technology is more developed than what applies for storage. The ability to capture CO_2 is quite high with the capability of capturing 80 to 90% of power plant flue gasses [4] with the current technology. Many questions around the storage part are still to be answered, especially regarding how to locate suitable storage sites and the consequences of long-term storage. In terms of CO_2 emission reduction, CCS could contribute with a 20% reduction in global annual CO_2 emissions, according to the International Energy Agency. In addition, CO_2 is used for enhanced oil recovery (EOR), though the main goal for EOR is not to store CO_2 over geological timescales, as it is for CCS, but rather to increase oil production. Overall, CCS is an area that has a lot of potential for CO_2 emissions reduction and efforts should be devoted towards further development.

2.2.1 Capture

CO_2 can be captured either directly from the industrial process stream (flue gas), during pre- or post- combustion processes, or by oxy-firing. Pre-combustion capture involves partial combustion producing hydrogen and CO_2. Although this technology already exists on a commercial scale, complete integration in full-scale facilities is still a challenge. Post-combustion capture involves capturing the CO_2 from the flue gas after fossil fuel combustion. The challenge with this technology lies in up-scaling and integrating into commercial process plants. Oxy-firing involves the use of pure oxygen instead of air in the burning process. The flue gas is made up by mostly CO_2 and water and can therefore be dewatered and compressed for storage as it is.

Different techniques are used in the various capture situations mentioned above. There are three main techniques of separating CO_2 from the flue gas [4]: (i) introducing a liquid- or solid-based sorbent that is capable of absorbing the CO_2, followed by regeneration of the sorbent leading to segregation of CO_2 and sorbent, (ii) using membranes allowing the selective permeation of gas, (iii) distillation of a liquefied gas stream, following a series of compression, cooling and expansion steps to separate the different components.

The large-scale applicability and the process cost are the key factors determining whether the technique is suitable or not. At present, using a sorbent is the most frequently used technique, such as the use of amine to absorb the CO_2 from the gas produced at Sleipner in Norway. This is done as the produced gas contains up to 9% [6], while sales agreements states that the delivered product should not exceed more than 2.5 mol% of CO_2.

2.2.2 Transport

This area of CCS technologies builds upon the knowledge and technology obtained for the transportation of natural gas (LPG – liquefied petroleum gas, LNG – liquefied natural gas) and is therefore well-understood. In addition, large quantities of CO_2 for enhanced oil recovery purposes have been transported to oil field sites since the early 1970s. For example, US pipelines are capable of safely transporting 50 million tons of CO_2 a year. Pipelines are the most practical solution for moving large quantities of CO_2 from power plants to near-by storage sites. Other options for transportation are trucks and ships, for example.

2.2.3 Storage

The applicability of CO_2 alone is rather limited. However, there are some areas in which CO_2 can be used. CO_2 injection has been and still is done for various reasons, most frequently reasons are both for enhanced oil recovery (EOR) purposes. These are: (i) Injection by alternating between water and gas, WAG injection, for increased reservoir pressure and a more effective sweep process than can be achieved by only injecting water or gas, [7] (ii) Acid treatment [8], exploiting the feature of that CO_2 dissolves in water to form an acid. Acidic solutions are known to dissolve carbonates in which injection induces the formation of high permeable channels, known as wormholes, that penetrates the formation close to the well. These wormholes increase the permeability around the well, thus reducing the skin in the damaged zone. A more detailed study on wormholes and reactive flow in general is discussed in the project by Kristian Eide: '*CO_2 induced calcite dissolution in Euville carbonate rock: Formation of wormholes.*'

Injecting CO_2 for EOR purposes is not a permanent solution for storing CO_2. Firstly, although the condition of having an oil reservoir is that the cap-rock is sealing and we have a trap, leakage of the injected CO_2 is still possible. Secondly, the likelihood of re-producing the gas together with the oil is extremely high, thus the CO_2 is only recycled. More advanced measures and considerations are needed in order to achieve more permanent storage possibility.

Currently, four different methods for storing CO_2 are proposed [9]: biological, mineral trapping, deep ocean disposal and injection into geological formations. Biological disposal suggests trapping CO_2 by relying on the CO_2 uptake by forests and algae. However, this is not considered to be a permanent storage option as the CO_2 is released again once the organism dies and decays. Mineral trapping is based on allowing CO_2 to react with minerals and brine to form stable carbonates. In order to liberate the cations, necessary for reaction, from the minerals offer, large quantities of acid or base are needed, making this an environmentally unfriendly and expensive method. Deep ocean disposal in the form of CO_2 hydrates is a limited option because the CO_2 can only be stored for a few hundred years [10], and the poor knowledge on hydrate formation dynamics [11]. Due to the potential environmental effects (ocean water acidification) deep ocean disposal is not considered on a large scale.

Injection into geological formations is by far the most promising method for long-term storage of CO_2. The different trapping mechanisms, both physical and chemical, are all mainly based on immobilizing CO_2. Depleted reservoirs, deep saline aquifers and coal seams are some of the most preferable and suitable storage sites, especially the latter. The idea is to inject CO_2 into low-permeable formations so that migration towards the surface is slow, allowing enough time for the trapping mechanisms to prevent the CO_2 from reaching the surface. The challenge is that injectivity requires a certain permeability and to locate reservoirs fulfilling both criteria is difficult. One option is to enhance the injectivity near the well by stimulation. Physical trapping, or static trapping, includes stratigraphic and structural trapping and implies that there are

structural seals preventing leakage of CO_2. Lateral seals can be faults whereas an impermeable caprock could seal the roof. Anticlines are also suitable for physical trapping. Other trapping mechanisms are [12], [4]:

- Residual-gas trapping in the pore space (physical),
- Solubility trapping in which the CO_2 no longer exists as a single phase and so there is no migration caused by buoyancy effects (chemical),
- Mineral trapping by mineralization (chemical),
- Absorption onto mineral surfaces (chemical),
- Absorption onto organic material (chemical).

The effectiveness and security of the geological storage is a combination of the different mechanisms and the timescale and is summarized in Figure 2 [4].

The potential of geological storage is great, and it is stated that over a time scale of thousands of years, aquifers are capable of eliminating over 90% of initially injected CO_2 [9]. Although the theory is understood, finding the fields is time consuming. A lot of work is still to be done, such as investigating long term effects and consequences that CO_2 could have. However, based on how far we have come today, the future looks promising with respect of permanent solutions for storing CO_2 and preventing pollution of the environment.
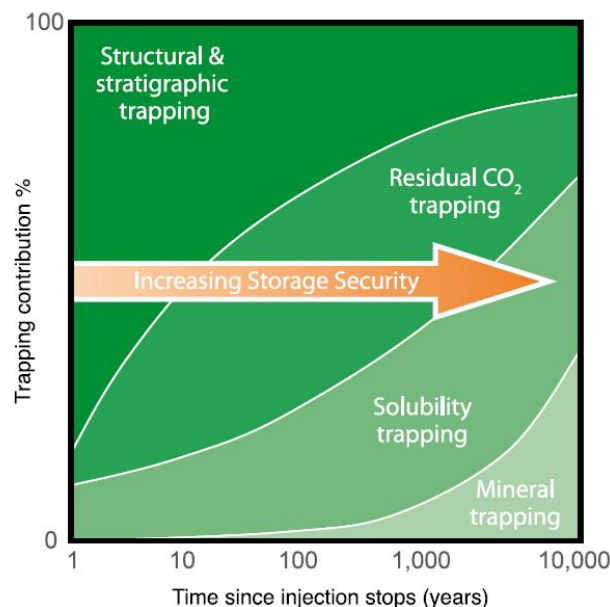
Figure 2: Security and effectiveness combining different trapping mechanisms. Large timescale mechanisms are most secure but these have also less storage potential [4].

2.3   Challenges and risks of carbon capture and sequestration

Although the use of capturing techniques has been around for a long time, issues are still faced as new technology is developed. Certain risks are associated with the different capturing techniques. Firstly, a lot of waste is produced, both solid and fluid. Secondly, the presence of impurities in the CO_2 separated stream could affect transportation systems and have a potential health and environmental impact. We know that costs are important in the choice of capture technology. CO_2 projects require certain cost efficiency in order to be feasible. Choosing less

costly techniques and technology might enhance the possibility of associated risks, such as having a more impure CO_2 stream, leakage from the system, and a greater production of waste. Nevertheless, new and more reliable as well as cost-efficient technologies are advancing, thereby steadingly improving the capture process even more.

Transport of CO_2 is safe and reliable due to the long application history. However, issues with the capturing process might reflect over to the transportation process, inducing risks here as well. Pipe failure is one of the primary risk factors but the technology on pipeline construction has reduced this factor significantly. The frequency of failure-incidents is very low. One may not expect that water is one of the most severe impurities. Wet gas leads to pipe corrosion, hence dehydration is essential in order to prevent this. As the amount of CO_2 needing to be handled in the future only grows, more pipelines will be required. Finding secure routs becomes harder, especially through highly populated areas. More and longer pipes also imply enhancement of the risk factors. Cleaning is already a challenge; however, this challenge will only grow with a growing pipe system. One also has to consider the possibility of military conflicts when constructing pipeline systems. Placing them in areas with a lot of political instability is a risk that can have significant consequences, *i.e.* sabotage and as a source of blackmail.

Storing CO_2 sounds rather simple, but a number of issues and challenges must be considered and dealt with, all the way from initial injection to long-term effects.

Though depleted reservoirs and aquifers are abundant worldwide, locating a suitable storage site remains a challenge. Stefan Bachu *et al.* [9] proposes that in order for a location to be suitable for storage purposes, certain conditions must be fulfilled:

- A sealing unit should overlie the reservoir/aquifer, which should also have trapping capabilities.
- The reservoir/aquifer top should be at more than 800 m depth.
- High porosity and lowest possible permeability should be present. Higher permeability is favorable close to the injection well.
- Storage location should be close to the capture site for economical reasons.

Further on, the main risks and challenges other that site localization are escaping CO_2 and pressurization of the formation that follows from the injection. The latter is mostly associated with aquifers and reservoirs that have not been depleted from their initial *in situ* pore pressure. Increasing the pore pressure increases the stress beyond *in situ* conditions in which failure could be induced.

Long-term effects that might follow from storing CO_2 are less known and the potential consequences could be severe. Dissolving minerals in the formation, due to of the acidic solution that CO_2 forms with brine, could affect the formation integrity altering the strength and stiffness of the rock. This enhances the likelihood of induced compaction and failure of the formation with induced tectonic activity, formation collapse and subsidence as some of the consequences.

There are also a number of challenges related to the post-injecting period. Monitoring, the distribution and movement of the CO_2 subsurface is important to ensure that no leakage is occurring. Also, reservoir pressure and stress changes are of interest. Stress changes are more difficult to monitor, however, by understanding the relationship between changes in acoustic properties and stresses, seismic monitoring is one way of assessing the changes that are occurring. Storing subsurface is quite costly and varies a lot depending on conditions such as the type of storage site, *i.e.* depleted reservoirs or aquifers. Depth plays a role as well as the pre-

existing data. In view of the steps in a CCS project, expenses are significant. As will be discussed in the next section, companies require a "push" or an economic reason in order to engage in a costly CCS project. Financial support by collaboration with other companies or governments could also be an important factor for initiating large-scale projects.

2.4   Current CCS status

Although CO_2 injection for enhanced oil recovery and the idea of CCS have both been around for about 80 years, with small-scale demonstration and research projects, it is not until recent years that large-scale *(1)* industrial CCS projects have been commenced. Sleipner in Norway is considered to be one of the pioneering CCS projects as well as being the first offshore facility for CO_2 injection and storage. The project became operational in 1996 with a total of 20 million tons of CO_2 planned for injection. Currently *(2)*, eight projects are considered to the leading CCS projects, of which two are located in Norway [13] (Table 1).

In addition, the Global CCS Institute reports 74 large scale projects, of which 14 are either operating or under construction [13]. Current annual storage capability is around 35.4 million tons of CO_2. This is roughly equivalent to Norway's annual emissions [13]. It is also a clear indication of high focus on CCS research worldwide, with a reported total of over 200 small-scale CCS demonstration and projects as of April 2010 [3].

1) *Large scale projects are here defined as projects capable of storing more than 800 000 tons CO_2 annually for a coal-based power plant and 400 000 tons for other types of facilities.*
2) *Current status is based on 2011 numbers provided by The Global Institute of CCS. See reference [13].*

Table 1: List of current large-scale operating CCS projects worldwide [13].

Project name	District	Country	Industry	Capture type	Storage option	Annual capture volume [Mt]	Year of operation
Val Verde Natural Gas Plants	Texas	United States	Natural gas processing	Pre-combustion	EOR	1.3	1972
Enid Fertilizer	Oklahoma	United States	Fertilizer production	Pre-combustion	EOR	0.7	1982
Shute Creek Gas Processing Facility	Wyoming	United States	Natural gas processing	Pre-combustion	EOR	7	1986
Sleipner CO_2 Injection	North Sea	Norway	Natural gas processing	Pre-combustion	Offshore formation	1	1996
Great Plains Synfuels Plant and Weyburn-Midale Project	Saskatchewan	Canada	Synthetic natural gas	Pre-combustion	EOR	3	2000
In Salah CO_2 Storage	Wilaya de Ouargla	Algeria	Natural gas processing	Pre-combustion	Onshore formation	1	2004
Snøhvit CO_2 Injection	Barents Sea	Norway	Natural gas processing	Pre-combustion	Offshore formation	0.7	2008
Century Plant (formerly Occidental Gas Processing Plant)	Texas	United States	Natural gas processing	Pre-combustion	EOR	8.5	2010

2.5 Working towards reduced CO_2 emissions

From the brief overview of CCS in general and the current status, we see that a long way is still to go in order to reach the set goals of reducing emissions so that a maximum of a 2 ℃ increase in average temperature is met. However, new measures are proposed and implemented more frequently than before, and we also see a strong trend of increased international collaboration between industrial companies and governments.

An example of international collaboration is the adoption of The United Nations Framework Convention on Climate Change in 1992, entering into legal force in 1994 [14]. As of 2011, 194 countries have agreed on and committed to help with the greenhouse gas challenge that the world faces. Another example that has a more fixed goal is the 1997 Kyoto Protocol that was adopted by 55 countries in 2005. The protocol implies that 37 industrial countries should reduce the total CO_2 emissions by more than 5% with respect to 1990 levels by 2012 [15]. The US is still not part of this agreement. The United Nations Framework Convention on Climate Change (UNFCCC) is still working on a new agreement for the time following after 2012.

Each respective country is responsible for finding ways to contribute to the reduction of CO_2 emissions by adopting national measures. An effective way used by governments to increase CO_2 focus is by applying tax on CO_2 emissions (so-called CO_2-tax). The Norwegian government is a leading example of an active government working on increasing CO_2 focus and emissions reduction by companies. In 1991, a new tax law was adopted by Norway, implying that any company that releases CO_2 by either burning oil or releasing natural gas, to the atmosphere on the Norwegian continental shelf will be imposed a fee [16]. As of 1st of January 2012, this fee is 0.06€ *(1)* per Sm^3 released natural gas or per liter oil burned [17]. The intention of this law is to motivate companies to engage in research on CCS. The Sleipner CCS project was initiated by Statoil ASA because of this law, showing the effect that additional tax law may have. Norway has already two large-scale CCS projects operating, with the third one, Mongstad, following in the near future. The Norwegian Petroleum Directorate has also published an atlas describing possible subsurface storage locations for CO_2 in the Norwegian part of the North Sea. The atlas shows the potential of storing up to 70 gigatons of CO_2 in this area. These achievements are a result of both government and industry collaboration.

Sharing CCS knowledge and technology accelerates developments, hence the initiative taken by the European Commission in sponsoring and organizing the world's first network of demonstration projects is therefore extremely important [18]. Not only is a strong collaboration seen between nations worldwide, but also between companies. The CO_2 Capture Project® is an award-winning partnership between seven major energy companies with a common goal of advancing CCS technology. Governments such as the U.S. Department of Energy, Norges forskningsråd and the European Union are contributing [19].

1)   *Based on an exchange rate of 1.00€ = 7.90 NOK*

3. Theory

3.1 Acid dissolution of carbonates

Neutral water can only to a very small extent, dissolve carbonates. Acidic solutions however, are capable of dissolving significantly more, depending on the strength of the acid. In pure water, the dissolution reaction occurs according to the following equation:

$$CaCO_3 \rightleftarrows Ca^{2+} + CO_3^-$$ (1)

The equilibrium (*i.e.* how far to the right the reaction will go) is determined by the solubility constant or the equilibrium constant. Adding an acid to the water will give a reaction according to:

$$CaCO_3 + H^+ \rightleftarrows Ca^{2+} + HCO_3^-$$ (2)
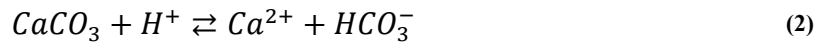
Calcite is here used as an example, but similar reactions occur with other carbonates such as dolomite etc. as well. From equation (2), we see that the acid plays an important role. As some $CaCO_3$ dissolves, the H^+ reacts instantaneously with the CO_3^{2-}. This will, according to Le Chatelier's principle [20], drive the equilibrium to the right, hence the significant increase in the dissolution capability. The strong effect of adding acid is also reflected in the equilibrium constant, which for reaction 2 is of an order of 10^9 or higher [21].

CO_2 features the ability to dissolve in brine and forms an acidic solution according to [22]:

$$CO_{2(g)} \rightleftarrows CO_{2(aq)}$$ (3)

$$H_2O + CO_{2(aq)} \rightleftarrows H^+ + HCO_3^-$$ (4)
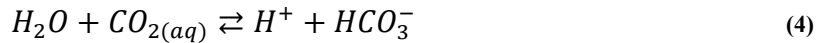
In contact with carbonates, this will result in enhanced dissolution. This feature is particularly exploited in EOR projects, but is also of significance with respect to CCS projects.

There are three different dissolution patterns seen as a result of the interaction between carbonates and acidic solutions. These are compact dissolution, wormholing and uniform dissolution. The dominating pattern depends on several factors, but is especially dependent on the ratio between the advective and the diffusive transport rates, and the ratio between the chemical reaction rate and the advective rate. Two dimensionless numbers are frequently referred to in reactive transport studies. The Péclet number (*Pe*) defines the first ratio, while the Damköhler number (*Da*) defines the latter and is expressed by [23]:

$$Pe = \frac{vL}{D}$$ (5)

$$Da = \frac{AkL}{\varphi v C_{eq}}$$ (6)

Here, v is the Darcy velocity, L is the characteristic length, D the diffusion constant, A the surface area of the grains, φ the porosity and C_{eq} the concentration at equilibrium. The latter, in the case of calcite-brine interaction, is the equilibrium concentration of calcium. These dimensionless numbers can be used for determining the dominating dissolution regime in a particular situation. The dissolution patterns can be graphically presented in a Péclet-Damköhler plot, seen in Figure 3 [23].
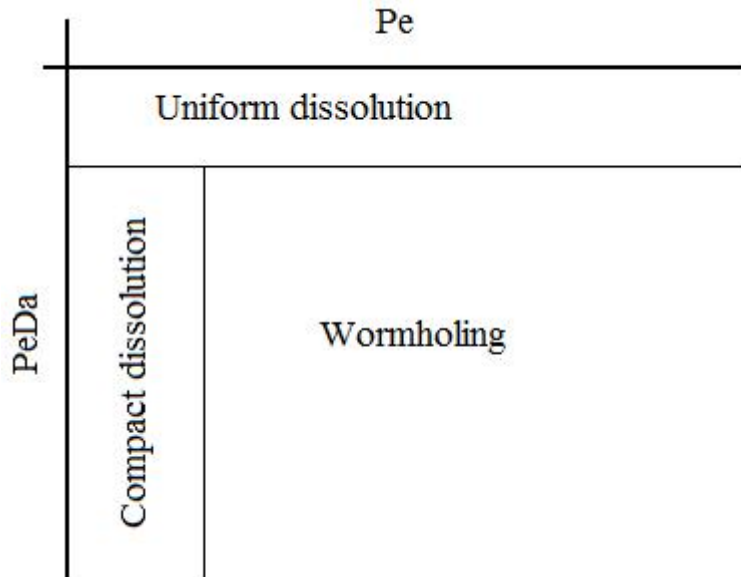
Figure 3: Péclet - Damköhler plot, graphically illustrating the regions where each respective dissolution pattern is dominating.

The boundaries between the regions are not definite exactly. However, a system with a Péclet number less than unity is normally dominated by a compact dissolution pattern, whereas very high Péclet numbers often result in systems with uniform dissolution. In between, we have wormholing, which also is the most frequently observed dissolution pattern in experiments and in the field close to the injection well. Wormholes are highly permeable channels, thus the applicability for EOR is great, especially in the acid treatment of wells [24]. Uniform dissolution is hardly ever seen in experiments with the exception of cases where uniform dissolution is intentionally imposed. From the definitions above, we see that rates play a significant role. Unrealistically high flow rates in conjunction with low reaction rates are necessary in order to achieve uniform dissolution. Other methods are required in order to achieve this dissolution pattern in the laboratory. I refer to Eide`s project [21], '*CO_2 induced calcite dissolution in Euville carbonate rock: Formation of wormholes*', for further reading on the reactive transport associated with carbonate-acid interaction.

The current project aims to stay in the uniform dissolution regime, located in the upper left region of Figure 3.

3.2 Reservoir rock and CO$_2$ interaction

As described above, CO_2 dissolves in water, forms an acid and reacts with carbonates. This reaction is considered to be very fast, thus the acidic brine will become buffered almost instantaneously. As discussed in Chapter 2, CCS projects inject CO_2 for geological storage. Saline aquifers and depleted reservoirs, both often consisting of carbonates, are preferred storage

formations. This introduces the issue that CO_2 could enhance the dissolution of the reservoir, causing severe alteration of its integrity.

During injection, different zones will emerge around the well depending on the saturation state [25]. These are graphically illustrated in Figure 4. Closest to the well, the concentration of gas is very high, resulting in a gas saturated zone. A gradual increase in the fraction of acidic brine is seen, constituting the transition zone. In this zone, most of the acidic brine is interacting with the reservoir formation, resulting in a declining acid strength as the flow continues outwards into the reservoir. The outer boundary of the transition zone is characterized as the point at which only a negligible amount of acid is left in the solution. The outer zone, *i.e.* the far field region, is therefore expected to consist of buffered brine with limited formation-acid interaction because of the equilibrium obtained in the transition zone.
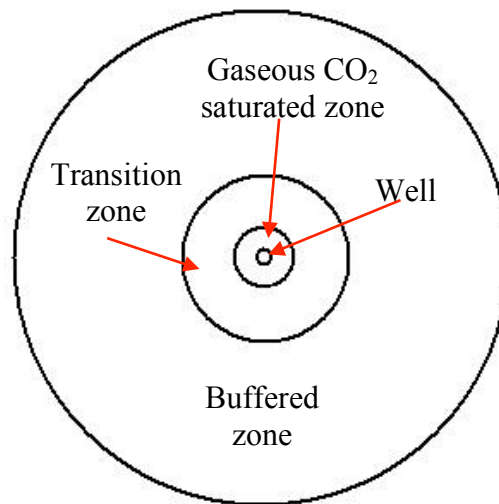
Figure 4: Different zones emerge during CO_2 injection in a CCS project.

Having a buffered solution in the reservoir gives reason to believe that no further dissolution will occur. However, disturbances in the equilibrium could result otherwise. Factors that could cause disturbances in the equilibrium are temperature changes. In addition, reactive transport is necessary in order for a dissolution reaction to occur [21]. Migration of fluids within the reservoir can occur due to gravity difference in fluids and thereby induce reactive transport. Diffusion and temperature gradients within the reservoir are also the driving mechanism for reactive transport in such reservoirs.

Precipitation is also something that can occur in the reservoir. This reaction can be described by reversing equation (2).

$$Ca^{2+} + HCO_3^- \rightleftarrows CaCO_3 + H^+ \tag{7}$$
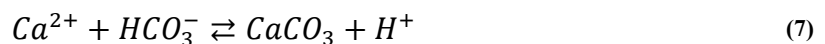
Acid is formed, thus the brine becomes more acidic. Reactive transport results in migration of the acidic brine, causing dissolution somewhere else in the reservoir. These reactions are slow, and the consequences are therefore associated with the long-term effects that CO_2 storage might have on the reservoir. It is especially the changes in porosity, stiffness and strength that are of main interest. The extremely slow flow rates puts us in the top left corner of the Péclet-Damköhler plot, namely in the homogeneous dissolution regime, Figure 3.

Studying these effects in the laboratory requires samples that are homogenously altered in order for the studies to be representative of the far field region. However, this is hard to achieve because injecting an already acidic solution will result in either compact or wormhole dominated dissolution pattern [21]. One has to find a way of placing the acid inside the sample before reaction takes place to avoid these patterns. Using a normal acid is therefore not possible due to the high reaction rate, unless one is able to inject with such high velocity that the placement is considered instantaneous. This requires unrealistically high rates. Another option is the use of a retarded acid, which is an acid with reduced reactivity. Various factors are control the reactivity, depending on the type of acid. Heating is a common factor, implying that the acid is not actually turned into an acid before reaching a certain temperature level.

3.3   Rock mechanical properties

3.3.1   Stiffness

Most dense and hard rocks are considered to be linear elastic, meaning that the stress-strain relationship is linear in the initial part of the loading [26]. A typical stress-strain plot can be seen in Figure 5. Figure 5 also shows the regions where different types of deformation occur. During loading, the rock experiences different stages during loading. These stages are related to the different types of deformation. A brief description of these regions can be found in Table 3.

The elastic moduli are closely related to each other, and for an isotropic rock, there are only two independent stiffness parameters. By performing different rock mechanical tests, one can obtain two different moduli and determine the rest by using the relationships. A few relationships are listed in Table 2. The most common approach is to determine Young's modulus and the Poisson's ratio from a triaxial test.

The rock's stiffness is characterized by different elastic moduli. These are:

- Young's modulus (E), describing the capability of the rock to deform. The modulus is defined as:

$$E = \frac{\sigma_z}{\varepsilon_z} \tag{8}$$

- Poisson's ratio (v) describing the ratio between lateral strain and axial strain.

$$v = -\frac{\varepsilon_{lat}}{\varepsilon_{ax}} \tag{9}$$

- The bulk modulus (K), describing the capability of withstanding uniform, or hydrostatic, compression. The inverse is known as the bulk compressibility.

$$K = \frac{\sigma_p}{\varepsilon_{vol}} \tag{10}$$

- Lame's parameters, (λ) and (G). G is also known as the shear modulus, describing the rock's resistance against shear deformation.

Another important modulus that is mostly relevant when studying the relationship between acoustic velocities and the rock mechanical parameters is the plane wave modulus or the P-wave modulus (H). The modulus is defined in a later section. In other contexts, this modulus is known as the uniaxial compaction modulus.

Two terms, describing different conditions, are of particular importance when studying stiffness, strength and the different rock mechanical tests:

(i) *Undrained condition* describes a situation at which the pore fluid is not allowed to escape during loading, which implies an increase in pore pressure during axial or radial loading.

(ii) *Drained condition* describes a situation where the pore fluid is allowed to escape meaning that the pore pressure is constant. This term is also used in a situation with a pore pressure equal to 0. The frame moduli are associated with these conditions.

In a triaxial test, the sample undergoes either axial (σ_z) loading, or unloading while keeping the confinement pressure (σ_{rad}) constant. If the rock's strength is to be determined, the sample is loaded until failure. This is addressed in more detail further down. Equation (8) and (9) are used for determining the moduli. It is important to note that the estimated moduli correspond to the applied confinement. Stiffness is normally reduced as higher confinement pressure is applied [26]. Young's modulus and Poisson's ratio are normally denoted with the notation *fr* to show that the moduli are characterizing a matrix frame property. However, the bulk modulus is often used with different notations, K_{fr}, K_s and K_{fl}. *fr* denotes the bulk modulus for the matrix frame (drained bulk modulus), while *s* and *f* denote the bulk modulus for the solid grains and the fluid. It is intuitive that the frame moduli are dependent on the rock porosity, therefore changing porosity will induce changes to these rock mechanical properties as well.

Table 2: Some stiffness parameter relationships. *E* denotes the Young's modulus, *v* the Poisson's ratio, *G* the shear modulus, *K* the bulk modulus and *H* the P-wave modulus/uniaxial compaction modulus.

$E = 3K(1 - 2v)$	(11)	$H = E \dfrac{1 - v}{(1 + v)(1 - 2v)}$	(12)
$E = 2G(1 + v))$	(13)	$K = \dfrac{2}{3} G \dfrac{1 + v}{1 - 2v}$	(14)
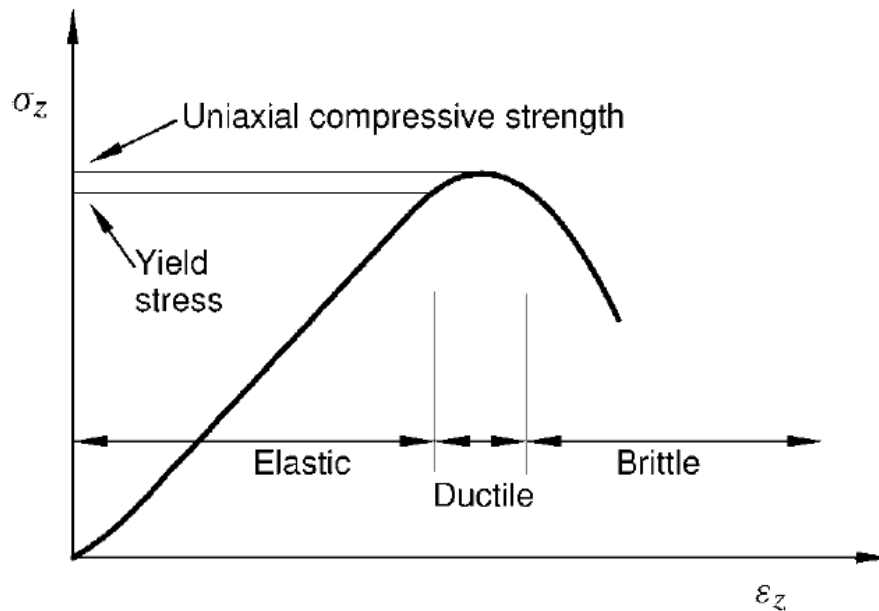
Figure 5: Typical stress – strain curve showing the different types of failure related to the stages that the rock undergoes during loading [26].

Table 3: Description of the different stages that the rock undergoes during loading. The stages occur in chronological sequence. Beginning of stage 6 is equal to the point showing the uniaxial compressive strength.

Stage	Description
1	Closing of pre-existing micro cracks causing an initial non-linearity.
2	Axial and lateral linear behavior. Elastic deformation meaning little permanent damage thus deformation is recoverable.
3	Near linear elastic behavior less recoverable compression micro cracking is induced in a controlled manner.
4	A steep increase in micro-cracking events. The micro-cracking events are merging to occur in the region with highest stress, forming tensile or shear failure depending on the strength.
5	Still intact although macro-cracking and fracturing is induced. Strain is concentrated in weaker elements leading to zones of concentrated strain or shear planes.
6	Failure of the rock followed by a decrease in the stress level. The stress level falls to a level equal to the frictional forces between the sliding planes.

3.3.1.1 Stiffness trend with respect to porosity

Bemer *et al.* [27] derived a set of equations for the purpose of estimating the trends of the bulk and shear modulus with respect to the porosity. A model based on a cemented structure was applied. This model assumes that the solid rock consist of two phases, the grains and the cement. The solid phases and the pore volume make up the dry rock. The following equations were derived:

$$K_{fr} = \frac{(1 - \varphi)K_s}{1 - \varphi + \varphi \frac{K_s}{K_c}}$$

(15)

$$G_{fr} = \frac{(1 - \varphi)G_s}{1 - \varphi + \varphi \frac{G_s}{G_c}}$$

(16)

where φ is the porosity, K_s and G_s are the grain bulk and shear modulus and K_C and G_c the cement bulk and shear modulus. K_{fr} and G_{fr} are the estimated rock bulk and shear modulus. Experimental data has shown that there is no specific trend of the grain and cement ratio with respect to porosity, therefore the ratio is assumed to be constant. Bemer found that for limestone, which is relevant for the current project, the K_c/K_s ratio falls to around 0.07, whereas the G_c/G_s ratio is approximately 0.12. There is a certain error associated with these ratios equal to ± 0.02. The above equations estimate the expected moduli at a specific porosity without any other influencing factors. If the acid has any effect on the alteration of the stiffness in addition to the change in porosity, the treated rock should fall outside the trend line. K_s and G_s can vary for different rocks, thus in order for a proper comparison between the untreated and treated sample, the trend line should be calibrated in order to fit the untreated sample for each respective core sample. By using the grain moduli measured for each sample and tuning the K_c/K_s and G_c/G_s ratio, an optimal fit can be obtained. The trend lines for the Young's modulus can be calculated by combining the equations in Table 2.

3.3.1.2   Stiffness trend: Critical porosity and Nur's Modified Voigt Average
Changes in different parameters are very often correlated to changes in porosity, thus estimating the porosity change is of great interest. Different empirical models have been derived for the relationship between rock mechanical moduli and porosity. A frequently applied model is the critical porosity model and Nur's modified Voigt average. The model is based on the assumption of a critical porosity, φ_c, that separates the mechanical (and the acoustic behavior) for the porous media, into two distinct domains [28]. Lower porosities means that the grains are bearing the load, whereas for higher porosities the fluid bears the load. These are also referred to as solid and suspension state, respectively. The model suggests that in the suspension state, the undrained bulk and shear moduli can be estimated by the Reuss average.

$$K_R^{-1} = (1 - \varphi)K_s^{-1} + \varphi K_{fl}^{-1}; \quad \mu_R = 0$$

(17)

K_s and K_{fl} are the bulk moduli for the solid and the fluid respectively, and φ the porosity. Shear modulus is zero in suspension mode because the shear modulus of the fluid is zero. This state is not very relevant for the current project because the experimental value for the critical porosity of limestone is close to 40% [29].

For the solid mode, Nur [29] showed that the ρV^2 - porosity relationship is linear with a steep decline. V is the acoustic velocity and can be either the P-wave or the S-wave velocity. The linear relationship applies very well for sandstone. In the case of dry rock (drained conditions), the linear dependence can be described as [28]:

$$K_{fr} = K_s(1 - \frac{\varphi}{\varphi_c}) \tag{18}$$

$$G_{fr} = G_s(1 - \frac{\varphi}{\varphi_c}) \tag{19}$$

also known as the modified Voigt average. K_{fr} and G_{fr} are the drained bulk and shear moduli, whereas K_s and G_s are the grain bulk and shear modulus. φ_c is the critical porosity. If clay is present, additional corrections are required. For further reading on different models, I refer to *The Rock Physics Handbook* [28].

3.3.1.3   Elastic moduli bounds in an effective medium
A porous medium normally consists of a mixture of grains and/or pore fluid. In order to predict the elastic moduli in such a medium, three specifications are needed [28]:

(i)   Volume fraction of the various phases
(ii)   Elastic moduli of each phase
(iii)   Geometric details on the orientation of the phases relative to one and another.

The latter is relative hard to determine and one is therefore only able to predict an upper and lower bound for the total elastic moduli. There are two common approaches for determining these bounds. The first is the *Hashin – Shtirkman Bounds,* which is given by [28]:

$$K^{HS\pm} = K_1 + \frac{f_2}{(K_2 - K_1)^{-1} + f_1(K_1 + \frac{4}{3}G_1)^{-1}} \tag{20}$$

for the bulk modulus, and for the shear modulus:

$$G^{HS\pm} = G_1 + \frac{f_2}{(G_2 - G_1)^{-1} + \dfrac{2f_1(K_1 + 2G_1)}{5G_1(K_1 + \frac{4}{3}G_1)}} \tag{21}$$

where K_1 and K_2 represents the bulk modulus of each phase, i.e. matrix and pore fluid, and G_1 and G_2 the shear moduli and f_1 and f_2 the volume fractions. The upper and lower bounds are computed by interchanging the materials termed 1 and 2. For undrained conditions, the fluid is ignored.

The second approach is the *Voigt and Reuss Bounds*. This is considered as the simplest, but not necessarily the best approach [28]. The upper bound, equation (22), and lower bound, equation (23), for each elastic modulus are defined in the same way:

$$M_V = \sum_{i=1}^{N} f_i M_i \tag{22}$$

$$\frac{1}{M_R} = \sum_{i=1}^{N} \frac{f_i}{M_{i}{}_i} \tag{23}$$

where f_i and M_i is the volume fraction and elastic moduli (e.g. Young's modulus or the bulk modulus) of the i -th phase, respectively. The upper bound is referred to as the Voigt upper bound or the isostrain average. The lower bound is commonly known as the Reuss lower bound or the isostress average.

3.3.2   Strength

Compressive strength is defined as the capacity to withstand compressive force. Strength is a matrix property and therefore associated with the effective stress. The strength of a rock is a relative parameter. The given strength for a rock is only meaningful in conjunction with additional information about the stress geometry at which it is measured. There are two primary definitions of strength: (i) uniaxial compressive strength and (ii) triaxial compressive strength. The former is more of a unique term because it defines the strength to withstand axial force with no confining pressure. Triaxial strength however, requires additional information on the lateral confining stresses in order to be meaningful. Higher confinement implies a stiffer and stronger rock. Uniaxial strength is more or less irrelevant for the oil industry because there is always confining pressure on the rock subsurface. There are different failure types, which will be discussed in the following.

3.3.2.1   Failure

Measuring the strength with different confining pressures is used as a tool to determine the parameters describing different failure criteria. Three different failure mechanisms are often mentioned: tensile, shear and compaction failure. Tensile failure occurs when the effective tensile stress across some plane in the sample exceeds a certain limit [26]. This limit is referred to as the tensile strength. The criterion is given by:

$$\sigma_3' = -T_0 \tag{24}$$

where σ_3' is the lowest effective principal stress and T_0 the tensile strength.

Shear failure occurs when shear stress is sufficiently high along one plane. The general definition is:

$$|\tau_{max}| = f(\sigma') \tag{25}$$

τ_{max} is here the maximum allowed shear stress, while f is a function of the effective stress. The Mohr – Coulomb failure criterion is frequently used to define $f(\sigma')$ and in combination with the Mohr circle, to determine if a given stress state is stable or not. Triaxial tests with different confining pressures are performed in order to determine the criterion parameters.
Mohr – Coulomb is addressed in more detail in the next section.

Compaction failure, also known as pore collapse, refers to the condition when the compression is sufficiently high enough to loosen and crush the grains before they are rearranged

and moved to an open pore space, resulting in higher compaction grade of the rock. Figure 6 show the respective regions for the three failure states in the q – p' space.
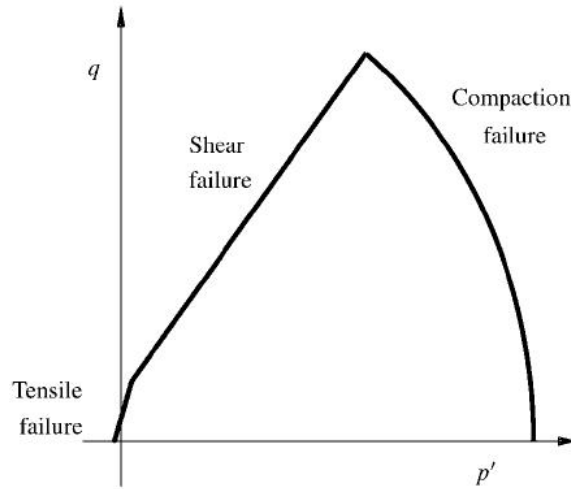
Figure 6: Diagram of q – p' space, showing where each respective failure mode occurs [26].

3.3.2.2 Mohr's circle and the Mohr – Coulomb failure criterion

Mohr's circle is a tool to graphically illustrate the current stress condition along any plane oriented with an angle θ with respect to the highest principal stress (σ_1'). The stresses σ' and τ are then defined as [26]:

$$\sigma' = \frac{1}{2}(\sigma_1' + \sigma_2') + \frac{1}{2}(\sigma_1' - \sigma_2')cos2\theta \tag{26}$$

$$\tau = -\frac{1}{2}(\sigma_1' - \sigma_2')sin2\theta \tag{27}$$

For a particular case with $\sigma_1' > \sigma_2' = \sigma_3'$, we get a circle, as seen in Figure 7, in a τ vs. σ' plot. In a situation where we have $\sigma_1' > \sigma_2' > \sigma_3'$, the Mohr circle becomes three dimensional, Figure 8. The three circles are defined by equation (26) and (27), by substituting the principal stresses accordingly.
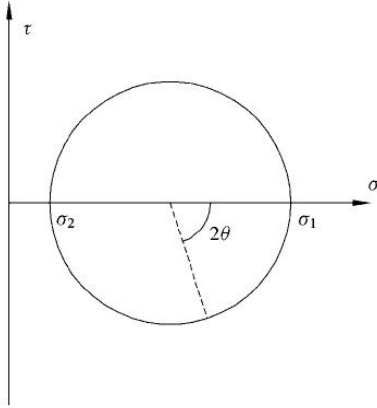
Figure 7: Mohr's circle when $\sigma_1' > \sigma_2' = \sigma_3'$. [26]
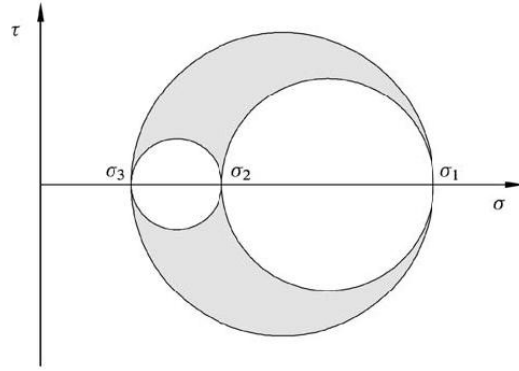
Figure 8: Mohr's circle in three dimensions, $\sigma_1' > \sigma_2' > \sigma_3'$ [26]

Mohr – Coulomb shear failure criterion assumes that $f(\sigma')$ from equation (25) is a linear function defined by:

$$|\tau| = S_0 + \mu\sigma' \tag{28}$$

μ is the coefficient of internal friction while S_0 is the inherent shear strength, or cohesion, of the material. Introducing the friction angle, we obtain:

$$\mu = \tan \emptyset \tag{29}$$

Failure occurs at the point where the Mohr's circle intersects with the failure line as seen in Figure 9. Here, 2β is the angle of the plane at which failure occurs, so by inserting this into equation (28) we obtain:

$$\tau = \frac{1}{2}(\sigma_1' - \sigma_3')\sin 2\beta \tag{30}$$

while the normal stress at failure point is given by:

$$\sigma' = \frac{1}{2}(\sigma_1' + \sigma_3') + \frac{1}{2}(\sigma_1' - \sigma_3')\cos 2\beta \tag{31}$$

Friction angle and failure angle are related through:

$$\beta = \frac{\pi}{4} + \frac{\phi}{2} \tag{32}$$

Uniaxial strength, C_0, is defined as [26]:

$$C_0 = 2S_0 \tan \beta \tag{33}$$

Kristian Engen Eide, Rijswijk, 2012

Combining equation (30) and (32) with the failure criterion, and introducing equation (33), we obtain the most common form of the Mohr-Coulomb criterion:

$$\sigma_1' = C_0 + \sigma_3' \tan^2 \beta \qquad (34)$$
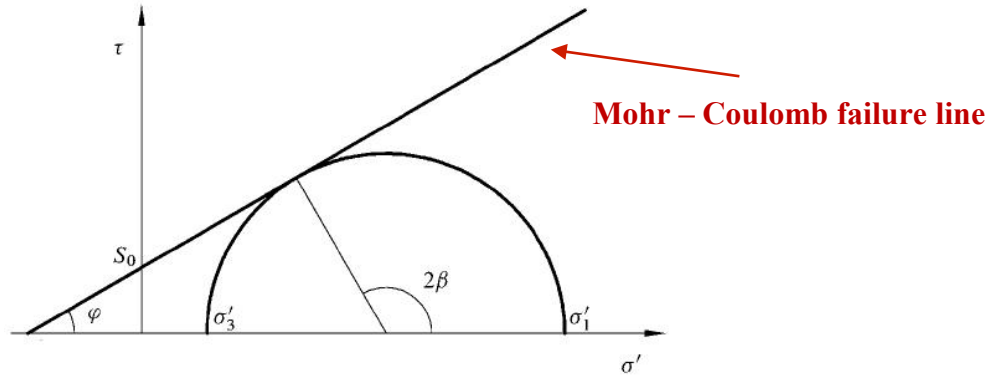
Figure 9: Mohr – Coulomb failure criterion line and the Mohr's circle at failure in a τ vs. σ_N'. [26]

The parameters required for determining the Mohr – Coulomb failure line are normally obtained through triaxial tests. It is preferable to perform a minimum of three triaxial strength tests all with different confining pressures. For practical reasons, results from the triaxial tests are plotted in a deiatoric vs. mean effective stress plot (q – p' space) shown in Figure 10.

$$q = \frac{1}{2}(\sigma_{axial}' - \sigma_{rad}') \qquad (35)$$

$$p' = \frac{1}{2}(\sigma_{axial}' + \sigma_{rad}') \qquad (36)$$

This implies that the friction angle (ϕ), and the cohesion (S_0) are then given by [30]:

$$\sin \phi = \tan \alpha \qquad (37)$$

$$S_0 = \frac{b}{\cos (\phi)} \qquad (38)$$

Here, α and b are defined according to Figure 10.
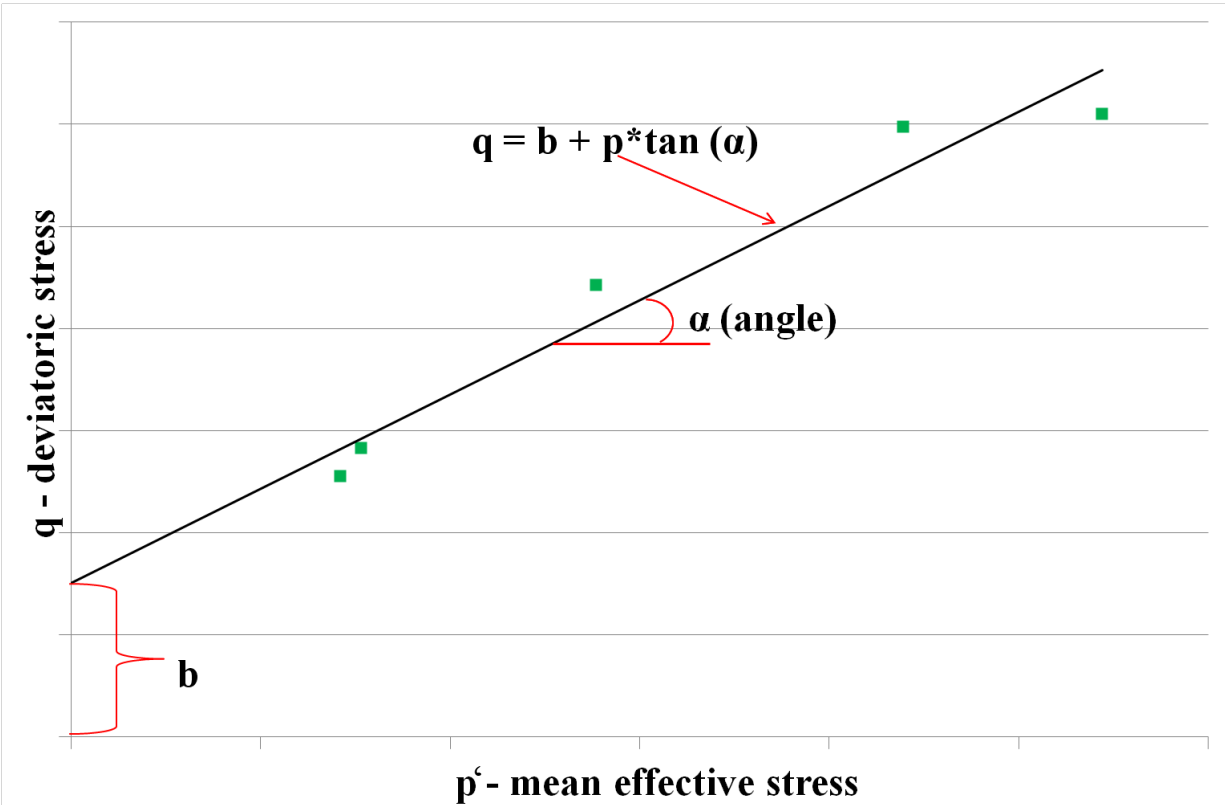
Figure 10: definition of the parameters of the alternative method for determining Mohr – Coulomb failure parameters. Green points indicate the registered failure points in different triaxial tests.

3.4   Rock mechanical properties from acoustic measurements

Seismic monitoring is becoming increasingly widespread, and in CCS projects this is an important tool for estimating changes in porosity, stresses, etc.

Rock properties can be obtained from acoustic velocity measurements. Sound waves can travel a very long distance in a rock. The velocities are related to rock properties, i.e. the stiffness, through the compression degree of the material. Two kinds of waves are normally associated with rock measurements. These are the P-waves (pressure waves, V_p) and the S-waves (shear waves, V_s), in which P-waves are the primary set. The waves can be correlated to the rock properties by:

$$V_p = \sqrt{\frac{K + \frac{4}{3}G}{\rho}} = \sqrt{\frac{\lambda + 2G}{\rho}} \tag{39}$$

and

$$V_s = \sqrt{\frac{G}{\rho}} \tag{40}$$

assuming an isotropic, homogenous and elastic medium. K is here the dynamic bulk modulus of the rock, G the dynamic shear modulus, λ the Lame's coefficient and ρ the density. As fluids do not have a shear modulus, shear waves only depend on the rock properties. It can be shown that the sound velocities can be related to the dynamic Poisson's ratio according to:

$$\frac{V_p^2}{V_s^2} = \frac{2(1-\nu)}{(1-2\nu)} \tag{41}$$

and by combining equations (40) and (41), and rearranging equation (41), we get:

$$K = \rho[V_p^2 - (\frac{4}{3})V_s^2] \tag{42}$$

$$\mu = \rho V_s^2 \tag{43}$$

Finally, the dynamic Young's modulus can be related to the velocities by combining the bulk modulus equation, equation (42), and the correlation between Young's modulus, the shear modulus and the bulk modulus from Table 2. The following equation can then be derived:

$$E = \rho V_s^2 \left[\frac{3V_p^2 - 4V_s^2}{V_p^2 - V_s^2}\right] \tag{44}$$

The P-wave modulus is also of interest in acoustic velocity studies and is defined as:

$$H = \rho V_p^2 = K + (\frac{4}{3})G \tag{45}$$

It is important to distinguish between these moduli obtained from velocity measurements and the moduli obtained from static tests, hence the dynamic term. This will be addressed later.

From the definition of the velocities of the two waveforms, weakening of the rock should result in lower velocities.

Acoustic velocities in rocks depend on several factors, in which stress is one. To a certain extent, this stress dependence could be explained by the induced porosity change that is caused by stress change. In addition, applying stress to a rock could close micro cracks making the rock stiffer. At a certain point, however high stresses induce tensile failure, resulting in a drop of velocities. Acoustic anisotropy is enhanced by anisotropic stress conditions. Other parameters affecting the velocities are temperature, partial saturation and chemical factors. In the current project, partial saturation is not an issue, whereas the temperature effects are corrected for. Chemical factors – whereby the framework of the matrix is altered due to dissolution - are what the current project is all about.

3.4.1 Fluid effect in velocity measurements of the moduli

Moduli obtained from velocity measurements are often referred to as dynamic moduli, whereas moduli obtain from rock mechanical tests, e.g. triaxial tests, are referred to as static moduli. The former moduli differ significantly from static properties. In the case of a saturated rock, the undrained saturated frame modulus is obtained from the velocity measurements. Seismic waves compress the rock when they travel through it, also inducing some compression of the pore fluid. Pore pressure is then increased, enhancing the resistance to compression, making the rock stiffer than what it actually is. This problem is known as the fluid substitution problem [28]. Different models have been derived to take this effect into account. The Gassmann model, equation (46), is one model describing the relationship between measured dynamic frame modulus and the dynamic frame modulus without the fluid effect.

$$
K = K_{fr} + \frac{K_{fl}}{\varphi} \frac{(1 - \frac{K_{fr}}{K_s})^2}{1 + \frac{K_{fl}}{\varphi K_s}(1 - \varphi - \frac{K_{fr}}{K_s})}
\tag{46}
$$

Here, the K is the dynamic undrained saturated frame modulus, K_{fr} the dynamic frame modulus unaffected by the present pore fluid, K_{fl} the fluid modulus, K_s the solid grain modulus or grain compressibility, and φ is the porosity. The Gassmann theory can also be applied to problems in which the change in bulk modulus due to a change in pore fluid is to be obtained.

3.4.2 Static vs. dynamic moduli

For an ideal linear elastic medium, the elastic moduli should in theory be equal regardless of how they are obtained, whether they are static or dynamic. In reality, however, this is not that simple. Moduli obtained from velocity measurements, dynamic tests, do in fact differ significantly from the ones obtained from static tests [31]. Rune Holt and Erling Fjær also showed this difference in a hydrostatic and triaxial test performed on dry Re-Wildmoor sandstone [26]. Figure 11 shows the results from this test, with the bulk modulus on the left, and Young's modulus on the right.
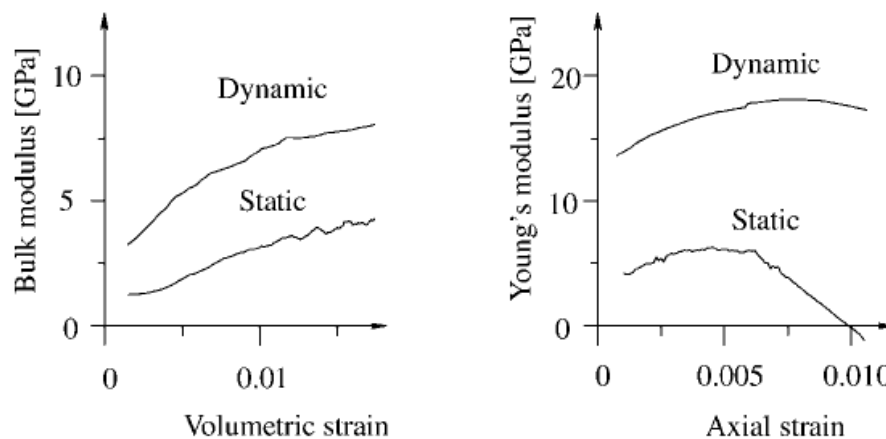
Figure 11: Results from hydrostatic and triaxial tests performed on dry Re-Wildmoor sandstone, by Rune Holt and Erling Fjær [26].

It is not only the pore fluid that is causes the difference [26]. For a homogeneous, elastic material, e.g. steel, the dynamic and static moduli are equal [32]. Fjær has introduced a quantitative model for the relation between static and dynamic moduli described by [26]:

$$K_{stat} = \frac{K_{dyn}}{1 + (P_z + 2P_r)K_{dyn}}$$

(47)

$$E_{stat} = \frac{E_{dyn}}{1 + P_z E_{dyn}}(1 - F)$$

(48)

Here, K_{dyn} and E_{dyn} are the respective dynamic moduli, while K_{stat} and E_{stat} are the static moduli obtained from the slope of the relevant stress – strain curve during initial loading. It is important that initial loading conditions are applied because the rock tends to become stiffer during an unloading – reloading cycle. z and r denote the respective direction related to a triaxial test, whereas P_i and F are parameters containing the difference between the static and dynamic moduli.

Static stiffness moduli are seldom estimated based on dynamic measurements. The dynamic properties are applied in situations where time-lapse seismic is used for monitoring the reservoir. Models have been proposed for the correlation between stiffness change and change in porosity. The evolution of the dynamic properties can then be associated with changes in the porosity to a certain extent.

3.5   Velocity-porosity models

3.5.1   Wyllie's time average: velocity-porosity model
Gary Mavko et al. [28] also present different velocity-porosity models. Wyllie's time average equation is one of them. Wyllie et al. showed that there was a relative simple relationship between acoustic velocities and the porosity under certain criteria:

(i)   Rock with relative uniform mineralogy.
(ii)   Isotropic rock.
(iii)   Fluid saturated.
(iv)   Subject to high stress conditions.
(v)   Should not be used for unconsolidated uncemented rocks.
(vi)   It is limited to primary porosity. Secondary porosity tends to lower the velocities. Under prediction is then expected.
(vii)   Most accurate for intermediate pores.

Wyllie approximated the relation with the following equation:

$$\frac{1}{V_p} = \frac{(1 - \varphi)}{V_{p-grain}} + \frac{\varphi}{V_{p-fl}}$$

(49)

where, φ is the porosity, $V_{p-grain}$ is the P-wave velocity in the grains and V_{p-fl} is the velocity in the fluid. Typical grain velocities of limestone range from 6400 m/s to 7000 m/s. In the case of rocks saturated with water, V_{p-fl} approximates to 1500 m/s.

The interpretation of this equation is that the total P – wave velocity is the sum of the travel time for the wave through the solid part and the fluid. Note that this equation is based on measured data, and cannot be proven theoretically [28]. The above assumption is only valid in seismic ray theory if: (i) the wave length is sufficiently small compared with the typical pore size and grain size, (ii) the pores and grains are arranged as homogeneous layers perpendicular to the ray path. Hence, Wyllie's time average equation should be applied carefully, and not used for acoustic velocity interpretation of significant detail.

Wyllie's equation can be applied in situations where the expected seismic velocity of rock with known mineralogy and pore fluid is to be estimated. It can also be used for estimating the porosity from measured seismic velocities. In the later case, knowledge of the rock mineralogy is also required.

Wyllie's time average equation tends to be conservative in the porosity range of 5% to 25%, implying an underestimate of the porosity with given velocity measurements [33]. Some of the limitations for the equation can be overcome by extending the equation. Empirical corrections exist for shaliness in rocks, secondary porosity, compaction and high porosity rocks (> 47 %). Raymer – Hunt – Gardner Relations [28] is one of these.

3.5.2 Biot's theory – elastic wave propagation

In a saturated porous media, the fluid will have an effect on the wave propagation as mentioned earlier, the same way as it has on the rock mechanical properties. Biot [26] showed that for low frequency waves, the P- and S-wave velocities could be described by the following equations:

$$V_p = \sqrt{\frac{K + \frac{4}{3}G_{fr}}{\varphi \rho_f + (1 - \varphi)\rho_s}} = \sqrt{\frac{H}{\varphi \rho_f + (1 - \varphi)\rho_s}} \tag{50}$$

$$V_s = \sqrt{\frac{G_{fr}}{\varphi \rho_f + (1 - \varphi)\rho_s}} \tag{51}$$

K is here the saturated bulk modulus, described by the Gassmann equation, equation (46). G_{fr} is the drained shear modulus, whereas the ρ_f and ρ_s are the fluid and grain densities, respectively. H is the P-wave modulus defined in equation (45).

This is a simplified approach of the complete Biot derivation, applying only for low frequency sound waves. In this low frequency limit, the solid and fluid are moving in phase [26]. It is also shown that for higher frequencies, the change is not dramatic, being typically less than 3 %. Increasing the frequency enhances the difference between the solid motion and the fluid motion. The flow of fluid relative to the solid is often referred to as "Biot flow". For P-waves,

the change in the "Biot flow" and the deviation from the above definitions increase with increasing frequency in softer rocks.

4.   State of The Art

Homogeneous dissolution of carbonates because of acid interaction is far less studied than the other dissolution regimes associated with carbonate dissolution. As mentioned earlier, wormholing is especially favorable to fully understand because of the applicability with respect to EOR/well stimulation. However, as CCS becomes more relevant, so does the importance of understanding how homogeneous dissolution alters the rock's integrity. We know from the theory that acoustic velocities and stiffness moduli relate to porosity, see Chapter 3. Intuitively, strength is also somewhat dependent on the porosity, thus understanding these relations can be used as an important tool in for example reservoir monitoring, but also changes in the surrounding formations.

The Institut Français du Pétrole (IFP) in France has been very active in terms of developing methods on achieving homogeneous dissolution, and to avoid wormholing, which leads to unrepresentative studies. Two methods have been developed and tested:

(i)   Inject strong acidic HCl on both ends with high rate to obtain a quasi-instantaneous injection. This is done to simulate instantaneous placement of acid into the core sample before allowing it to react followed by flushing with brine for cleaning afterwards.

(ii)   By using retarded acid, one is able to control the reaction to some extent. The applied retarded acid in IFP's case features the ability to remain almost neutral in pH in room temperature, allowing the placement into the sample to be done without any acid-rock interaction. The temperature is then increased, activating the reaction by turning the solution into an acid of pH around 3.

The latter approach has turned out to be a success for IPF and is therefore applied in most of the published work. The former approach was presented in a publication by Egermann *et al.* in 2005 [34]. This paper was reviewed in Eide's '*CO2 induced calcite dissolution in Euville carbonate rock: Formation of wormholes'* [35]. The focus point in Egermann's study was to investigate changes in permeability and porosity, as well as the evolution of the pore size distribution due to carbonate dissolution. They conclude that the high injection rate approach does not result in homogeneous alteration. The reaction speed is to fast compared to the achievable injection rates.

The publication clearly shows that heterogeneous dissolution results in a significant increase in both permeability and porosity. The improvement in permeability for the experiments is as high as 70% for one of the samples, whereas the highest porosity increase is 1.8 PU (porosity units). Figure 12 shows the permeability-porosity evolution. An important assumption made during the study was that the porosity evolutions were directly proportional to the treatment number.

Further on, the mercury porosimetry show a clear increase in intermediate and large sized pores, see [34].
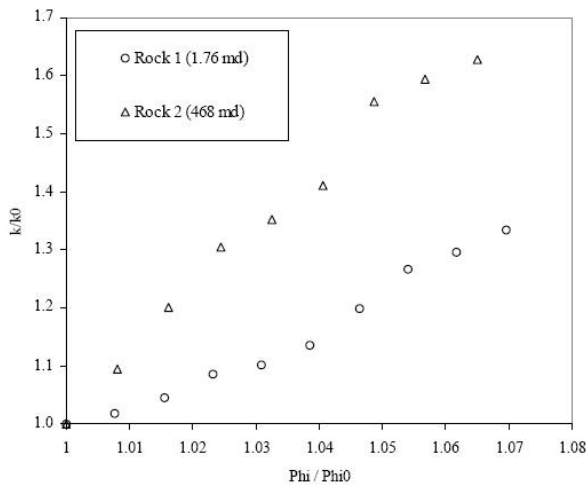
Figure 12: Permeability evolution with respect to the porosity evolution [34].
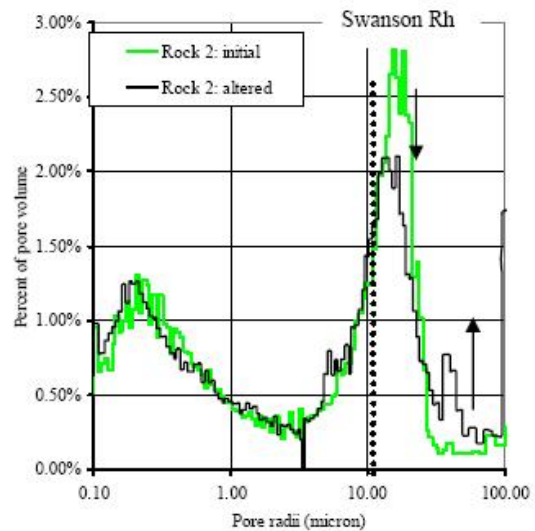
Figure 13: Pore size distribution pre and post alteration. Clear increase in the fraction of intermediate sized pores [34].

Egermann *et al.* also compares the experimental results with a pore network model. They conclude that the experiment is best modeled with the scenario that simulates an increase in both pore body size and pore throat size with the former having twice the growth rate with respect to the latter. The results from the modeling show good consistency with both porosity and pore size distribution evolution. The experimental procedure is concluded to be applicable for assessing alteration studies caused by "true" CO_2 injection into carbonates, *i.e.* when wormholing occurs.

Egermann, Bemer and Zinszner [36] have published a study based on the second approach, followed by two more recent studies. The first one done by Bemer and Lombard [37] in 2010, while the second one by Nguyen *et al.* [38] in 2011, both utilizing the feature of the retarded acid. The main focus in all these three studies was to investigate the relation between homogeneous alteration, porosity change and rock mechanical properties changes. In terms of relevance for the current project, the latter study is performed on Euville Limestone, the same as used in the current project. Some of the results from Nguyen's study will be reviewed and compared against our findings.

All three studies show a significant increase in both porosity and permeability. They agree on that the evolution of the porosity is directly proportional to the number of acid treatments, while the permeability does not change to significantly before having at least three treatments. The studies show a consistent change of about 0.3 to 0.4 PU per treatment, depending slightly on the initial porosity. Although the permeability changes are more unpredictable, it is obvious that more dissolution increases the permeability and supports the modeling theory from Egermann *et al.* 2005 about that there is an increase in pore throats. Figure 14 show the pre and post measurements of the bulk and shear moduli as well as the unconfined strength. This figure show the specific results from Egermann *et al.* 2006, however, the evolution is similar in the other studies. Egermann *et al.* 2006 also address acoustic velocity measurements and how they changes with porosity change. A clear decrease in velocities are seen as the porosity increases, see Figure 15.

Overall, there is consensus in the conclusions about reduced stiffness and strength with respect to increasing porosity due to homogeneous alteration from acid-rock interaction. IFP also indicates that further studies are already initiated.
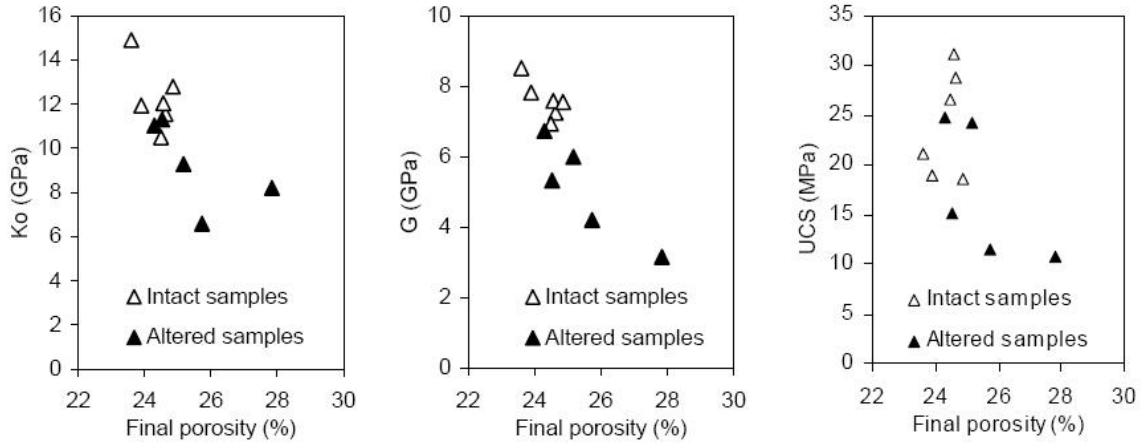
Figure 14: Plot of the different the bulk and shear moduli as well as the unconfined strength (UCS) pre and post alteration. Clear indication of that the rock is weakening with increased porosity due to dissolution [36].

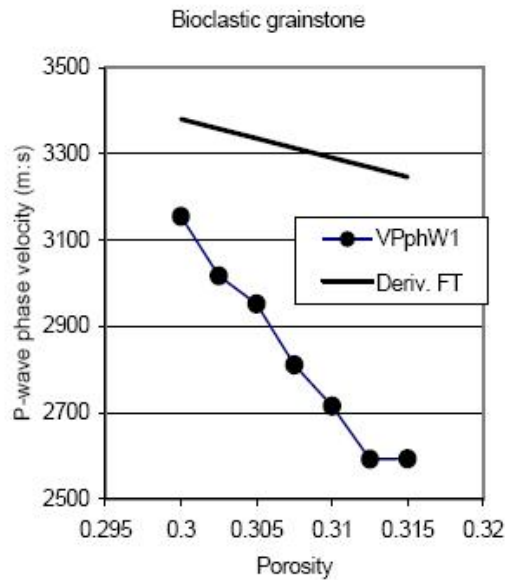**Figure 15: P-wave velocity measurements with increasing porosity. As the porosity increases, the P-wave velocities are decreasing. The solid line represents the empirical "Field Observation Transform" for limestone [36].**

5. Challenges related to experimental determination of rock mechanical properties.

Geomechanical modeling is used for modeling the reservoir and surrounding formation's response to different alterations such as drilling, completion, production and injection. The intension and purpose with applying geomechanical models are to predict problems related to different scenarios, including wellbore stability, faulting, sand production and reservoir compaction. It is also applied for production and injection optimization. These models demand comprehensive and detailed knowledge on rock mechanical properties, magnitude and orientation of principal stresses, as well as pore pressure. Combining geologic, geophysical and petrophysical information, knowledge on this area can be obtained. Petrophysical properties or the mechanical properties are mainly obtained through laboratory work performed on core material, which represents the subsurface formation. There are indeed several uncertainties related to the properties that are estimated through different test such as standard and special core analysis, compaction tests and flooding experiments.

Core analysis can provide important information on e.g. permeability, porosity, wettability and capillary pressure curves. Stiffness and strength properties such as Young's modulus, Poisson's ratio and bulk moduli can be estimated from different compaction tests.

Geomechanical properties are one of the main focus areas in the current project. Several uncertainties follow from estimating these properties in the laboratory. First of all, the size of the samples used in the laboratory is limited by practical reasons. In addition, samples of the subsurface formation are limited to the ability of acquiring core material. One option is to use outcrop material, which is done in the current project. However, the representation is not accurate due to different factors.

Although outcrop material could have the same composition, porosity and permeability as the subsurface formation, rocks respond differently to different stress conditions. Two initially identical rocks that undergo different stress paths could end up with different mechanical properties. A reasonable assumption normally made is that a rock is linear elastic for small deformations, implying that the deformation, both compaction and expansion, is reversible. The higher the stresses are the more inaccurate is the assumption. A rock will always show some hysteresis, where the amount depends on the rock's stiffness. Stiffer rocks usually show much less hysteresis than softer rock. If the rock becomes soft enough, or the stresses high enough, permanent deformation could be induced to the rock. Typical stress – strain paths for loading/unloading in the case of elastic material with hysteresis and material with permanent deformation can be seen in Figure 16 and Figure 17, respectively.

An outcrop has seen a different stress path than the subsurface formation. Firstly, *in situ* stress conditions are different. Outcrops experience atmospheric pressure conditions, whereas the reservoir material is exposed to the overburden stress, pore pressure at a significant depth and so on. The outcrop has also experienced a rising, which the subsurface material has not.
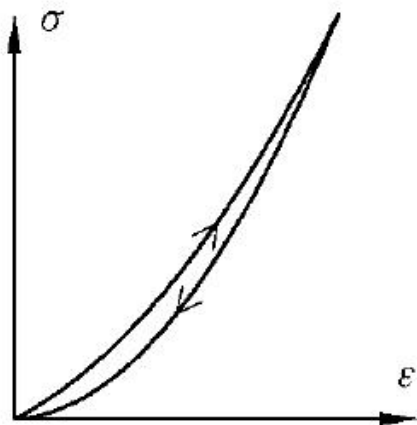
Figure 16: Elastic material with hysteresis.
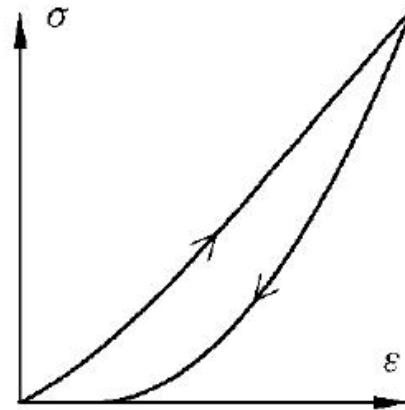
Figure 17: Material with hysteresis and permanent deformation.

The response to different stresses demands that the estimation of rock mechanical properties in the laboratory is performed at *in situ* stress conditions. Comparing the mechanical properties obtained during initial loading and those estimated at *in situ* stress condition, effects of different stress conditions can be seen. During initial loading, micro-cracks could close and the rock becomes compacted, both contributing to a stiffer material. Stiffness and strength properties are obtained by performing different stress cycles including unloading/reloading. The hysteresis effect can clearly be seen from the unloading/reloading, Figure 17. The stiffness properties can be estimated from both the unlading and reloading but the result differs significantly. So what is the most accurate estimation? One option is to apply the average from the unloading and reloading.

Another factor that questions the validity of an outcrop as a representation of the subsurface formation is the exposure to air. This induces weathering, chemical pollution, changes in pore fluid and saturation. All these aspects could cause alteration of the rock's properties making it a non-representative material.

Sample size is causing a huge uncertainty as well. A core sample is only a small fraction of the whole formation, and represents only a local area. Another common assumption is that the rock is isotropic, meaning that the properties are equal anywhere in the formation. This is one of the simplest assumptions done in the estimation of rock mechanical properties and geomechanical modeling. In reality, rock is very heterogeneous. Thus the properties estimated from a core sample are only representative for that very local part of the rock. To eliminate this, one has to do tests on a vast number of samples taken from areas spread across the formation. All the results must then be incorporated into the geomechanical model. Weaker parts of the rock, *i.e.* less consolidated parts, fractured rock and soft spots in the rock, are usually not tested in the laboratory. This gives an overestimate of the actual strength and stiffness of the formation, which in terms of modeling will result in the wrong predictions.

Incorporating the complete anisotropy of the formation into a geomechanical model is impossible. The applied solution to this problem is to simulate different scenarios. To overcome overestimated stiffness and strength properties, extreme stress conditions could be simulated. Other extreme conditions can also aid in the prediction of possible problems that could be encountered in reservoir management.

6.   The experiments

6.1   Core material properties

Dry Euville carbonate from the Euville Outcrops in the northern part of France has been used in the current project. This outcrop is representative for Limestone tests having a rather simple composition, consisting mainly of calcite ($CaCO_3$) and some clay (~2%). A total of 8 different core samples have been used in the experiment, in which all are from the same outcrop block except one (EU_06).

Routine and more advanced core analysis were initially applied in order to obtain petrophysical and hydrodynamic properties such as porosity, permeability, density, lithology etc. Bulk and pore volume estimations as well as Klinkenberg corrected permeability have been obtained through core analysis, while threshold pressure and pore size distribution were obtained through high-pressure mercury injection. Beige color and medium sized angular grains were dominating the visual characterization of the samples.

Initial weight, porosity and permeability are presented in Table 4, whereas additional pre-test properties and physical measurements such as length, diameter and other values are summarized in the appendix. Pre experimental CT scanning was performed on relevant samples. A reference sample was subjected to mercury intrusion for porosimetry with the resulting pore size distribution plot showing in Figure 18. Section 6.2 has a short description on some of the procedures for measuring initial porosity, permeability and how the mercury measurement is done.

Table 4: Initial properties of the different core samples used in the current project.

Sample ID	Weight	Porosity	Permeability
EU_06	191.76	16.5%	190
EU2_01	189.52	16.9%	266
EU2_02	190.15	16.6%	322
EU2_03	190.30	16.6%	288
EU2_05	189.60	16.4%	267
EU2_07	191.19	16.2%	259
EU2_08	190.48	16.5%	310
EU2_09	191.88	15.7%	210
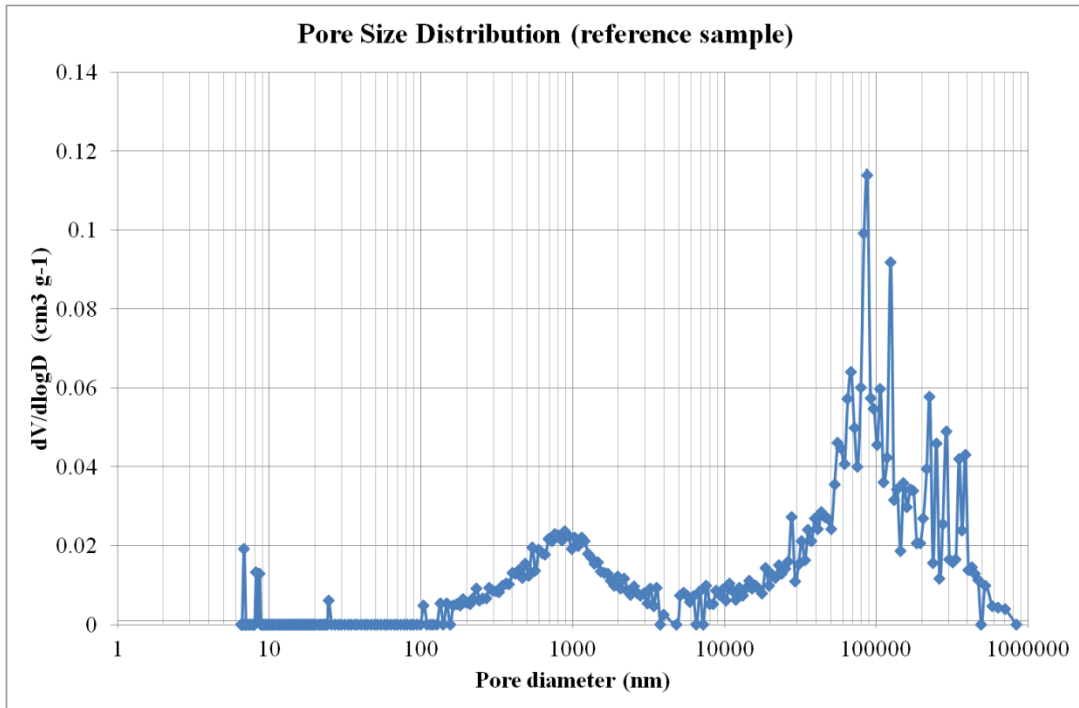
Figure 18: Pore size distribution plot for the untreated reference sample. There is a predominance of macro-pores.

Looking at the pore size distribution plot, we see that there is a predominance of macro-pores.

The strength envelope for unaltered Euville will be determined by performing three failure tests at different confining pressures. This is addressed in more detail in Chapter 8.

6.2 Pre measurements: CT scanning, porosity, permeability and mercury porosimetry.

6.2.1 CT scanning

Application: Imaging method for internal macro structure studies of the core sample. The created images can be processed in different ways and used for grain – pore relation studies.

Method: All samples are dried before subjected to X-Ray Computed Tomography (CT) scanning. In the current project, a Siemens Volume Zoom IV spiral scanner located at the Shell's Rock and Fluid Physics laboratory in Rijswijk. A certain tube potential (kV) and current (mAs), are applied (120 kV and 90 mAs in the current project). The gray values produced in a CT scan are expressed in Hounsfield units (HU) and the X-Ray attenuation is calibrated such that air corresponds to 1000 HU. Core materials have much higher HU values than this. The resolution for the medical CT scanner is 10.24 pixels per millimeter.

6.2.2 Porosity – permeability – grain density

The porosity is determined in three steps:
-   Bulk volume (V_b) is measured from the length and diameter of the sample.
-   The grain volume (V_g) is determined by submerging the sample in chloroform and allowing full saturation. The core is then weighted while submerged. From weight and chloroform density, grain volume is determined.
-   Porosity is then calculated by:

$$\varphi = \frac{V_b - V_g}{V_b} \tag{52}$$

The permeability is measured with a $KA - 210$ gas permeameter supplied by Coretest System Inc. USA. The core is placed in a sleeve and a pressure (400 psi) is applied. Air is flushed through the core while measuring the flow rate and pressure gradient over the core sample. The permeability to air is then calculated by:

$$K_a = \frac{2\mu Q_b P_b L}{A(P_1^2 - P_1^2)} \tag{53}$$

where K_a is the permeability respective to air, μ viscosity of the air, Q_b is the flow rate, P_b the atmospheric pressure, P_1 and P_2 the pressures at the inlet and outlet, respectively, L the length and A the cross section area of the core sample. To obtain the permeability relative to liquids, the gas permeability (K_a) is Klinkenberg corrected.

Grain density is calculated by dividing the dry weight of the sample by the grain volume determined from the porosity measurement.

6.2.3 Mercury injection – porosimetry

Application: Analytical method for determining porosity, pore volume, capillary pressure and pore size distribution and density. Except for important information about the pores, the technique gives the capillary pressure curve, which is important for understanding: saturation distribution in the reservoir, imbibition processes and multiphase fluid flow through the rock.

Method: The system consists of a mercury container, a vacuum pump, a pressure pump and a sample container. First step is to vacuum the sample, removing all air. The sample container is then filled with mercury before pressure is applied, forcing the intrusion of mercury into the sample. The pressure is lowered allowing some mercury to extrude. Mercury is always a non-wetting phase with high surface tension. Only the applied pressure and the cumulative volume of injected mercury are measured. The rest is calculated. The system is schematically illustrated in Figure 19 and a typical result plot from an experiment can be seen in Figure 20. Blue line represents intrusion data points, while red curve represents the extrusion data due to pressure decrease.
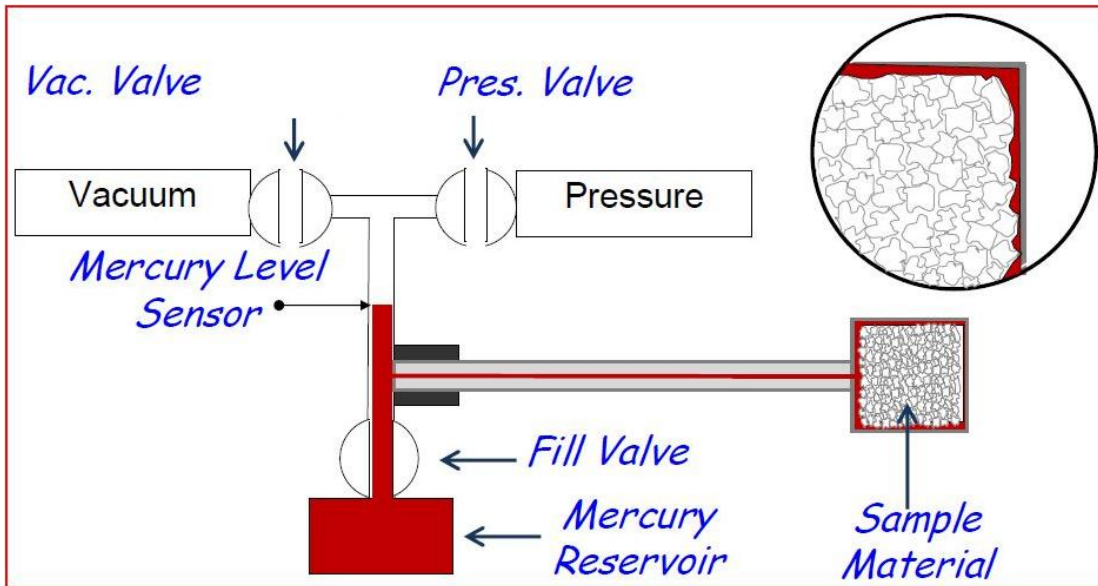
Figure 19: Schematic of mercury porosimetry system, showing the mercury-filling step. Picture made by Ton Blok at Shell's research facility in Rijswijk, the Netherlands.
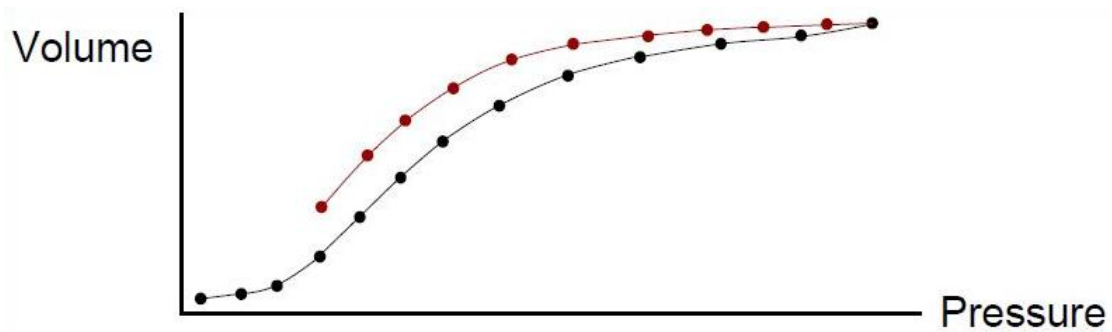
Figure 20: Typical data plot from a mercury injection experiment. Blue line represents pressure increase and intrusion data, whereas red line represents pressure decrease and extrusion data. Picture made by Ton Blok at Shell's research facility in Rijswijk, the Netherlands.

6.3 Experimental program

As mentioned above, a total of 8 core samples were used during the experiment. 3 remained unaltered, whereas 5 were subjected to retarded acid treatments. The experiments were performed according to the following program, Table 5, which also includes an overview of the primary objective for each particular experiment.

Table 5: Experimental program, showing specific objective for each particular experiment and additional details on confining pressure conditions at failure.

Sample	# of acid treatments	Objective	Confinement pressure at failure *[MPa]*
EU_06	3	Core analysis, CT scanning and mercury injection	-
EU2_01	6		-
EU2_02	6	Determine failure envelope treated Euville.	5
EU2_05	6		0
EU2_07	6		10
EU2_03	0	Determine failure envelope untreated Euville.	10
EU2_08	0		1
EU2_09	0		0 (UCS – test)

6.4 Experimental setup

A flow scheme of the experimental setup is shown in Figure 21. With only a few modifications, the setup is applicable for experiments involving CO_2 flooding.

An ISCO pump was connected to the compaction cell, which was used for saturating the sample with retarded acid before treatment. The Quizix pump (pump 1) was used for flushing the sample with fresh brine after the acid reaction for cleaning and permeability measurement purposes. Flow control was applied for this pump. Both the Quizix and ISCO pumps feature the ability to deliver fluid at constant rates and high pressures making them suitable for the current experiment. The Quizix pump is better suited for smaller volumes, while the ISCO has a slightly smaller flow rate, but a higher capacity. The current experiment flooded only a maximum of 4 PV, thus the limitations were not an issue.

The core sample was built into a triaxial compression cell. Figure 22 shows a schematic drawing of the cell. The sample was placed between titanium end-caps and enclosed in impermeable 2.5 mm thick HNBR sleeve. Between the titanium end-caps, featuring bores to enable fluid access, porous plates were used to enable fluid distribution over the cross section of the sample during injection. The pressure vessel in which the assembly was placed in had a capacity of 100 MPa axial and radial pressures. Axial loading was achieved by pressurizing fluid in a chamber at the bottom of the hydraulic piston in the pump. Axial pressure was measured using a 100 MPa pressure gauge. Pressurized oil, surrounding the elastomer sleeve, was used to apply radial stress to the setup. Pore fluid pressure was applied through the top end-cap and monitored both at the top and bottom with a 100 MPa gauge. This allowed for verification of full pore pressure communication during the experiment.
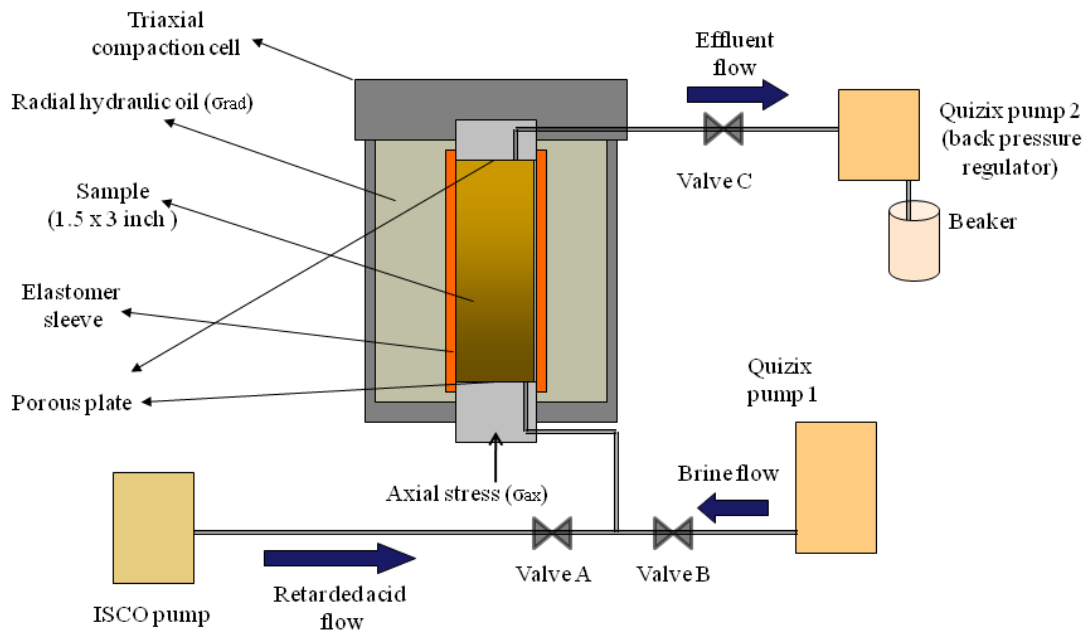
Figure 21: Schematic of the experimental setup.
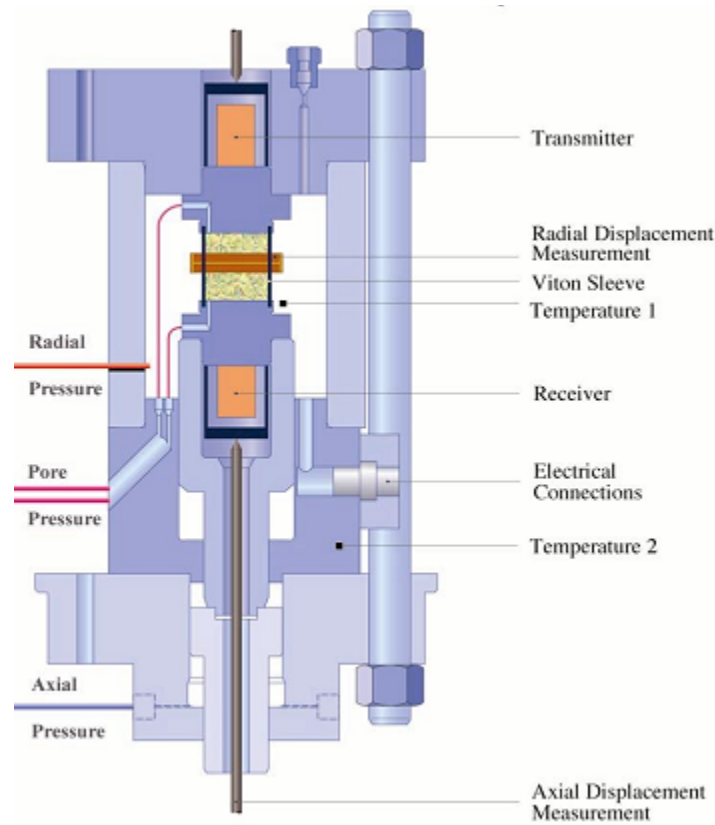
Figure 22: Schematic drawing of the compression cell.

The compression cell also featured two linear variable displacement transducers (LDT) for continuously measuring axial strain. Note that corrections were made for the axial deformation of the titanium end-caps due to axial load and temperature changes. Radial strain measurements were made by a cantilever bridge (Radial displacement transducer, RDT) equipped with foil strain gauges that was clamped onto two pins penetrating the sleeve and being in direct contact with the sample. Piezoelectric transmitter and receiver were integrated in the end-caps for ultrasonic velocity measurements in axial direction.

For back-pressure maintenance, a second Quizix pump (pump 2) was connected to the outlet of the cell. Effluent was collected in a 1-liter beaker placed at the outlet of the second Quizix pump for further analysis. Data acquisition and experimental sequence control was done by custom-built software.

6.5 Experimental procedure

Different objectives required different procedures. Initial measurements and scans, as mentioned earlier, were the same for all samples. A total set of 77 CT scans was taken on each sample with a resolution of 10.24 pixels per mm.

In terms of procedure for the acid treatment experiments, the following protocol was applied:

1. Build in the sample into the triaxial cell.
2. Vacuum and saturate the core with brine to a pore pressure of 5 bars.
3. Bring sample to *in situ* stress conditions ($\sigma_{ax} = 200\ bars$, $\sigma_{rad} = 150\ bars$, $p_f = 100\ bars$) following a specific sequence of:
   a. 20 bars isostatic loading. Measure loading bulk modulus (K_{fr})
   b. 95 bars constant net stress increase. Measure loading grain modulus (K_s)
   c. 5 bars radial stress increase.
   d. 45 bars axial loading. Determining loading Young's modulus (E_{fr}) and Poisson's ratio (v_{fr}).
   e. 8 hours consolidation period at *in situ* stress conditions, with acoustic velocity recordings every 15 min.
4. Measure Young's modulus and Poisson's ratio in a uniaxial unloading/reloading cycle with axial stress changed by 42 bars [1).
5. Bulk modulus measured in an isostatic unloading/loading cycle, with axial and radial stress change by 42 bars [1).
6. Measure permeability at *in situ* conditions. Core is flooded with different constant flow rates, 0.05, 0.1, 0.2, 0.3 and 0.4 ml/min. Pressure difference is measured and permeability is calculated from Darcy's equation.
7. Saturate core sample with retarded acid solution. Flooded with approximately 3 PV.
8. Heat to 80 ºC.
9. Allow 15 - 24 hours reaction time. Longer time was set for weekends.
10. Cool the sample to ambient temperature (25 ºC).
11. Flush sample and system with brine for cleaning and wash out purposes, approximately 3 PV.
12. Measure Young's modulus, Poisson's ratio and Bulk modulus in unloading – loading cycle, see step 4 and 5. Measure permeability, see step 6.
13. Repeat step 7 – 13 according to experimental program.

Acoustic velocities were continuously measured by inducing a pulse in the transmitter crystal that travels along the length of the core before being registered by the receiver crystal. Due to malfunction, velocities were not measured during the 3 RAT experiment (EU_06). Acoustic velocities were also not measured for untreated failure experiments (EU2_03, EU2_08 and EU2_09).

The injected acid solution consisted of 10% retarded acid, and 90% water (tap water). Potassium format (KCOOH) was added to buffer the solution at room temperature, having an initial pH of approximately 6.4 before injection. Only effluent from step 11 was accumulated and analyzed, with the exception of EU_06. The reason for not sampling during EU_06 was that this experiment was only meant as a protocol test. Due to good results and time limitation, it was chosen to include this experiment as a part of the project.

Experiments with the prime objective to be post CT scanned and mercury injected, had the sample built out. To avoid damage during build out, samples subjected to strength measurements were kept in the cell, applied confining pressure according to Table 5 and brought to failure. The untreated failure envelope was determination from performing different failure tests on untreated samples with different confining pressure according to Table 5.

A set of 77 CT scans was obtained for the built out samples, having the same resolution as the pre scans.

---

1) The unloading is divided into two steps. First a 12 bar unloading step followed by 5 min consolidation to overcome friction effects, then a 30 bar decrease. Same procedure is applied for the re-loading.

7.   Experimental results

In the following section, the most important results are summarized. Additional results can be found in the appendix. Arjan van der Linden, researcher at Shell Rijswijk Research Center, has assisted with supervising and also completing some of the experiments. Experiment EU_06, EU2_03 and EU2_08 were fully carried out by Arjan, whereas EU2_05 was initiated by Kristian Eide and completed by Arjan. Shell researcher Fons Marcelis performed special core analysis and together with Ton Blok had the CT scanning and MICP done. Effluent analyze was carried out by Carl van Rijn, associate research technician at the Shell International Research Center Rijswijk and Merit van der Lee, Associate Researcher. Contact information can be found in the appendix.

7.1   Stress and strain path

Because all of the experiments involving treatment followed the same protocols, the stress and strain paths are more or less equal. The plot below, Figure 23, shows a typical stress, path, whereas Figure 24 shows strain and temperature paths. The spikes in Figure 23 are present due to frictional corrections causing an increase in pressure. The longer periods with elevated temperatures, in Figure 24, are caused by longer temperature interval over a weekend. Having a period with longer elevated temperature is not believed to have any additional affect on the results because of the fast reaction speeds.
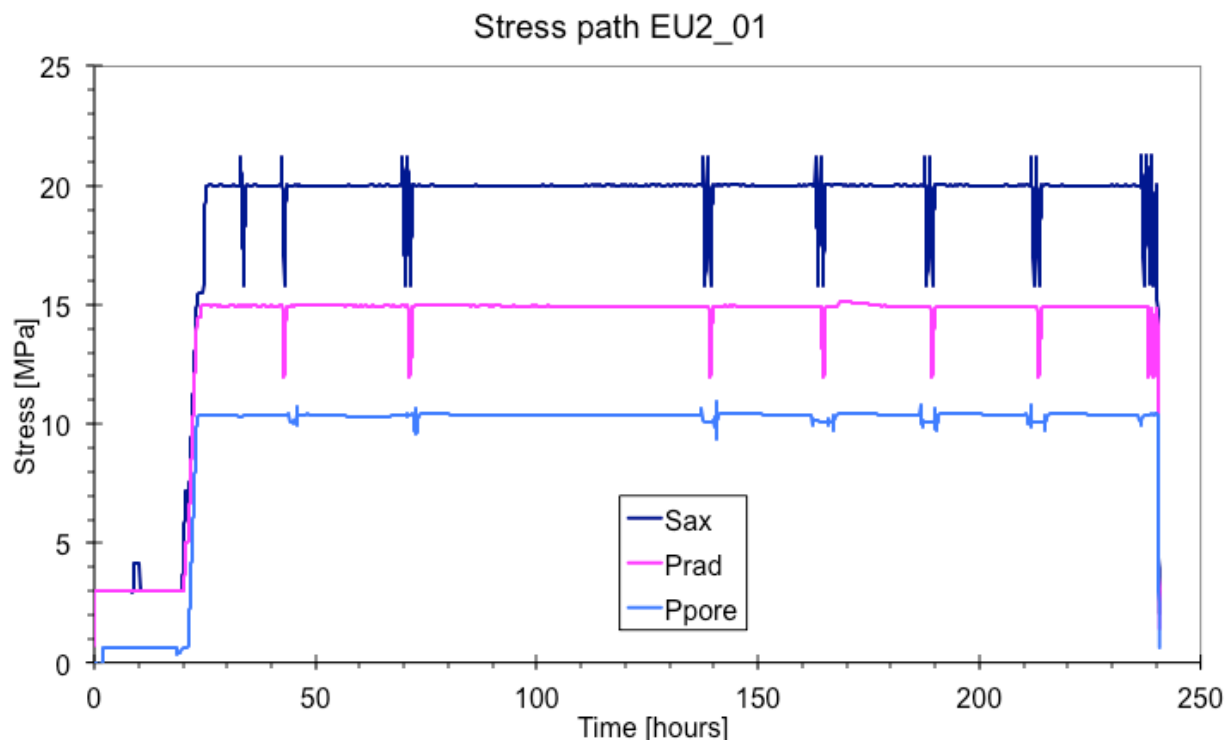
Figure 23: Stress path for the EU2_01 experiment. This stress path is similar for all the treatment experiments. The isostatic unloading/reloading cycles are performed instantaneously after the uniaxial cycle hence, appearing almost as one cycle on the S$_{ax}$ curve.
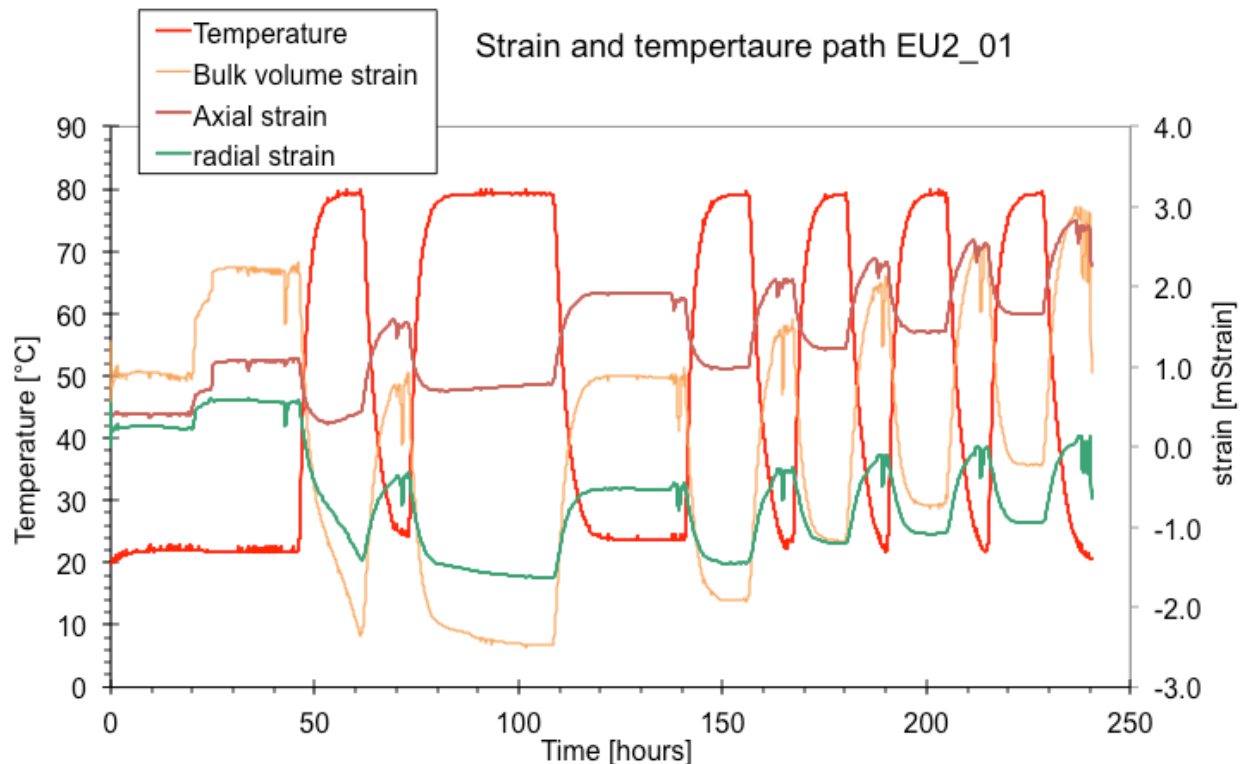
Figure 24: Strain and temperature path for EU2_01. The paths are similar for the other treatment experiments. Longer temperature periods are caused by weekends where elevated temperature was kept for a longer time. This does not affect the experimental result.

7.2   Measured rock mechanical properties

Two samples were built out and subjected to core analysis. Core analysis was also attempted on the failed samples with various results. Table 6 presents the final results obtained from the analysis.

Table 6: Weight, porosity and permeability measurements. Only EU_06 and EU2_01 were built out and subjected to core analysis. Possible measurements were done for the failed samples.

Sample ID	Weight	Porosity	Permeability	Permeability*
EU_06	189.45	16.9 %	2750	280.9
EU2_01	180.65	19.9 %	2798	261.7

Measured permeability at in situ stress conditions based on Darcy flow.

Young's modulus, Poisson's ratio, and Bulk modulus have been measured during unloading and reloading cycles. They can be estimated from both unloading and reloading part, though a difference is expected. The causes to these differences are discussed in more detail in Chapter 5. Table 7 to Table 11 shows the estimated rock mechanical properties from unloading and reloading as well as the average value, pre and post to the experiments. The table also includes the calculated value of the bulk modulus based on Young's modulus and Poisson's ratio. Table 12 contains the estimated grain modulus (K_s) for each of the experiments. A more detailed overview of the estimated rock mechanical properties after each treatment can be found in the appendix.

Table 7: Young's modulus estimated from the unloading, reloading and average prior to and post treatments.

Sample ID	Young's modulus (E_{fr}) [GPa]					
	Initial			Final		
	Unload	Reload	Average	Unload	Reload	Average
EU_06	18.5	20.8	19.6	11.2	16.8	14.0
EU2_01	25.2	26.0	25.6	11.9	14.6	13.2
EU2_02	24.1	25.7	24.9	13.7	14.2	13.9
EU2_05	17.9	19.0	18.4	7.8	9.5	8.7
EU2_07	18.6	18.3	18.4	13.0	15.2	14.1

Table 8: Poisson's ratio estimated from the unloading, reloading and average prior to and post treatments.

Sample ID	Poisson's ratio (v_{fr})					
	Initial			Final		
	Unload	Reload	Average	Unload	Reload	Average
EU_06	0.20	0.10	0.15	0.29	0.16	0.23
EU2_01	0.19	0.20	0.20	0.32	0.25	0.28
EU2_02	0.20	0.22	0.21	0.32	0.27	0.29
EU2_05	0.18	0.19	0.18	0.37	0.30	0.33
EU2_07	0.11	0.11	0.11	0.28	0.25	0.26

Table 9: Calculated bulk modulus based on Young's modulus and the Poisson's ratio for the unloading, reloading and the average, prior to and post treatments.

Sample ID	Bulk modulus (K_{fr}) (calculated) [GPa]					
	Initial			Final		
	Unload	Reload	Average	Unload	Reload	Average
EU_06	10.2	8.5	9.4	8.9	8.3	8.6
EU2_01	13.6	14.7	14.1	10.8	9.7	10.2
EU2_02	13.6	15.4	14.5	12.4	10.4	11.4
EU2_05	9.2	10.2	9.7	9.8	7.8	8.8
EU2_07	7.9	7.9	7.9	9.6	10.0	9.8

Table 10: Bulk modulus estimated from the unloading, reloading and average (from the isostatic cycles) prior to and post treatments.

Sample ID	Bulk modulus (K_{fr}) (measured) [GPa]					
	Initial			Final		
	Unload	Reload	Average	Unload	Reload	Average
EU_06	-	-	-	-	-	-
EU2_01	3.6	5.3	4.4	2.8	4.0	3.4
EU2_02	5.0	4.3	4.6	2.9	4.2	3.6
EU2_05*	3.4	3.9	3.7	3.5	3.3	3.4
EU2_07	3.8	4.3	4.1	2.6	3.5	3.1

The final values are after the 5th treatment. 6th treatment measurements were not possible due to technical problems during the bulk modulus cycle.

Table 11: Shear modulus calculated from the Young's modulus and Poisson's ratio during loading, reloading and average, prior to and post treatments.

Sample ID	Shear modulus (G_{fr}) [GPa]					
	Initial			Final		
	Unload	Reload	Average	Unload	Reload	Average
EU_06	7.7	9.5	8.6	4.3	7.2	5.7
EU2_01	10.6	10.8	10.7	4.5	5.8	5.2
EU2_02	10.0	10.5	10.3	5.2	5.6	5.4
EU2_05	7.6	8.0	7.8	2.8	3.7	3.2
EU2_07	8.4	8.2	8.3	5.1	6.1	5.6

Table 12: Estimated grain modulus (K_s) for each sample.

Sample ID	Grain modulus (K_s) [GPa]
EU_06	48.4
EU2_01	57.5
EU2_02	74.3
EU2_05	67.7
EU2_07	48.8
Average	59.3 ± 11.5

7.3   Strength results

A total of three untreated samples were failed at different confining pressures. 6 RAT samples were also subjected to failure with various confining pressures. Table 13 contains the failure data.

Table 13: Failure data for the failed samples.

Sample ID	Treatment	Failure point (effective stresses) [MPa]			p'	q
		Axial stress	Radial stress	Mean stress		
EU2_02	6 RAT	25.61	4.65	11.64	15.13	10.48
EU2_03	Untreated	54.12	9.99	24.70	32.06	22.07
EU2_05	6 RAT	19.16	0.00	6.39	9.58	9.58
EU2_07	6 RAT	30.99	9.45	16.63	20.22	10.77
EU2_08	Untreated	28.96	0.98	10.31	14.97	13.99
EU2_09	Untreated	26.07	0.00	8.69	13.04	13.04

*p' denotes the effective mean stress, whereas q denotes the deiatoric stress. Both calculated based on the equation **(35)** and **(36)** in Chapter 3.*

7.4 Effluent analysis

In addition to the above measurements, effluent samples were taken and analyzed for calcium concentration. Note that the experiment, in which three acid treatments were performed, did not have any effluent samples taken. This experiment was in the beginning only meant to be a test. However, based on the results, it was decided that this experiment was of great relevance and therefore included. The results from the effluent analyzes are summarized in Table 14.

Table 14: Calcium concentration in the effluent after each treatment. The reference sample (pure tap water) and a sample taken during acid flooding in the EU2_01 experiment are included.

Sample ID	Reference (water)	1st	2nd	3rd	4th	5th	6th	Acid flooding
EU2_01	51.1	1898.0	3660.4	6262.4	5830.5	5214.2	4668.0	2212.9
EU2_02	-	4101.0	5157.5	5567.5	5791.0	5833.0	5503.9	-
EU2_05	-	4850.9	4725.2	4519.8	4550.5	5742.5	*	-
EU2_07	-	3069.5	5993.8	6173.9	6381.2	5892.9	5730.6	-

Due to spill, the 6th effluent sample of EU2_05 was lost.

7.5 Velocity results

Acoustic velocities were measured for most of the experiments. EU_06 did not have velocity measurements because of defect equipment at the time. Instability in the equipment has also resulted in some inconsistency in the measurements. Table 15 to Table 16 contains the measured velocities prior to and after each treatment

Table 15: Measured P-wave velocities after each treatment.

Sample ID	Prior	1st	2nd	3rd	4th	5th	6th
EU2_01	4555.2	4349.3	4068.7	3935.1	3882.5	3837.9	3839.5
EU2_02	4437.6	4286.3	4125.9	4004.7	3921.6	3872.1	3646.1
EU2_05	4402.4	4261.8	4150.5	4066.9	3962.5	3880.0	NA
EU2_07	4368.8	4290.4	4157.2	4134.9	3964.8	3899.9	3807.7

Table 16: Measured S-wave velocities after each treatment.

Sample ID	Prior	1st	2nd	3rd	4th	5th	6th
EU2_01	2248.3	2023.3	1811.4	1748.6	1739.7	1710.6	1662.6
EU2_02	2024.5	1907.6	1852.1	1990.6	1728.3	2411.0	1709.8
EU2_05	2303.3	2273.2	2235.3	2183.1	1848.8	1739.4	NA
EU2_07	2217.6	2194.9	2133.6	2122.8	1901.2	1873.7	1843.0

8.   Discussion

In the following chapter, results are discussed and compared to some of the work done by other parties. First of all, we are interested in seeing whether the results we have obtained are in line with what has been done earlier, or if there are new findings. Secondly, we want to assess the effects that the acid exposure might have to the formation and the consequences.

The term RAT is frequently used in this chapter, denoting Retarded Acid Treatment. Estimated moduli and other values are given for *in situ* stress conditions as defined in the experimental protocol, Section 6.5.

There are a lot of errors related to such experiments. Measuring the rock mechanical properties are sensitive to small changes within the rock. Chapter 5 addresses some of the uncertainties related to the measuring rock mechanical properties in the lab. There is an overall uncertainty of approximately 0.5% for the compaction cell, whereas the uncertainty due to heterogeneities in the sample is higher. Equipment errors are reduced by frequently calibrating the sensors. For example, axial and radial transducers are calibrated with respect to aluminum, which has known parameters for certain stress paths.

The outcrop material used has an expected uncertainty from heterogeneities of approximately 10%. In the following discussion, 10% is taken into account for the results related to the creep cell. For acoustic velocity measurements, an error of 5% is assumed. Special core analysis errors are set to being 10% for permeability measurements and 5% for porosity measurements.

8.1   Dissolution pattern

In general, Euville carbonate is rather homogeneous in terms of pore structure, pore and grain size as well as composition. This implies great conditions for homogeneous alteration. In reality, most reservoirs are more heterogeneous, thus the use of a pure homogeneous carbonate will give us the worst case with respect to dissolution. All acid will be spent during each treatment and therefore result in most dissolution. Having a rock that is more heterogeneous in terms of composition will have less dissolution if it consists of grains unsolvable by acid.

In the current project, we have applied two different degrees of altering of the rock material. One experiment was performed with three retarded acid treatments, while in the other experiments the samples were treated six times. Six treatments were chosen in order to achieve an extreme effect.

From visual examination of the rock, subjecting the sample to three retarded acid treatments, show indications of wormholing at the inlet while the outlet looks more or less unaltered. The sample subjected to six treatments has even more distinct indications of wormholing at the inlet. However, visual examination is not enough to verify the general dissolution pattern, thus examining the internal alteration is necessary with e.g. CT scanning. The principle behind CT scanning can be utilized in the evaluation of the dissolution in the samples. Absorption of X-ray is element specific (heavier elements absorb more than lighter elements) and depends on the density of the particular element. Air shows weak X-ray absorption and rock grains exhibit high absorption. The generated images use grey scale to visualize the attenuation. Black areas imply air and hence represent the pore space in a dry sample.

Advanced image-processing software featured the ability to create 3D models for the CT scans. Using different coloring methods enables for 3D visualization of the dissolution pattern as seen in Figure 25 and Figure 26. The figures show a 3D visualization of the EU_06 (3 RAT)

---

sample and the EU2_01 (6 RAT) sample, respectively. The red coloring area is representing the change in pore space.
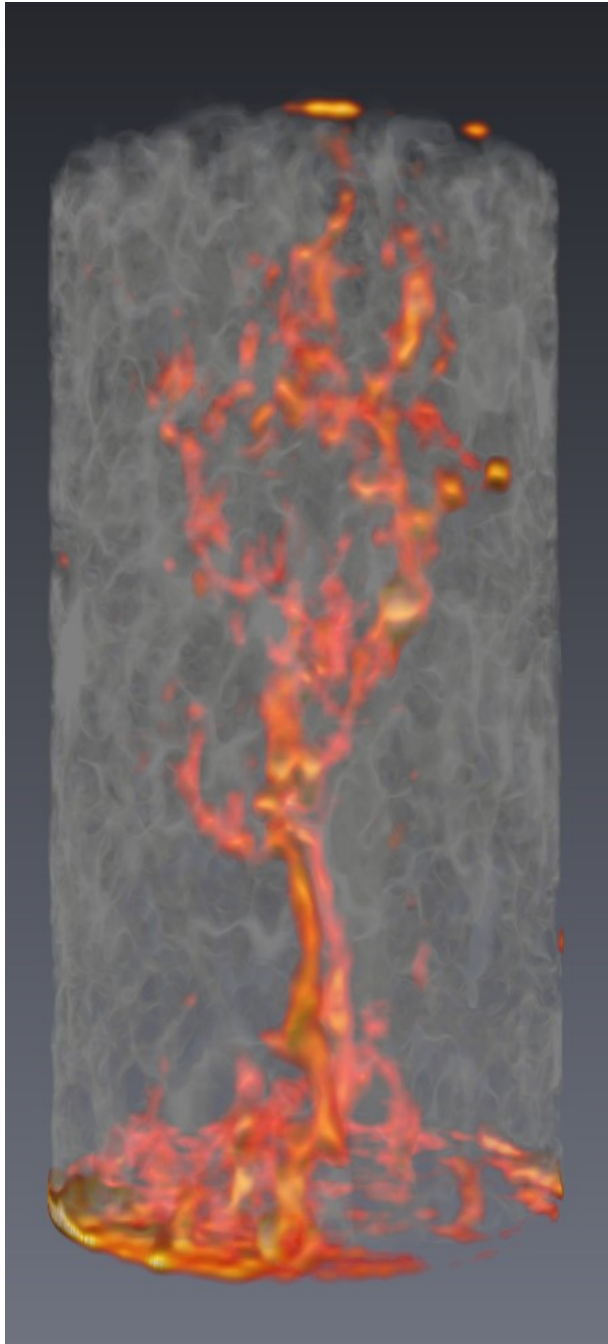
Figure 25: 3D visualization of the 3 RAT EU_06 experiment. Red represents change in pore space. Channeling is pronounced, though there is not one dominating wormhole formed. Picture was made by Holger Ott, using Avizo image processing software.
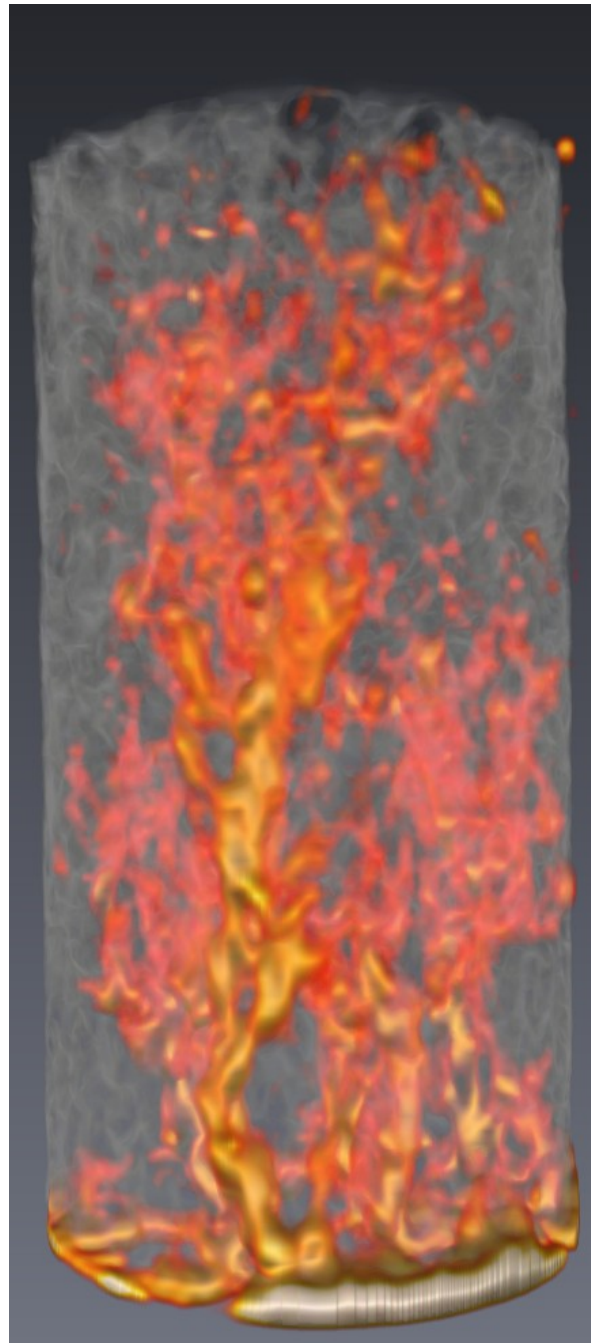
Figure 26: 3D visualization of the 6 RAT EU2_01 experiment. Red represents the change in pore space. Homogeneous dissolution is more pronounced. Some channeling is still occurring. Picture was made by Holger Ott, using Avizo image processing software.

It is evident that more acid exposure leads to a significant increase in porosity. The CT scans confirms the observed wormholing at the inlet (bottom of the pictures) and the less altered outlet. Despite the wormholing at inlet and the outlet effect, the 6 RAT sample show strong indications of homogeneous dissolution in the center part of the sample. The 3 RAT sample however, show tendencies of pronounced channeling. This could give reason to discard the sample. Further assessment of this sample should therefore be done carefully. Channeling is still occurring in the 6 RAT sample as well, but no single dominant wormhole has formed. The channeling is not totally unexpected. As will be discussed shortly, having a slightly acidic solution at the time of saturation could have consequences resulting in the channeling.

As expected, some areas show more dissolution than others. Larger pores contain more acid thus the reaction potential is greater and more dissolution is therefore achieved. In addition, the injected acid always chooses the least path of resistance. If the permeability is high enough and the injected flow rate is too low, less permeable channels could potentially be left unsaturated with the acid. This could also cause pronounced growth of specific channels in the sample. This applies especially for micro pores. Eide [35] showed that larger pores grow faster and that there is a self-amplifying effect. Although this was shown for dynamic conditions, e.g. acid flooding, the same effect applies to some extent in static conditions. Larger pores accumulate more solution and acid, having a greater reaction potential and hence, more dissolution is expected. This allows us to predict what regions will be altered the most. Translating this into field scale, enhanced alteration is expected in regions with higher porosity. This implies that some channeling also could occur in the reservoir and therefore still make our results reasonable as simulation of subsurface processes.

8.2   Attenuation analysis

The image-process software ImageJ [39] was used to measure the mean grey value in a specified area of the picture. This value, of course, depends on the contrast and brightness settings of the pictures. However, by keeping these settings constant for all images and look at the differences between pre and post scans, makes this method a quantitative tool. To avoid edge effects a small fraction around the whole sample is left out of the specified measuring area. As described in the experimental procedure, a total of 77 images were generated for a sample, each scan representing a certain position along the core length. The figures below show post CT scans, with adjusted thresholds settings, for EU_06 and EU2_01.
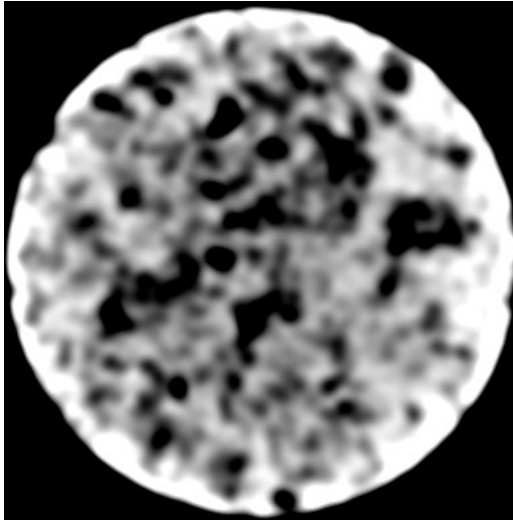
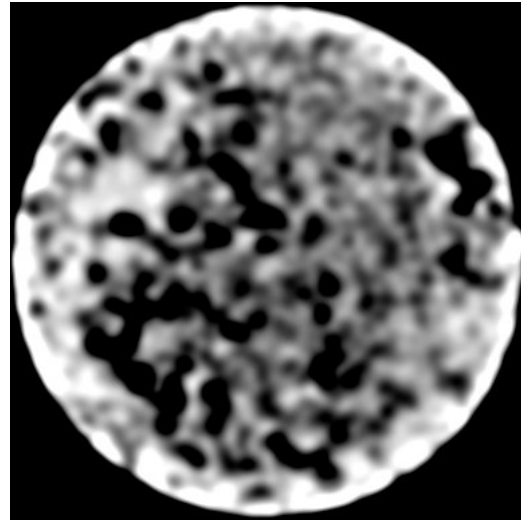**Figure 27: Cross section CT scan of EU_06.**

Figure 28: Cross section CT scan of EU2_01

The plot in Figure 29 shows the difference in absorption pre and post to the 3 RAT experiment, whereas Figure 30 shows the same plot for the experiment with 6 treatments. In both cases, we see the same inlet and outlet effects as mentioned above. Basically, the plots below can be divided into 3 regions, one at the inlet, one along the middle, and the last towards the outlet. At the inlet, we see a steep gradient that can be caused by end artifacts in the CT scan, or roughening of the cross section surface during core cutting. Roughening could create small pocket in which enhanced acid accumulation will occur, leading to more dissolution than elsewhere. Both inlet and outlet artifacts are taken into account by discarding two scans at both ends.

There is also a possibility that there is some reaction taking place during acid saturation. The injected solution has a pH of approximately 6.4, meaning that it is slightly acidic. This degree of acidity could induce a small reaction, buffering the solution completely before placement. Due to the high reaction rates [35], the reaction is fast and will only take place at the inlet, hence the steep gradient at the inlet. By only discarding one scan at the inlet, the gradients become even steeper, supporting the reaction hypothesis. In the wormhole study by Eide [35], a steep gradient at the inlet was also observed. Despite the fact that the gradient was significantly steeper, considering that a strong acidic solution was injected in this case, indicates that our week acidic solution could cause the small gradient relative to Eide's, at the inlet. High calcium concentration in the effluent after acid flooding could potentially indicate whether a reaction takes place during the saturation process or not. This is addressed in more detail at a later stage.

The next section, middle part of the plots, clearly shows that the difference becomes more or less constant, which suggests that the amount of dissolution is similar in this part of the core. Even though the difference is constant, one is not able to determine if the dissolution pattern is homogeneous from the plot alone. Eide showed that formation of a dominant wormhole throughout the core sample would also show up as constant difference in a similar plot. However, in combination with the CT scans, the dissolution pattern seems to be close to homogeneous for the 6 RAT sample. The self-amplifying growth effect that larger pores have implies that a perfect homogeneous dissolution, meaning that all pores are enlarged at equal rate, will never occur, neither in the laboratory nor the reservoir. In order for perfect homogeneous dissolution, all pores must have the same size and shape.

Figure 29 also indicates an increase in grain volume close to the outlet. The acid-rock interaction takes place at elevated temperatures and the retarded acid becomes buffered. As the sample is cooled afterwards, temperature change could disturb the equilibrium. The solubility product of calcite, the prime mineral in Euville, is slightly reduced with a decrease in temperature [35]. This reduction, together with other mechanisms could cause precipitation of loose particles in the pores. Introducing water for cleaning purposes could cause further disturbance in the equilibrium and more precipitation. The precipitation has a certain time delay, resulting in more precipitation at the outlet. In combination with pore throat blockage, accumulation of loose particles could result in an increase of grain volume at the outlet, hence the increase in absorption.

Figure 30 shows the difference in absorption between pre and post for the EU2_01 sample subjected to 6 RAT. Again, a much stronger dissolution is seen at the inlet. From the visual observations, we see several wormholes at the inlet, which is consistent with the acid – rock reaction taking place at the inlet during saturation. Although there is a clear outlet effect similar to the 3 RAT experiment, the porosity decreases in contrast to the increase for the 3 RAT experiment. These inlet and outlet effects are also clearly visible on the 3D visualization figures, Figure 25 and Figure 26.
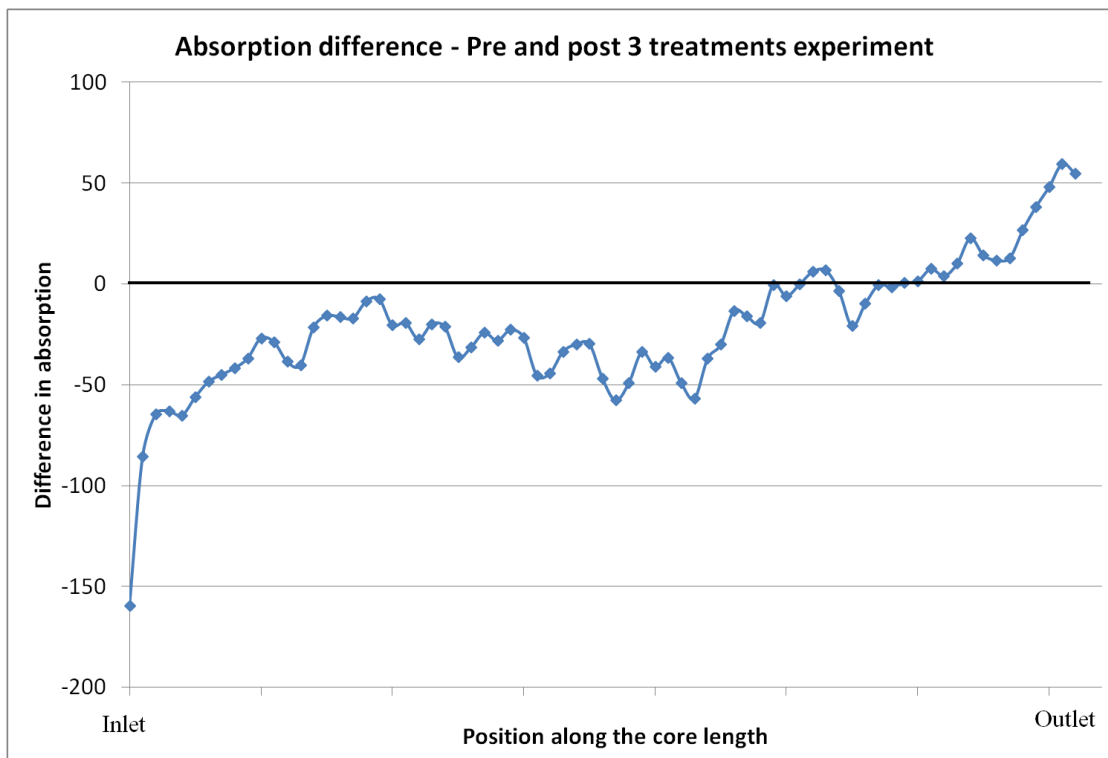
Figure 29: Showing the absorption difference between pre and post to three treatments along the core length. A decrease in absorption indicates a decrease in grain volume after the experiment. Inlet and outlet effects can also be observed.
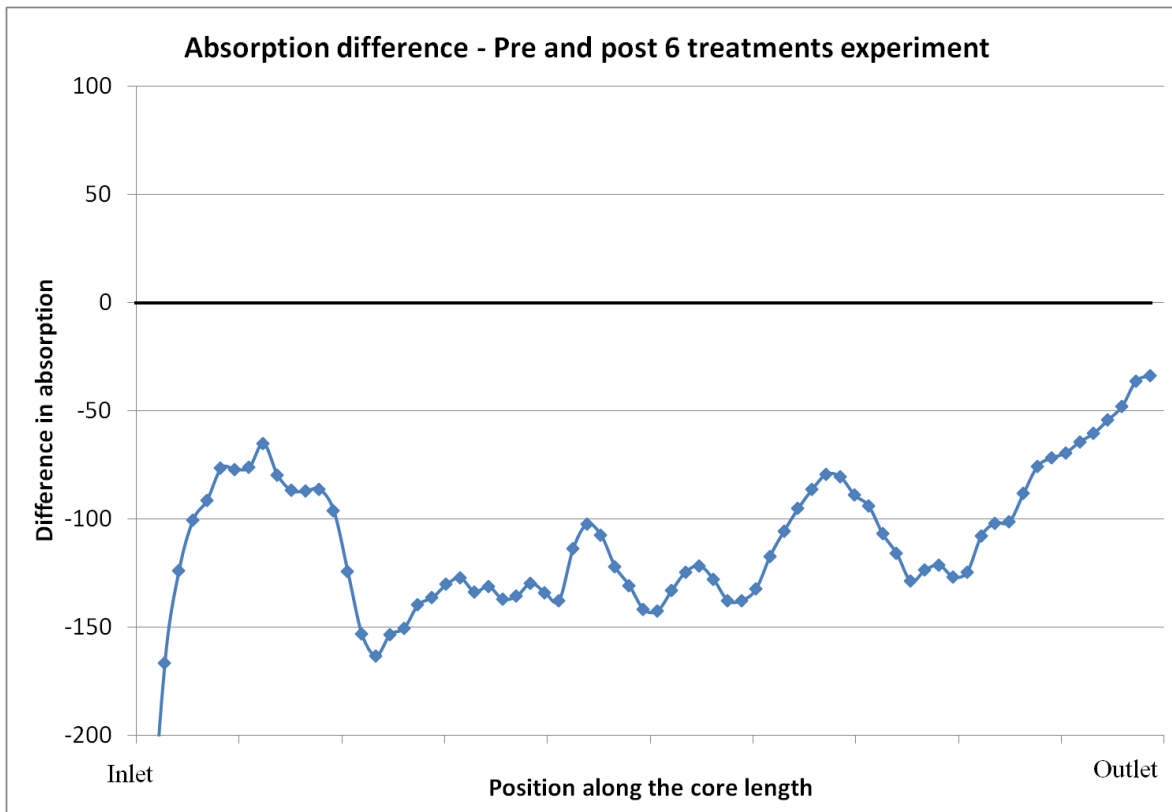
Figure 30: Showing the absorption difference between pre and post to six treatments along the core length. Negative difference implies a decrease in grain volume, hence an increase in porosity. There is significantly more dissolution than for the 3 RAT experiment. Inlet and outlet effects can also be observed here.

8.3   Effluent analysis: Calcium concentration

Eide [35] observed that, towards the end of the experiment the concentration of calcium dropped, suggesting an unbuffered solution. He explained this and showed that once a wormhole is formed, the growth is self - amplifying up to a certain point, at which the size becomes the limit. This size is called terminal size and is defined as the point where the advective flow is faster than the other reactive flow mechanisms (diffusion for fresh acid circulation to the wormhole walls) such that the solution does not get buffered. Once the wormhole has reached this size along the whole length, the concentration of calcium in the effluent will drop. Observing a drop in concentration during an experiment could potentially be an indicator of that a wormhole has formed.

This method is limited to dynamic acid treatments because advective flow must be present. The current experiment induces the reaction at static conditions over a long period of time. This allows the solution to completely buffer each time. The calcium concentration in the effluent is therefore dependent on how much dissolved carbonate we have during each treatment. The increasing porosity allows for more acid to be placed in the sample after each treatment, enhancing the reaction potential. One should therefore expect more dissolution as the porosity increases. However, this self-amplifying effect could possibly be negligible because of small increases in porosity from treatment to treatment.

In the current experiment, an effluent size of approximately 55 ml was taken. Table 17 contains the amount of calcium in grams registered after each treatment for all the experiments.

One sample of the effluent after acid flooding was also taken, in order to see whether any reaction takes place during acid saturation. We see that there is in fact 0.12 g of calcium in the effluent sample, suggesting some dissolution. However, this can also be explained by having residue from treatment that was not flushed out. Variation in the amount of Ca^{2+} could therefore be expected from treatment to treatment. As we see from Table 17, the amount of calcium in the effluent after each treatment varies to some extent.

Table 17: Amount of Ca^{2+} in grams after each treatment, together with the total amount of Ca^{2+} and the estimated total amount of dissolved calcite. The two latter estimations are based on equal Ca^{2+} concentration after all the acid floods.

Effluent id	EU2_01	EU2_02	EU2_05	EU2_07
Reference (Water) *[g]*	0.00			
1st *[g]*	0.10	0.22	0.26	0.15
2nd *[g]*	0.20	0.28	0.26	0.30
3rd *[g]*	0.34	0.30	0.25	0.31
4th *[g]*	0.31	0.32	0.25	0.31
5th *[g]*	0.28	0.32	0.31	0.29
6th *[g]*	0.25	0.30	**	0.28
Acid flooding* *[g]*	0.12			
Total amount of Ca^{2+} *[g]*	2.21	2.45	2.31	2.29
Total amount of $CaCO_3$ *[g]*	5.40	5.98	5.62	5.58

For calculation purposes, we have assumed an equal concentration of Ca^{2+} after all acid floods. Hence, for the total amounts six times the acid flooding amount is added.
**Due to spill of the last sample, the amount of dissolved Ca^{2+} is assumed equal to the average value of the other 6th treatment effluents when calculating the totals.*

The total amount of flushed water is somewhat higher than the approximate 3 PV after acid treatment. A slow water circulation is maintained during unloading/reloading, and during experimental standby. This could potentially result in missing out on a significant amount of calcium being flushed out from the sample. The total amount of flushed water varied from treatment-to-treatment and sample-to-sample.

Knowing the amount of calcium flushed out after each treatment, and by assuming equal calcium concentration after each acid flooding, expected total amount of dissolved calcite could be estimated. This is also presented in Table 17. Since we only know the post weight of EU2_01, we can only compare this to the calculations above. Table 17 gives total calcite dissolution of 5.4 ± 0.5 grams for EU2_01. This is significantly lower than the measured value of 8.9 grams. The big difference is mainly caused by: assuming similar dissolution after each acid treatment and the calcium being flushed out when not collecting effluent.

Estimating the weight and porosity change for the failed samples based on the effluent involves a lot of uncertainty and requires a significantly more structured and accurate monitoring of the effluent in order to be sustainable for this type of application. In later studies, an effluent sample should be taken after each acid flooding as well.

All effluent data can be found in the appendix.

8.4   Porosity changes

Eide [35] showed that utilizing ImageJ's feature of measuring the absorption, one could correlate it to the grain volume and porosity. The calculated porosity change was consistent with the measured value and the calculated value based on change in weight. The correlation between absorption and grain volume imply the following assumptions:

- 0 absorption implies pore space.
- a_0 and $V_{g,0}$ are the average total absorption value and grain volume prior to the treatments.
- a_1 and $V_{g,1}$ are the average total absorption value and grain volume prior to the treatments.

The change in porosity and mass can then be derived from having:

$$a_0 - a_1 \propto [(1 - \varphi_0) - (1 - \varphi_1)] \tag{54}$$

$$\Delta a = a_0 - a_1 \propto [\varphi_1 - \varphi_0] = \Delta \varphi \tag{55}$$

The absorption difference is normalized by:

$$\frac{\Delta a}{a_0} = \frac{a_0 - a_1}{a_0} = \frac{\varphi_1 - \varphi_0}{1 - \varphi_0} \tag{56}$$

yielding a porosity change described by:

$$\Delta \varphi = (\varphi_1 - \varphi_0) = (1 - \varphi_0)\frac{\Delta a}{a_0} \tag{57}$$

The change in mass is directly related to the change in grain volume and is given by:

$$\Delta m = \rho_s \int (\varphi_1 - \varphi_0) dV = \rho_s \int (1 - \varphi_0)\frac{\Delta a}{a_0} dV \tag{58}$$

The calculated results, both for the 3 RAT and 6 RAT experiment, can be seen in Table 18. The table also contains the measure porosity and the estimated one based on weight change. In the core analysis, density is measured independently of the weight. What we see is that the total change in density is consistent with the change in weight.

Table 18: Porosity measurements form core analysis and estimations based on absorption and weight change.

Sample id	# RAT	Initial porosity	Final porosity			
			Measured	*MICP*	*Based on weight change*	*Absorption*
EU_06	3	16.5	16.9%	17.1%	17.5%	17.4%
EU2_01	6	16.9	19.9%	19.3%	20.8%	20.9%

It is clear that acid treatments are inducing porosity changes. The consistency of the weight based final porosity and the absorption based, is good in contrast to the measured one. The potential of losing grains during build out and transportation is large, and could affect the weight change significantly. The estimated porosity change based on weight difference is very sensitive to this uncertainty. This applies especially for the 6 RAT samples because the sample gets very fragile around the edges. Since weight and absorption is related, these uncertainties are also reflected on the absorption-based estimate. The loss of grains is most likely causing some of the difference seen between the measured and weight based porosity. As an example, for the EU2_01, the difference in porosities implies a total additional loss of grains corresponding to 2.5 grams. It is very unlikely that this amount of grains is lost thus only partly explaining the porosity variation. The measured porosity is assumed to be the most accurate and therefore applied in other application in the current project. However, by taking the error of ±5 % into account could result in more consistency.

Our measured results from the 3 and 6 RAT not subjected to failure do not show consistency with IFP's results. While IFP [38] states that the porosity increase is directly proportional to the number of treatments, our results suggest otherwise. We see a higher increase going from 3 to 6 RAT than from untreated to 3 RAT. However, a final conclusion is difficult to make based on only having one 3 RAT sample in addition to the pronounced channeling seen for that sample in the current project.

Having a non-linear increase is not that unlikely though. Each treatment results in an increase in porosity, allowing more acid to be placed in the sample. More acid implies that more reaction could take place and therefore increase the porosity even more. According to this assumption, one should have a constant ratio of dissolved material per volume acid placed in the sample between each experiment. The ratio for the 6 RAT is of a factor 3.5 higher than in the 3 RAT experiment. This suggests that other factors influence the dissolution grade. Inability to continuously monitor the porosity, limits the assessment of the porosity evolution. More significant changes could cause the evolution to also change. As was discussed in the previous section, the effluent from the flushing after treatment can in theory be used for monitoring the calcite dissolution and hence the porosity increase. However, the method involves a lot of uncertainty and the error is large, making it difficult to apply.

There are several other known and unknown factors that can cause a non-linear increase in porosity with respect to treatments:

(i)   Higher initial porosity allows for more acid to be placed in the sample during the first treatment, resulting in a bigger increase in porosity. The self-amplifying effect is then causing a non-linear growth.

(ii)   Rock mineralogy: although the samples are from the same formation, small variations in the mineralogy and cementation. As mentioned earlier, EU_06 is from another batch implying that the mineralogy can vary more.

(iii)   Fluid effects: potassium format was used to buffer the retarded acid at ambient temperatures (23 ℃). The amount of salt required for obtaining the same pH for the injected solution for each treatment varied.

(iv)   Uncertainties in the measured pH of the solution before injection due to pH meter inaccuracy.

Taking everything into account is very difficult and approximations are therefore required in order to make more general conclusions and models. Rocks are very heterogeneous and, as already mentioned, laboratory experiments only represent a very small fraction of the whole formation.

8.4.1 Porosity change as a function of core length

CT scans can be applied to calculate the porosity as a function of the core length. Figure 31 shows the porosity for the pre and post sample for the three treatments case, whereas Figure 32 show the same for the six treatments case. The plots only confirm what have been discussed earlier. Inlet effect can be seen, and a higher number of treatments result in higher porosity increase. They also show the more or less constant porosity increase throughout the core sample.

Comparing our CT scan porosity plots with IFP's (Figure 33 and Figure 34), we see further similarities. What differ in the results are the effects that we see at the inlet and outlet and also that our 6 RAT treatment results in a more significant increase in the porosity. IFP seems to have a more homogeneous porosity change throughout the whole core. This could be explained by that we still have a slightly acidic solution during saturation. Whether this is the case for IFP does not come out in their report. For future studies, I recommend that: a neutralized retarded acid should be used, achieved either by adding more potassium format salt, or running the solution through carbonate before injection. This could eliminate inlet effects.

Porosity - Pre and post 3 treatments experiment
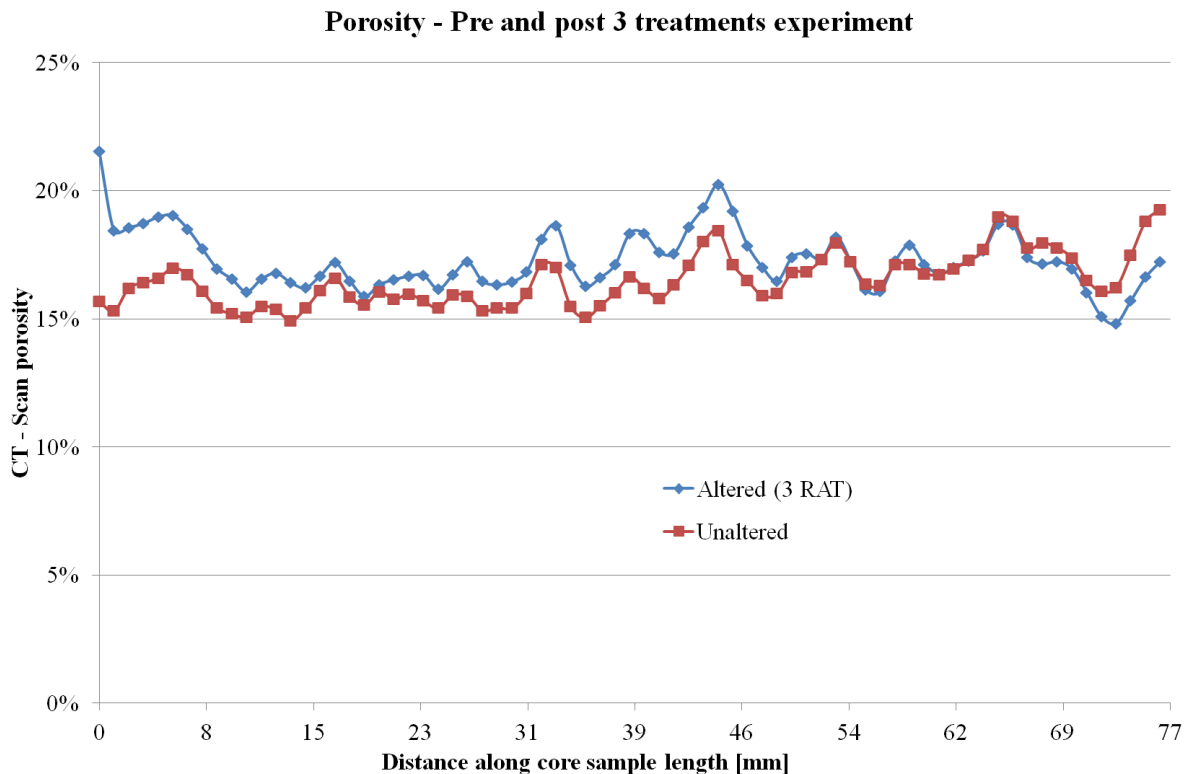
Figure 31: Porosity calculated from absorption as a function of core sample length pre and post experiment for 3 RAT.
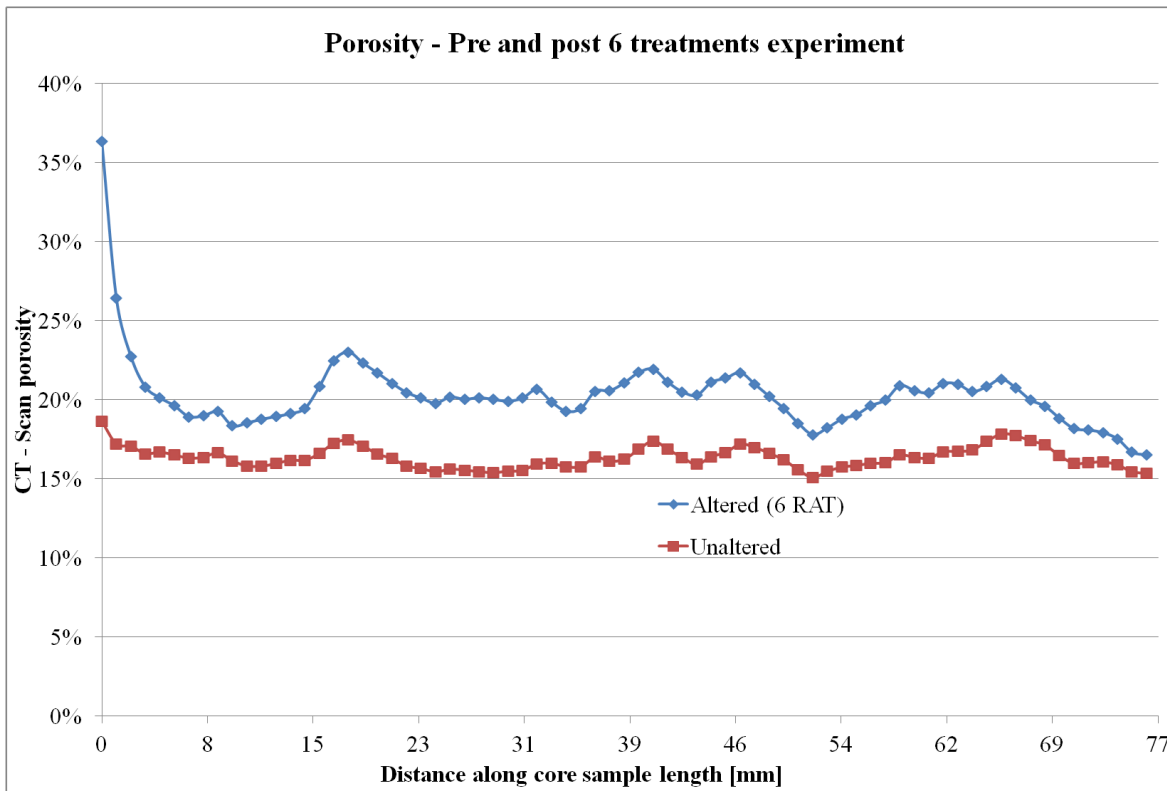
Figure 32: Porosity calculated from absorption as a function of core sample length pre and post experiment for 6 RAT.
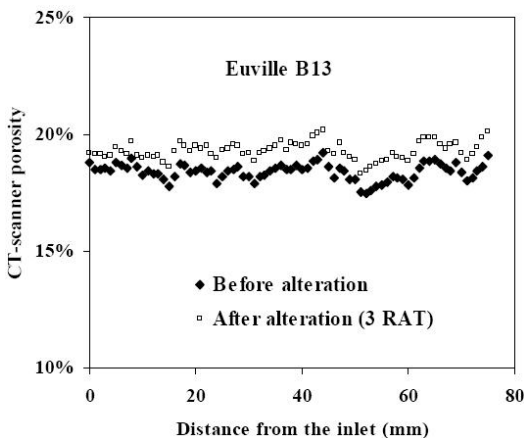
Figure 33: IFP's CT scan porosities (3 RAT)
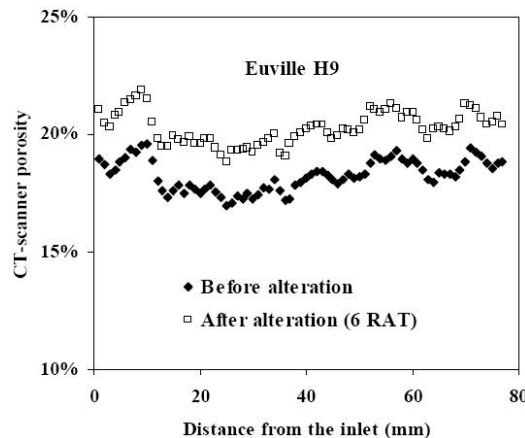
Figure 34: IFP's CT scan porosities (6 RAT)

8.4.2   Porosity of the failed samples

The samples subjected to failure could not be post CT scanned, and measuring porosity based on buoyancy in chloroform is not valid because of the generated cracks during failure. From the inconsistency between the different methods of estimating the porosity change makes the determination of the final porosity, for the failed samples, difficult. However, with the assumption of having an error of approximately ±10%, assuming similar change as for EU2_01 is therefore reasonable to assume. This is justified by the consistency in the effluent estimated

weight changes. This assumption has been made where it is found reasonable to apply it in the assessment of the results.

8.5   Pore size distribution – mercury injection

Mercury injection capillary pressure (MICP) measurements can be applied to determine the pore size distribution in a sample. The pore size distribution plot for the untreated Euville sample was presented in Chapter 6. MICP was performed on both the 3 RAT and 6 RAT, EU_06 and EU2_01 samples, after treatment. Figure 35 compares the pore size distribution for the 3 samples. We see that the number of micro pores is more or less unchanged, whereas the number of intermediate is increasing with treatment. The reason for unchanged number of micro-pores could be that the acid is unable to reach these pores due to capillary forces and isolation. The pores remain unaltered. The increase in intermediate pores is highly expected due to the acid alteration. Smaller pores are enlarged or merged with other pores to form intermediate sized pores.

What is noteworthy though, is that the number of large pores is also less affected, and also that it decreases a bit. This is most likely caused by the extensive enlargement of some pores, causing them to not be visible on the MICP. Some intermediate pores grow to the size of large pores, equalizing the change in this pore size range. In conclusion, a shift in the pore size distribution is observed, in which micro pores seems to remain more or less unaltered.
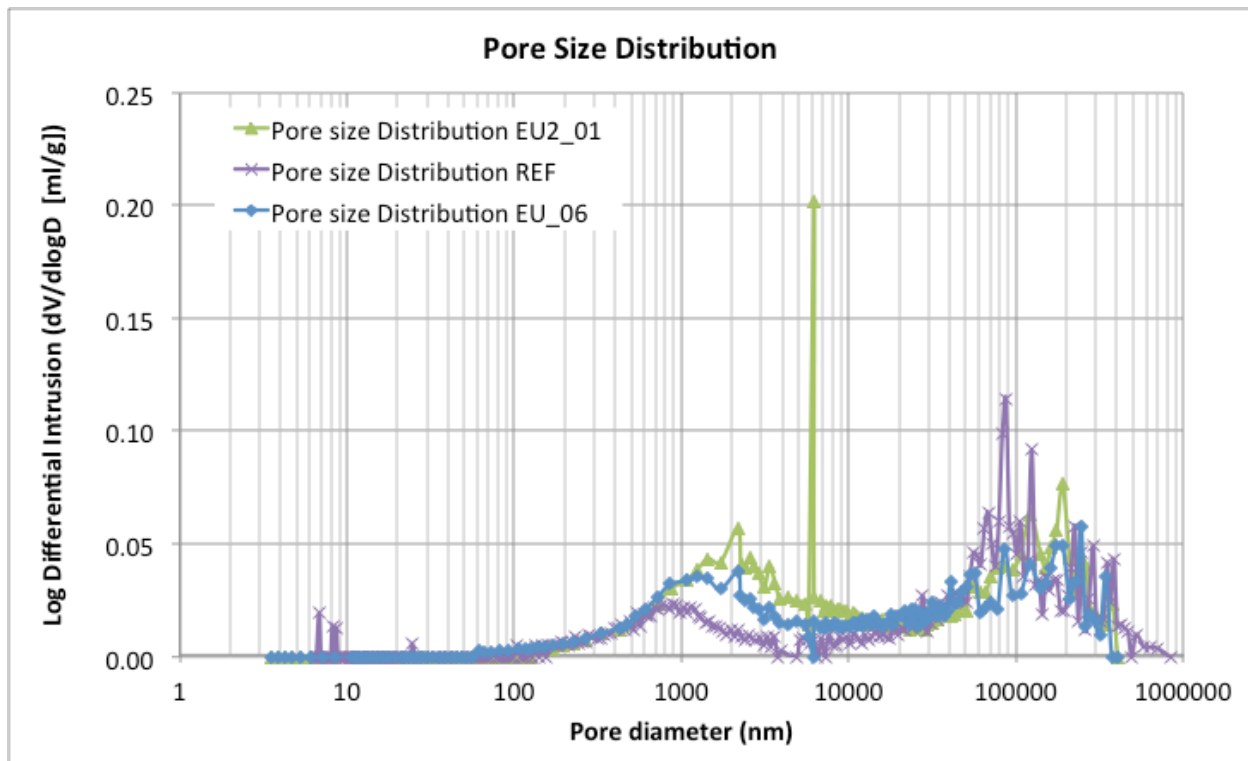
Figure 35: Comparison of the pore size distribution between untreated Euville, 3 RAT and 6 RAT Euville. A shift in the pore size distribution can be observed, having that micro pores seems unaffected and larger pores grows to a size undetectable by the MICP.

Pore size distribution is not the only result that can be obtained from mercury injection. Porosity is also measured, with the results presented in Table 18. Further on, when injecting the non-wetting mercury phase air is drained from the sample and the capillary drainage curve (P_c-curve) is obtained. **Figure 36** show the drainage curve for the two treated samples compared to the reference sample. The reference curve indicates a threshold pressure of approximately 0.0035 MPa. Complete mercury saturation is obtained at ~ 20 MPa. For EU_06 (3 RAT) and EU2_01 (6 RAT), we see a threshold pressure of 0.0039 MPa and 0.0036 MPa, respectively. Complete mercury saturation is obtained at ~ 40 MPa and ~ 15 MPa. One should expect both threshold pressure and full mercury saturation pressure to decrease with treatments because of increasing pore size, thus less force needed for intrusion. The threshold pressure seems to be less affected by the alteration, whereas a significant decrease in complete saturation pressure can be observed. Larger pores and enlarged pore throats enables the fluid to penetrate the rock more easily. Having that the reference is from an older batch of Euville could explain that the threshold pressure and complete saturation pressure are not in line with EU_06 and EU2_01.
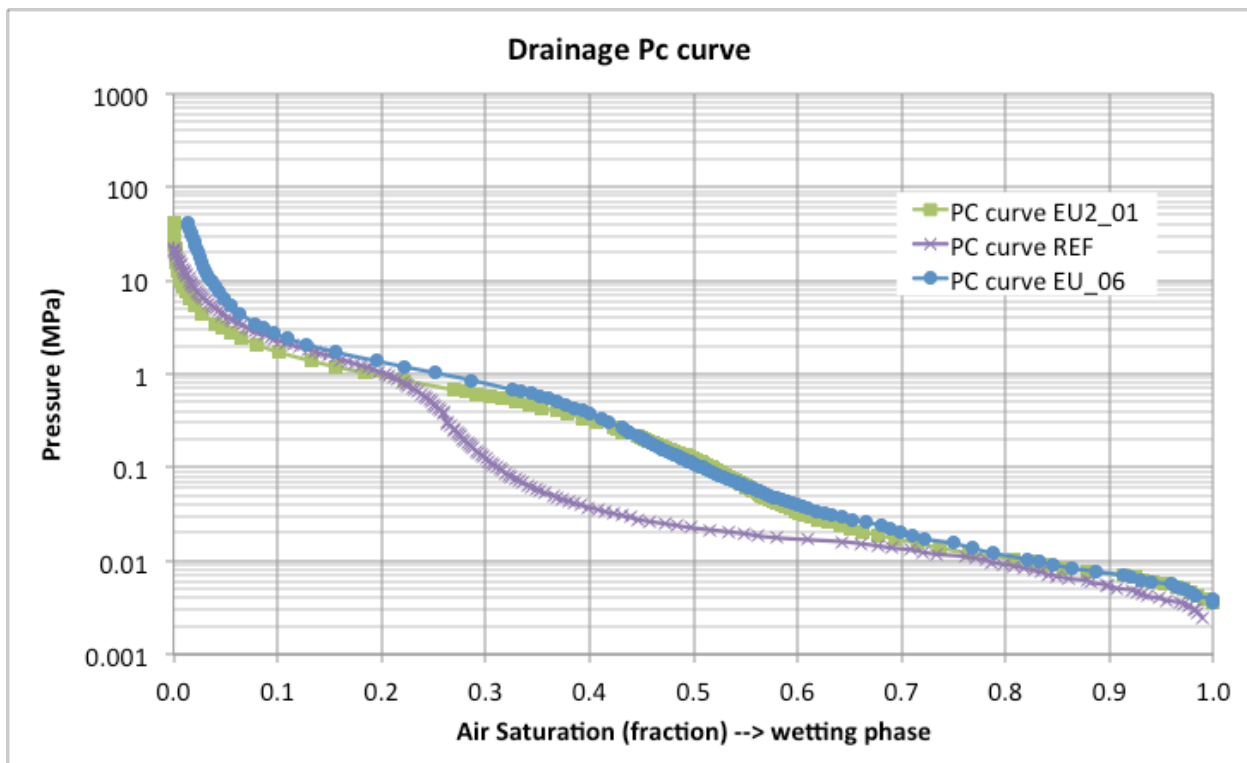
Figure 36: Comparison of the capillary drainage curve for EU_06 (3 RAT) and EU2_01 (6 RAT) with the untreated reference sample. Having that the reference sample is from an older Euville batch explains the differences seen from the other two samples in terms of threshold pressure and complete saturation pressure. The trend between 3 and 6 RAT do however suggest a significant decrease in complete saturation pressure. Threshold pressures seem to be more or less unaffected.

8.6   Permeability changes

We have performed two different permeability measurements: (i) prior and post to the experiments according to the procedure described in Section 6.2.2 and, (ii) according to step 6 in the experimental protocol. The latter is done under *in situ* stress conditions, whereas the first

method is done at isostatic stress conditions (30 bars). Applying high stresses to the sample could cause micro-fractures to close that otherwise would have contributed to a much higher permeability. The results from both methods are discussed below, but the absolute values are not comparable.

Comparing the permeability at *in situ* stress and lower stress conditions indicates that there is indeed a difference, ranging from 30 to 50% lower permeability at *in situ* conditions. The lower permeability measured in the creep cell is also subject to pressure drops in tubes etc. Permeability increase is highly expected. The pore throats are important in terms of permeability. Even though the pores are big, having a narrow pore throat will have a negative effect on the permeability. Retarded acid is also placed in the pore throats during saturation, implying that dissolution also will occur here, enlarging the throat and hence, contribute to increased permeability. An exponential increase in permeability is not unlikely due to the self-amplifying effect in the pore throat growth. As the throat grows, more acid is placed inside allowing for enhanced growth. The permeability change is very sensitive to different effects that can occur during one treatment cycle. Loose particles can plug pore throats during one cycle while being opened again at a later stage, explaining the scatter in the data.

Figure 37 show the evolution of the normalized permeability for all the experiments, both the 3 and 6 RAT and the failed samples. Note that these are estimated based on method (ii) hence the uncertainties related to this method mentioned above, applies.

Since this method does not require building the sample out, and is performed throughout the experiment, failure experiments can also be included. As stated in the experimental procedure, different rates were used for calculating the permeability. The average permeability values for these rates are used in Figure 37. Monitoring the permeability after each treatment gives the benefit of observing the evolution of the permeability, whereas the measurement according to (i) only gives pre and post values. The general observation is that there are a lot of uncertainties and scatter in the measured permeabilities. We can even see that the permeability falls below the initial value for some of the experiments both under and after the experiment. The estimated permeability for each rate varies significantly; hence the error is large being approximately ± 78 mDarcy based on standard deviation. A more detailed overview of the estimated permeabilities can be found in the appendix.

Despite no clear trend in the permeability evolution from treatment to treatment, an increase in permeability is seen. Expanding pore throats is a reasonable explanation, reducing the resistance that the pore throats have on the flow. The 3 RAT permeability evolution differ from the other samples. This could be explained by the pronounced channeling that was observed from the CT scans. Eide showed that for wormholing, a rapid increase in permeability was seen, before the wormhole reached a terminal size, resulting in a diminishing effect on the permeability increase.
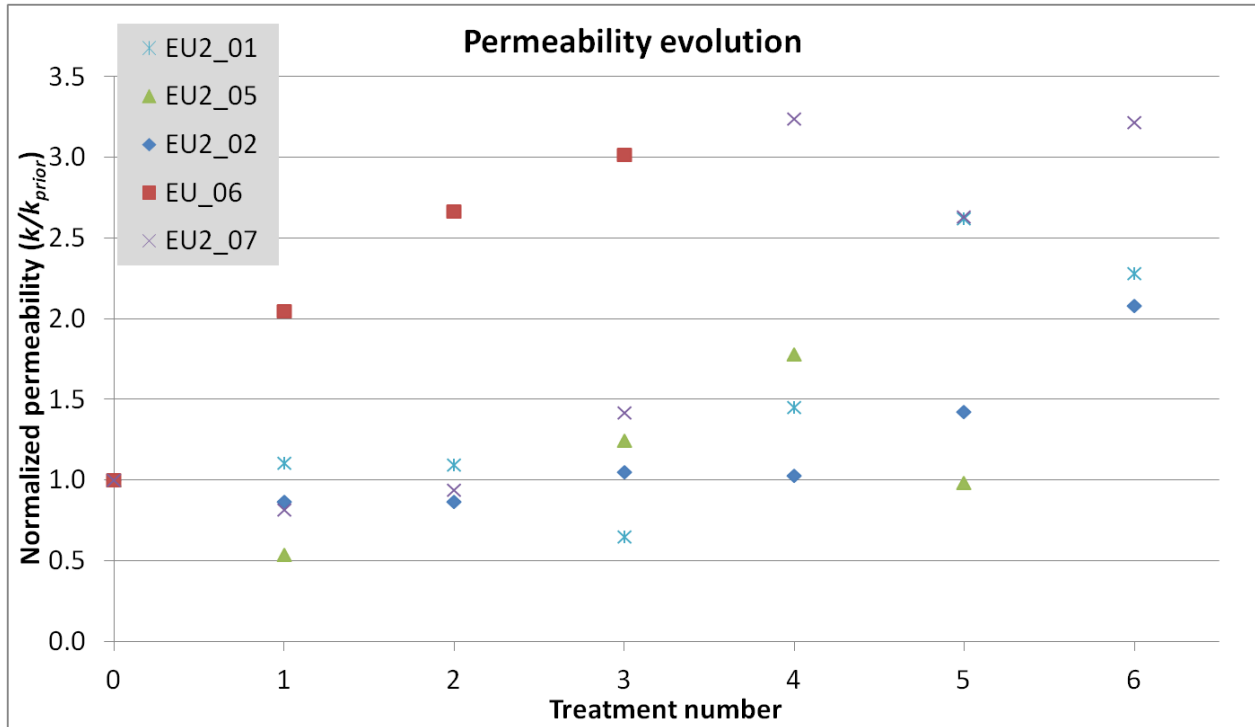
Figure 37: Normalized permeability evolution for all the treatment experiments. We see that there are a lot of dispersion and the error large.

Because only one of the 6 RAT samples was built out without failing it first, one pre and post permeability measurement at isostatic conditions (30 bars) are available for the 6 RAT experiments together with the 3 RAT experiment, see Table 19.

As Eide showed, the permeability evolution in the case where a wormhole forms is much more significant. An increase of almost 13 Darcy, measured according to (i), was seen for the wormholing case, whereas for the 3 RAT and 6 RAT was ~2.5 Darcy. The result of having less permeability increase suggests that a more homogeneous alteration is induced.

Table 19: Permeability measurements (mDarcy) prior and post to the experiment at hydrostatic conditions (30 bars).

#RAT	Prior to experiment	Post experiment
3	190 ± 19	2750 ± 280
6	266 ± 27	2798 ± 280

Having no clear trend in the permeability increase is consistent with IPF's [38] permeability results. However, they concluded that the increase in permeability going from 3 to 6 RAT is much more significant than from unaltered to 3 RAT. The porosity change with respect to sample length showed that the outlet was less altered. This end effect could create an uncertainty in the overall permeability increase, because the cross section with the lowest permeability will determine the overall axial permeability. It is also noteworthy that there is no correlation between the increase in porosity and permeability. The results suggest that the initial porosity increase is contributing significantly more to permeability increase with a diminishing effect as the porosity continues to increase. This could be caused by that the initial increase in the pore throats are much more effective on the permeability compared to the growth effect after a certain size of the throats is reached. Most likely, having similar permeability for the 3 RAT and

6 RAT is caused by the wormholing in the 3 RAT sample. The permeability has increased significantly faster than what would have been the case if a more homogeneous dissolution is present.

In terms of assessing the permeability change, the most reasonable and accurate values are the ones obtained from core analysis, Table 19. The core is properly cleaned and measurements are done at the exact same conditions. In conclusion, the permeability increases is significant. Due to the pronounced channeling seen in the 3 RAT case, drawing a conclusions with respect to higher initial permeability increase compared to later in the treatments, is difficult. This requires further studies, e.g.: build out and determine permeability for each number of treatments. There are however, indications of having a higher permeability increase in the first treatments, which is supported by showing consistency with previous work.

In terms of consequences due to permeability increase in the reservoir, enhanced water influx from surround aquifers could induce a faster and higher grade of disturbance in equilibrium of the reservoir solution. In addition, reactive flow is necessary for a reaction to take place. Increasing the permeability, which is an important factor for reactive flow, could enhance reactivity in the reservoir. As discussed in Chapter 3, once the CO_2 saturated brine settles in the reservoir, it has become more or less buffered. Further reaction and possible dissolution of the reservoir rock occurs if there is a disturbance in the equilibrium.

8.7   Stiffness alteration

It should be noted that the core samples are only a small representation of the whole rock. Localized propertied can change within a rock, thus causing the absolute difference seen between each of the samples. The sample subjected to 3 RAT was obtained from another batch than the 6 RAT samples explaining the more significant difference in properties. Samples from the same batch can also vary. The initial Young's modulus for EU2_05 was measured to be around 7 GPa lower than for the others. An absolute comparison is therefore difficult. There are also a number of uncertainties in the final porosity of the failed samples.

Carbonates are considered to be linear elastic, implying that the properties should be nearly independent of the confining pressure. Despite the linearity, we choose to only compare moduli estimated at *in situ* conditions, because of the deviation from this theory. The drained unlading/reloading cycles performed prior to the first treatment and after each treatment enable us to estimate the drained frame moduli: Young's modulus, Poisson's ratio and the bulk modulus. The moduli can be determined either from the unloading or reloading part. Due to some deviation from linear elasticity, these two methods will result in slightly different values, thus we have chosen to consider the average value. The difference between the average values and the unloading/reloading values is accounted for by an error of $\pm 10\%$. In addition to being based on experience, this error reflects some of the

Chapter 3 also discusses that hysteresis depends on the rock stiffness. Weaker rocks have the tendency of showing much more hysteresis and falling in the permanent deformation domain. Figure 38 shows the stress strain path during the unloading/reloading cycle prior to treatments for EU2_01. The hysteresis effect is less clear form this figure, suggesting that the rock is stiff and behaves linear elastically. Figure 39 shows the stress–strain path for EU2_01 after 6 RAT. Hysteresis is more evident which indicates enhanced plastic deformation. If a loading/unloading cycle had been used instead, plastic deformation, which is seen in the figures, would cause more compression after the stiffness measurement. This is not desirable, hence making an unloading/reloading cycle more suitable.

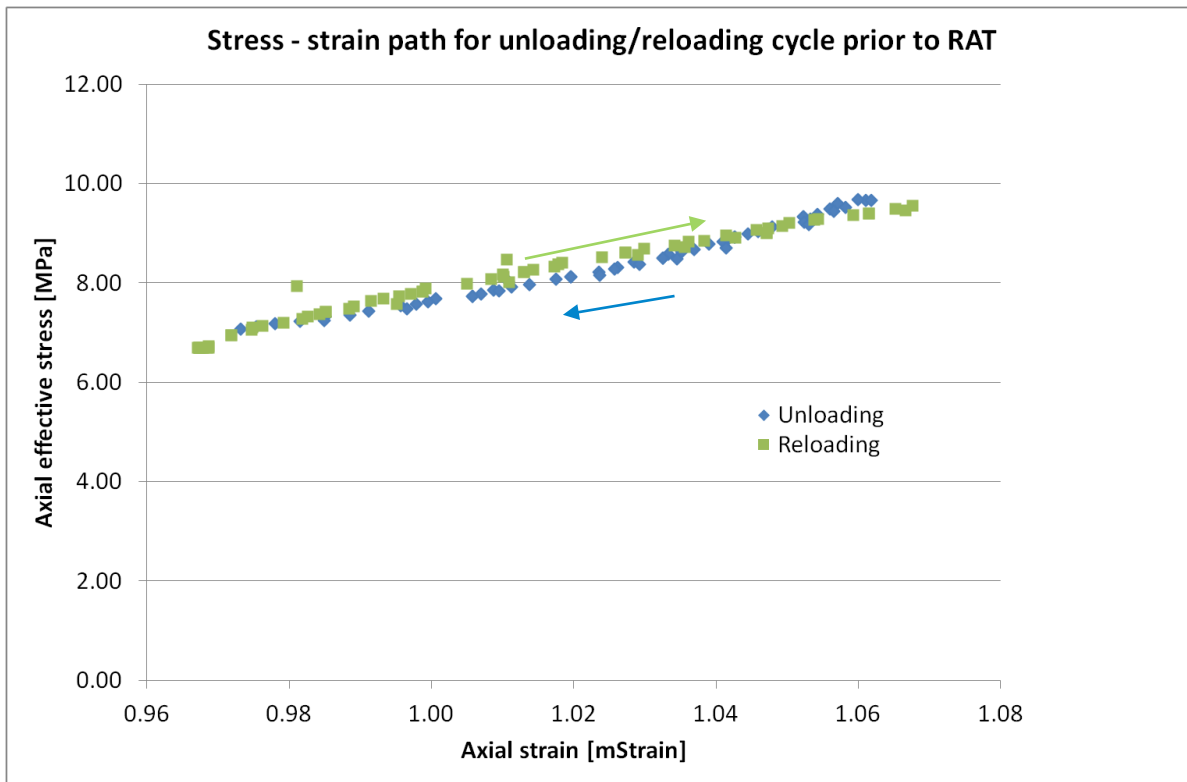**Figure 38: Stress-strain path during unloading/reloading cycle prior to treatment for EU2_01. Hysteresis is less clear, suggesting a stiff rock.**
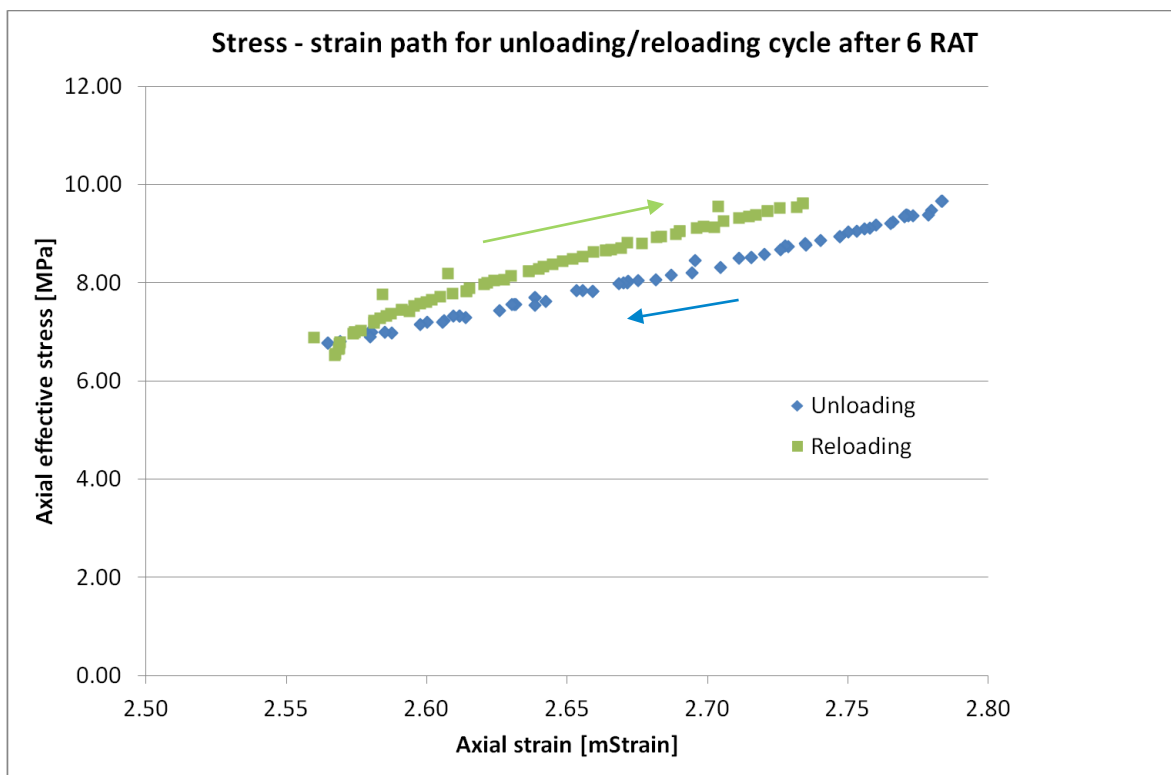
Figure 39: Stress-strain path during unloading/reloading cycle after 6 RAT for EU2_01. Hysteresis has become more evident and initial and final strain level is different, indicating plastic deformation and weakening of the rock.

Figure 40 shows the stress strain path after each treatment, going from prior to treatment on the left to after 6 RAT on the right. Unloading path is on the right, while the reload path is on the left. Again, hysteresis increases with each treatment meaning that the rock becomes softer. It is difficult to determine where the linear behavior is occurring. The slope is clearly different at the initial stage of both unloading and loading part. However, frictional effects present in the apparatus give reason to believe that the steeper slopes at the initial stage are a result from overcoming these. When estimating the stiffness moduli, adjustments on which points to include has to be done because the trend lines are sensitive to offset error points. Determining whether the unloading or the reloading part is the correct path to use is also something that has to be taken into account. The estimated values can differ significantly, depending on the amount of hysteresis. As the experimental results in Chapter 7 shows, the unloading and reloading values are differing significant, as for EU2_01 is expected according to the stress-strain path evolution. One should be careful and critical when choosing. Comparing Figure 38 and Figure 39, less and less elastic behavior is seen for both the unloading and reloading, making the uncertainty more significant. In the last experiment, two uniaxial unloading/reloading cycles were performed after each treatment to see whether the second cycle would reduce some of the plasticity. However, the second cycle showed similar behavior as the first cycle. We have therefore chosen to use the average values for more detailed assessments and applications.

The same stress-strain trends can also be seen for the other samples.
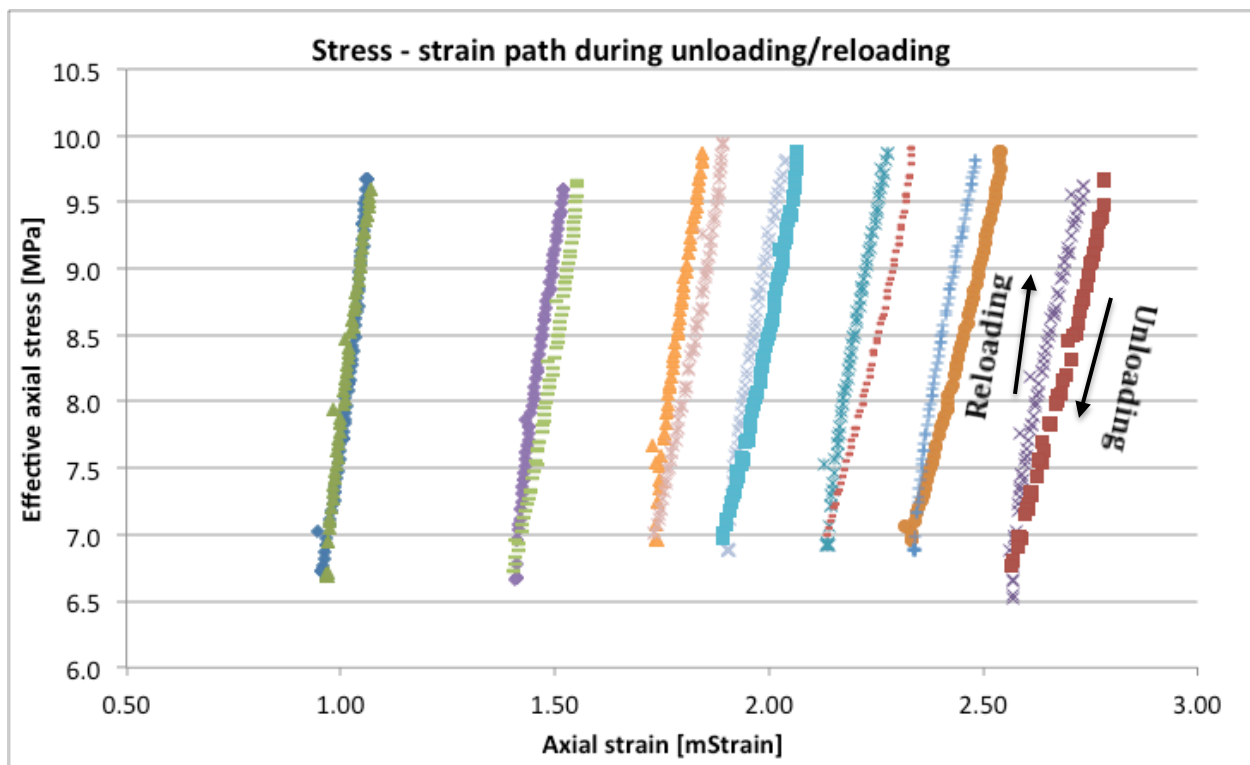
Figure 40: Stress-strain path for unloading/reloading cycle after each treatment going from prior on the left to 6 RAT on the right. The unloading path is on the right, whereas the reloading path is the left one, applying for each cycle. Hysteresis increases with the treatments.

8.7.1   Stiffness as a function of acid treatment

In the current project, absolute values are of less interest, whereas the main focus is on the trends seen between each treatment. Figure 41 to Figure 44 show the different moduli and the

Poisson's ratio with respect to treatment number. As mentioned in the very beginning of this chapter, estimated values are assumed to have an error of $\pm 10\%$. Despite having a systematic error of 10%, the trend remains the same. Isostatic unloading/reloading cycles, for measuring the bulk modulus, resulted in unexpectedly low values due to some strange behavior of the radial displacement during the cycles. We have therefore chosen not to include these in the assessment. However, it should be noted that the relative changes are similar as to the calculated bulk modulus based on Young's modulus and the Poisson's ratio.

It is also noteworthy that several of the samples experience jumps in the different moduli. However, the overall trends suggest that the acid treatment is softening the rock. The jumps can easily be seen in Figure 41 to Figure 44. A reason for these jumps could be that minor pore collapse events occur. Vugs, large pores and channels can cause localized failure in the sample during unloading/reloading cycle. This could result in a sudden stiffening of the rock. Despite some fluctuation in the evolutions, the general observation is that all moduli are significantly reduced with a diminishing rate as the rock is treated, suggesting that the largest effects are seen initially of the acid exposure. The same behavior is seen for the 3 RAT test and the failure tests.
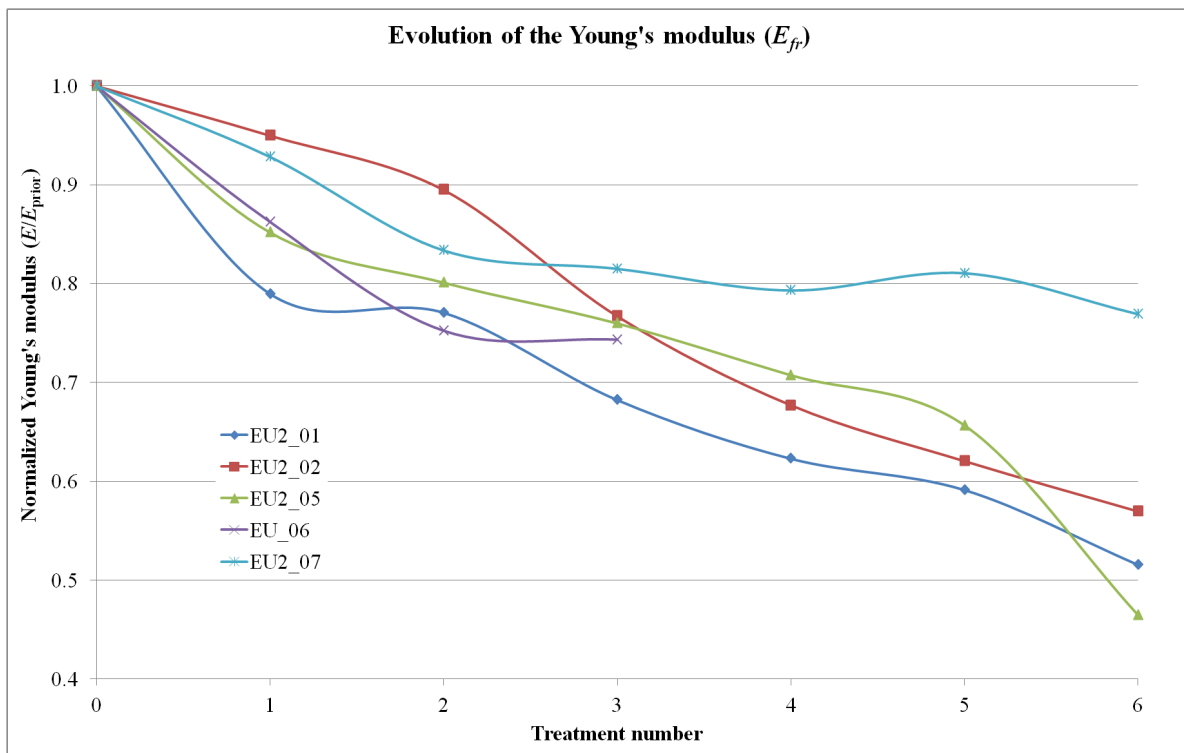
Figure 41: Evolution of the Young's modulus with respect to treatment. The trend is clear for all samples. Acid treatment reduces the Young's modulus and hence the stiffness, significantly.
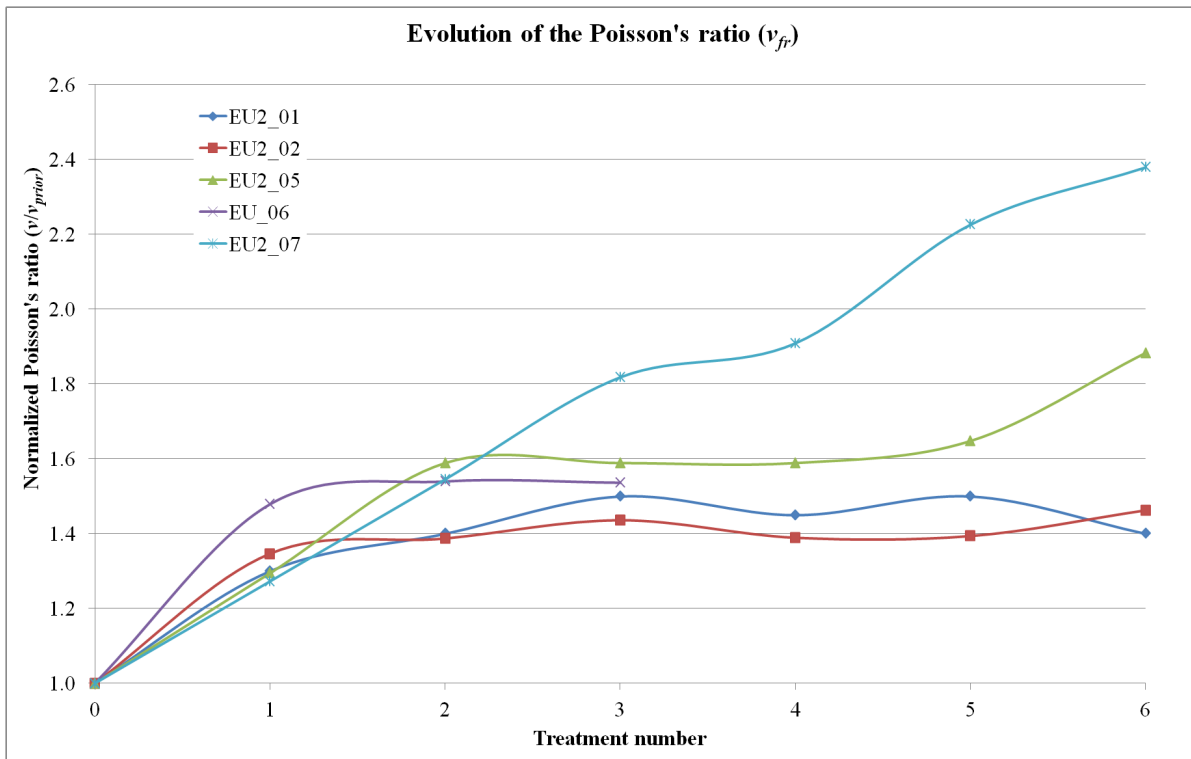
Figure 42: Evolution of the Poisson's ratio with respect to treatment number. The Poisson's ratio increase significantly as the rock is dissolved.
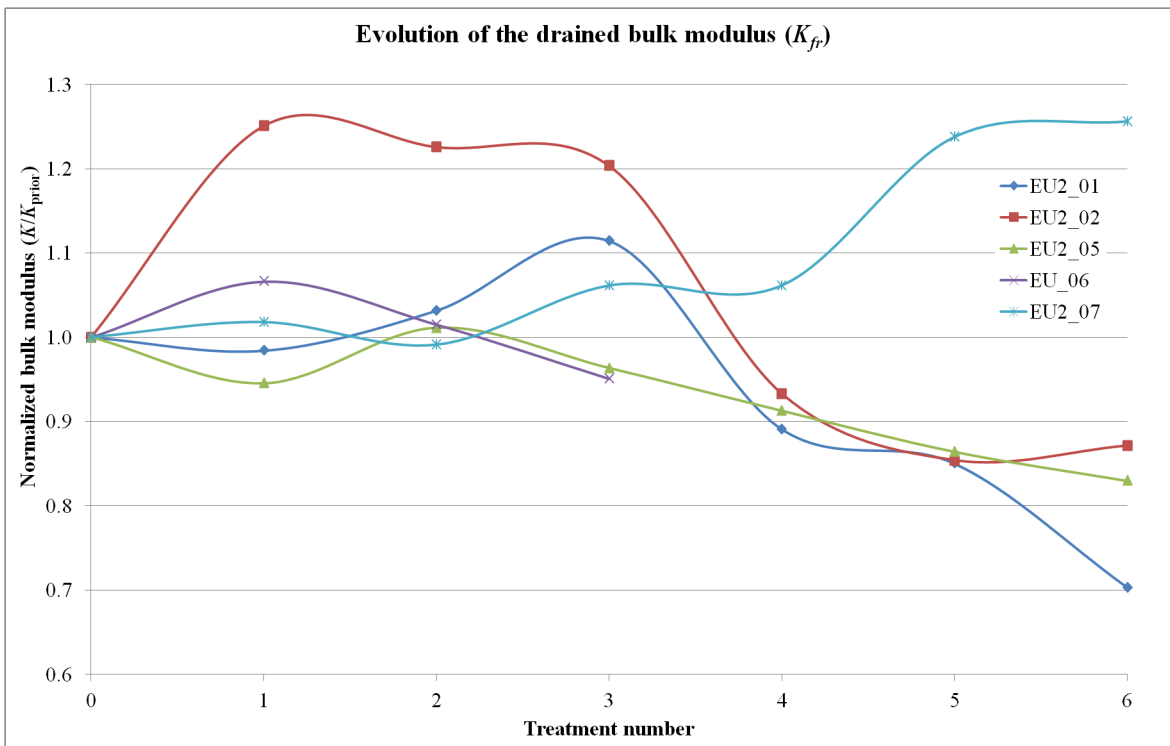
Figure 43: Evolution of the drained bulk modulus with respect to treatment number. Fluctuations can be seen, which could be caused by pore collapse, closing of fractures and vugs, making the rock stiffer. The overall trend is that stiffness is reduced due to acid treatment.
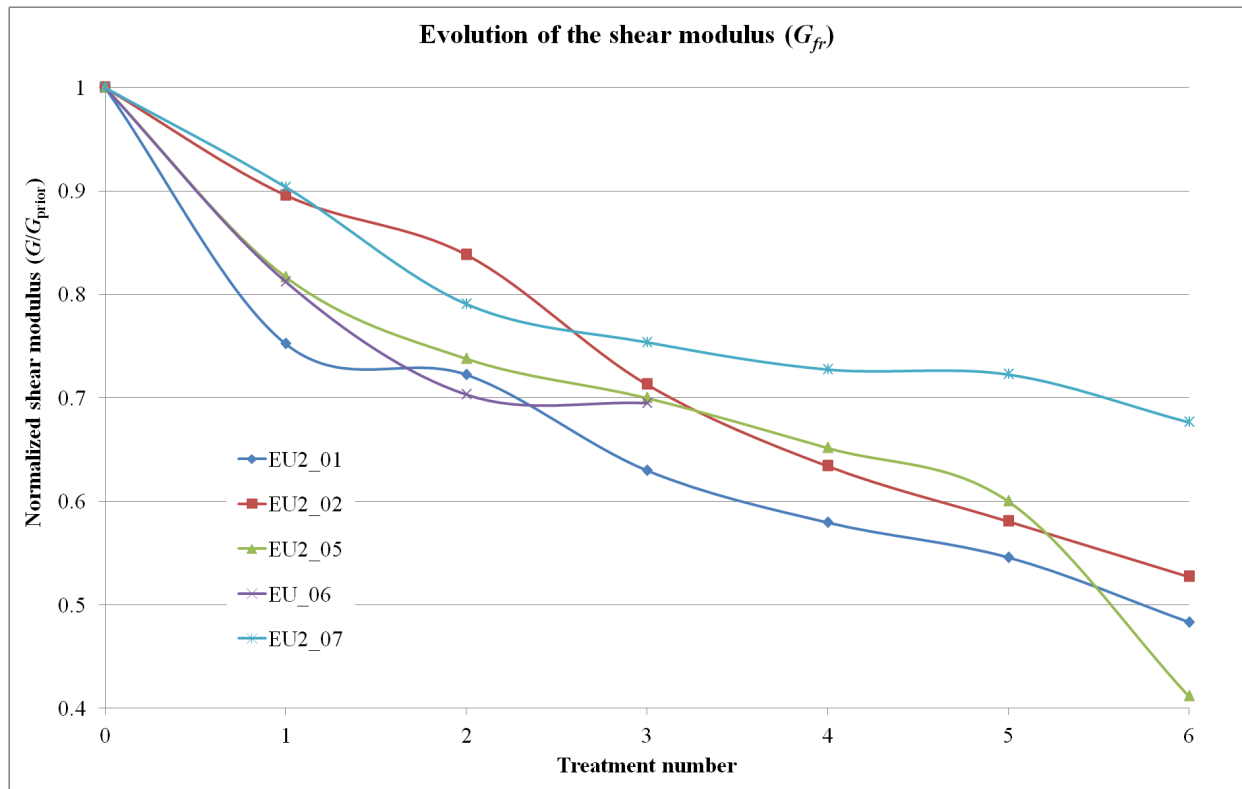
Figure 44: Evolution of the shear modulus as a function of treatment number. A significant reduction in the shear modulus is seen for all the samples due to the acid treatment. The trend is somewhat diminishing.

Regardless of the chosen loading process, they all show similar behavior and significant changes. Table 20 to Table 23 contains the initial and final moduli for each experiment based on the average of the unlading/reloading, including the change in percentage.

Table 20: Initial and final Young's modulus (E_{fr}) for the different test samples, including the change in percent with respect to after final treatment.

Sample ID	Young's modulus (E_{fr}) [GPa]		
	Initial	Final	Change
EU_06	18.8 ± 1.9	14.0 ± 1.4	26 %
EU2_01	25.6 ± 2.6	13.2 ± 1.3	48 %
EU2_02	24.9 ± 2.5	13.9 ± 1.4	44 %
EU2_05	18.9 ± 1.9	8.8 ± 0.9	54 %
EU2_07	18.3 ± 1.8	14.1 ± 1.4	23 %

Table 21: Initial and final Poisson's ratio (v_{fr}) for the different test samples, including the change in percent with respect to after final treatment.

Sample ID	Poisson's ratio (v_{fr})		
	Initial	Final	Change
EU_06	0.15 ± 0.02	0.23 ± 0.02	54 %
EU2_01	0.20 ± 0.02	0.28 ± 0.03	40 %
EU2_02	0.21 ± 0.02	0.29 ± 0.03	38 %
EU2_05	0.17 ± 0.02	0.32 ± 0.03	88 %
EU2_07	0.11 ± 0.01	0.26 ± 0.03	137 %

Table 22: Initial and final bulk modulus (K_{fr}) for the different test samples, including the change in percent with respect to after final treatment.

Sample ID	Bulk modulus (K_{fr}) [GPa]		
	Initial	Final	Change
EU_06	9.1 ± 0.9	8.6 ± 0.9	5 %
EU2_01	14.5 ± 0.1	10.2 ± 1.0	30 %
EU2_02	14.5 ± 0.1	11.4 ± 1.3	21 %
EU2_05	9.9 ± 0.1	8.2 ± 0.8	17 %
EU2_07	7.8 ± 0.8	9.82 ± 1.0	26 %

Table 23: Initial and final Shear modulus (G_{fr}) for the different test samples, including the change in percent with respect to after final treatment.

Sample ID	Shear modulus (G_{fr}) [GPa]		
	Initial	Final	Change
EU_06	8.19 ± 0.8	5.7 ± 0.6	30 %
EU2_01	10.7 ± 1.1	5.2 ± 0.5	52 %
EU2_02	10.3 ± 1.0	5.4 ± 0.5	47 %
EU2_05	8.1 ± 0.8	3.3 ± 0.3	59 %
EU2_07	8.2 ± 0.8	5.6 ± 0.6	32 %

The average change for the Young's modulus after 6 treatments is 9.4 ± 3.6 GPa, whereas for the Poisson's ratio, the bulk modulus and the shear modulus are 0.12 ± 0.04, 1.8 ± 2.7 GPa and 4.5 ± 1.2 GPa, respectively. The change in Young's modulus is not directly proportional to the number of treatments, suggesting a diminishing effect. The change going from 3 to 6 RAT increases more significantly for the bulk modulus, while for the shear modulus, the change is more random. No final conclusion on the relation between number of treatments and change can be made due to only having one 3 RAT sample. In addition, the pronounced channeling seen in the 3 RAT sample could give reason for discarding the sample. As mentioned in Chapter 5, the stiffness moduli are sensitive to small heterogeneities within the rock, thus having that the 3 RAT sample is from another batch enhances the uncertainty in correlating the 3 RAT evolution and the 6 RAT evolutions.

The Poisson's ratio is estimated from a uniaxial unloading/reloading. Having that the Poisson's ratio is increasing indicates that the deformation in radial direction increases compared to the axial deformation.

Softening of the rock is justified by assessing the evolution of the axial and radial strain paths. Figure 45 shows the strain paths for EU2_01, all the other experiments have similar paths. It is clear from the overall evolution for the strain (purple lines), that there is deformation despite keeping *in situ* stress conditions constants. This implies that the rock becomes softer, justifying the observations done based on the measured values.
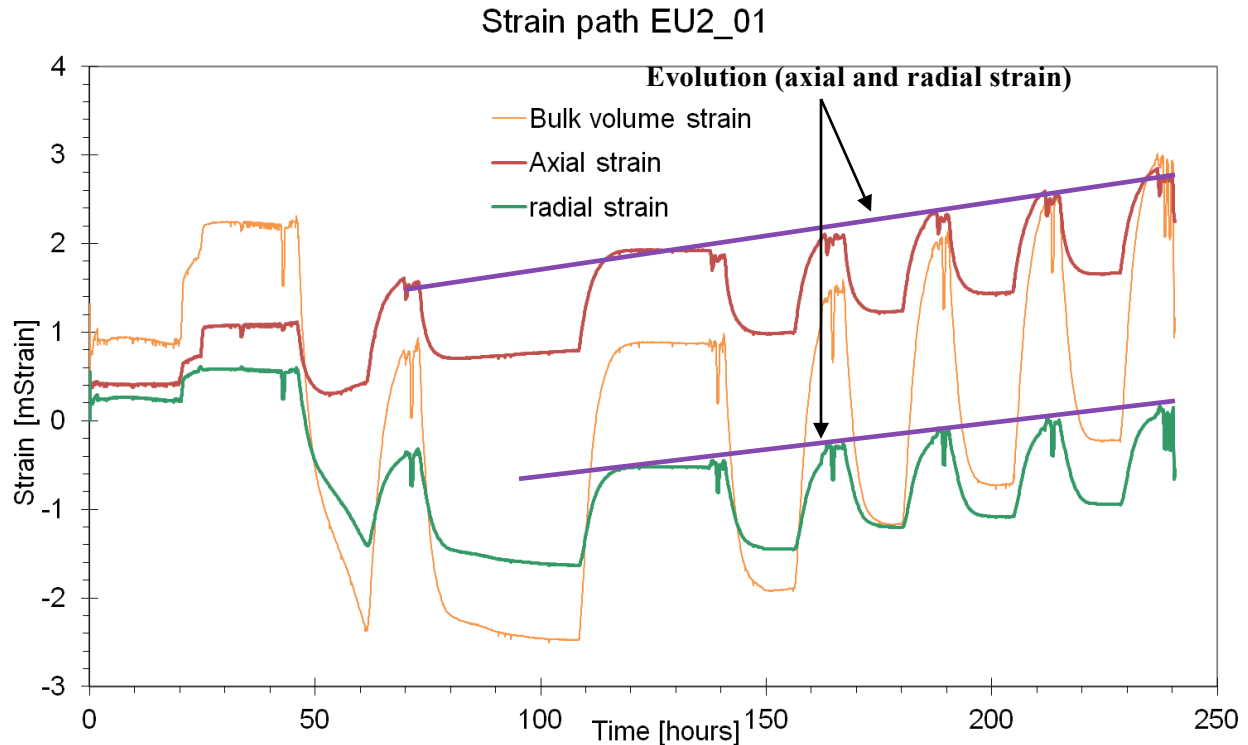
Figure 45: Strain paths EU2_01. Trend lines (purple lines) for the axial and radial strain path show deformation with respect to time, indicating a softening of the rock due to acid treatments.

8.7.2 Stiffness – porosity trends

As presented in Chapter 3, trend lines of the stiffness moduli with respect to porosity can be estimated. IFP [38] presents in their paper plots of the bulk and shear moduli for various carbonates obtain from the literature together with their own experimental data. The plots also include trend lines, estimated from equation (15) and (16), and the *Hashin and Shtrikman's bounds*. The grain moduli that are required in the trend line equations are obtain from the literature in these plots. Figure 46 show the bulk modulus plot from this paper including the results from EU2_01. It is clear that the bulk modulus in IFP's case show a significant decrease because of acid treatments. It is also noteworthy that the decrease does not follow the trend line, indicating that the acid treatment has a chemical effect on the stiffness, and not only causing a reduction in stiffness by increasing the porosity. Since the trend line is dependent of the grain modulus, mismatch between our untreated data point and the line is expected. Despite the mismatch, it is evident that our data does not follow the trend line either.
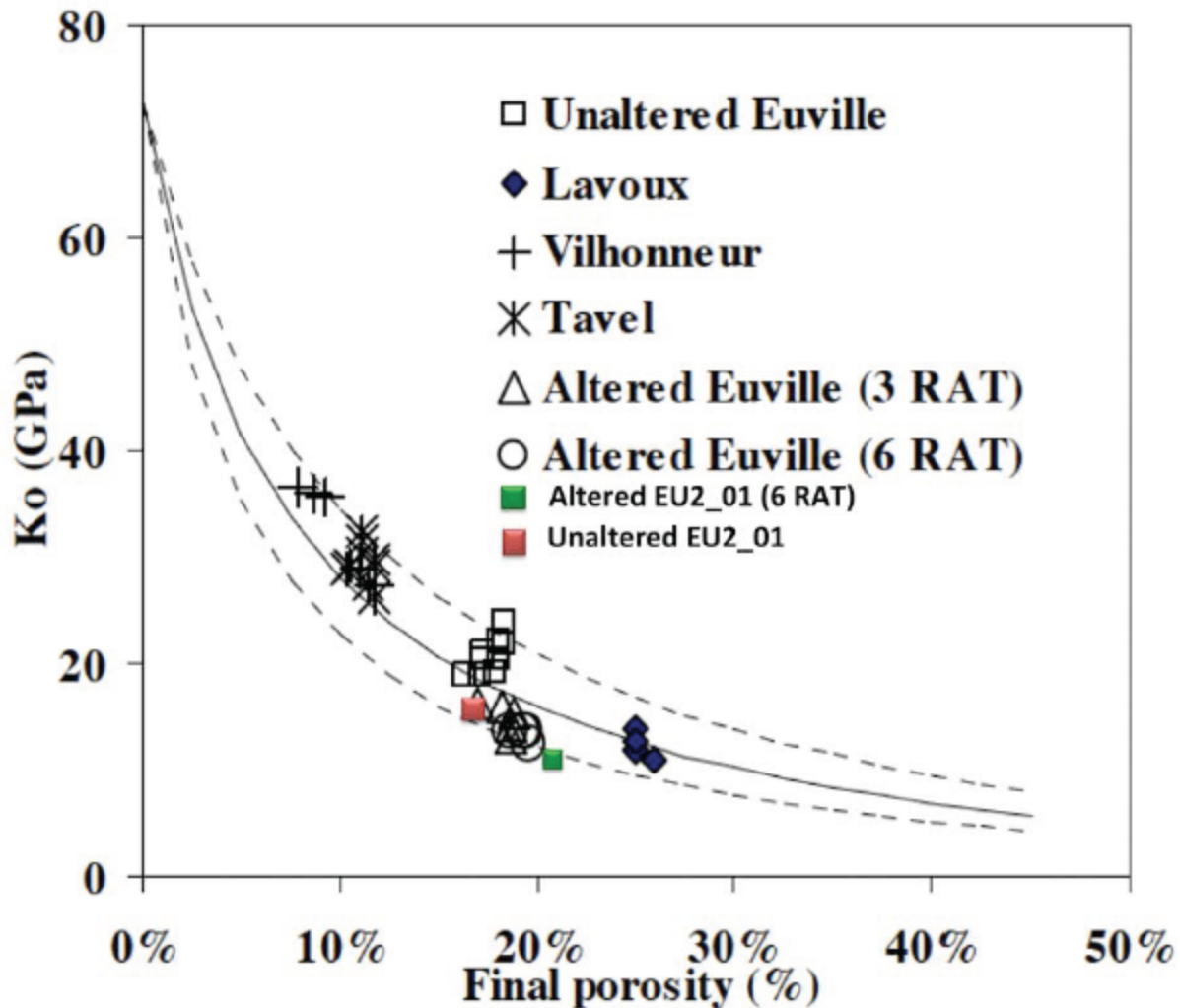
Figure 46: Bulk modulus plot from IFP's research including literature data, Euville experimental data and the results from EU2_01 from the current project.

To get a more valid assessment of the deviation from the trend line for the current project, we need to fit the trend line to our untreated sample. In the following discussion, EU2_01 is taken into consideration.

Equation (15) and (16) are used to generate the trend lines. In order to make a fit with the untreated data point, we use the grain modulus that was obtained during initial loading for EU2_01, $K_s = 57.5$ GPa, and adjusting the K_c/K_s ratio until a perfect match is obtained. Figure 47 shows the trend line, including the *Hashin and Shtrikman's* bounds estimated for the current project. Since we have drained conditions, K_f is set to 0 GPa when estimating the bounds, whereas for the model, a K_c/K_s ratio of 0.07 is chosen. It is evident that there is a significant deviation from the trend line after treatment. The results are in line with what IFP has found, justifying that there could be additional effects on the stiffness change such as micro pore effects.
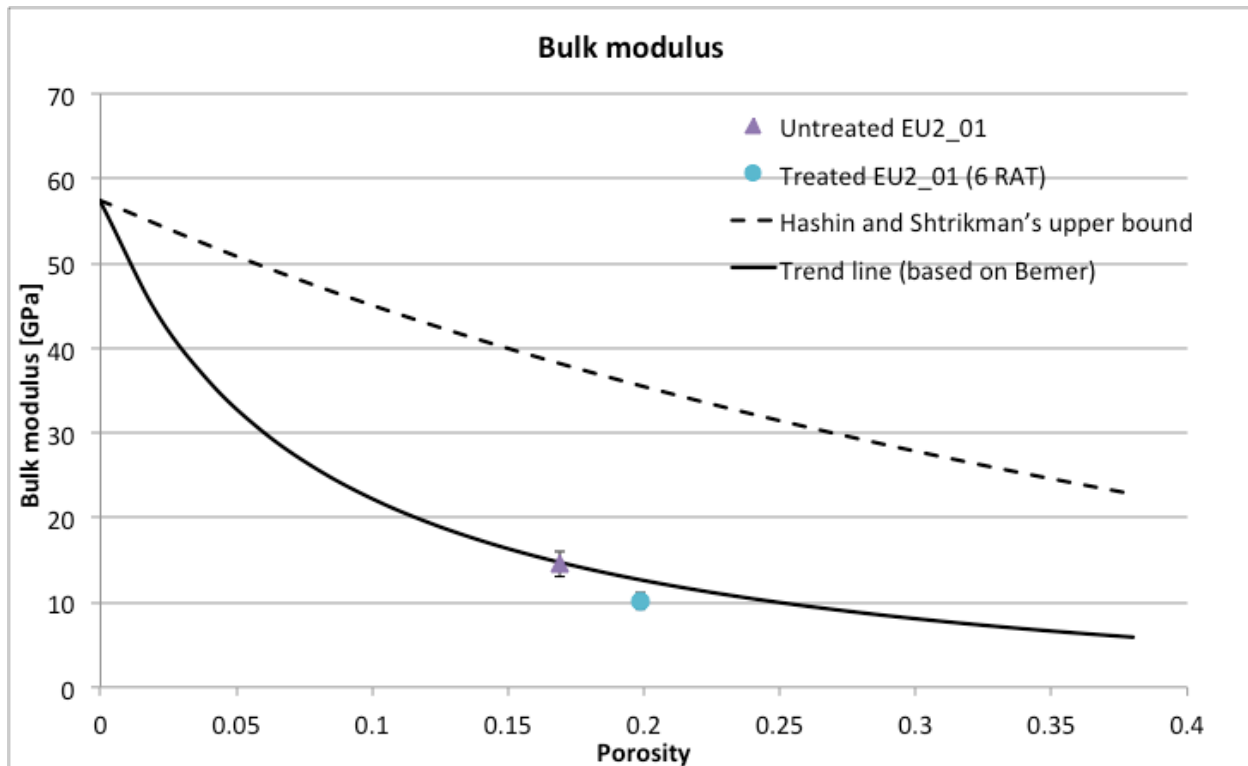
Figure 47: Bulk modulus data from EU2_01 compared to the trend line of the bulk modulus with respect to porosity. There is a clear deviation from the trend line after treatment. Considering the errors does not influence the result of any significance.

By assuming an increase in porosity for the failed samples corresponding to the same amount as seen for EU2_01 and estimating the trend lines, we see similar deviations after treatment for those samples as well. We have chosen here to not include them because of practical reasons related to the difference in absolute values. It also applies for the other experiments that an error of $\pm 10\%$ does not affect the conclusion of the trends.

The Young's modulus trend line can be derived, by combing the trend line equation from the bulk modulus and the shear modulus. The Young's modulus is presented in Figure 48, in which a $G_s = 29$ GPa and $G_c / G_s = 0.12$ is chosen. G_s is found in the literature, and Bemer [27] showed that the chosen ratio, G_c / G_s, is reasonable to assume. The bulk modulus show clear evidence of deviation from the trend line, suggesting other effects influencing the reduction in stiffness. The Young's modulus shows even stronger deviation from the trend. The diminishing decrease in the stiffness moduli, discussed earlier, could potentially indicate that the additional effects become less as the rock is continued being exposed to the acid.
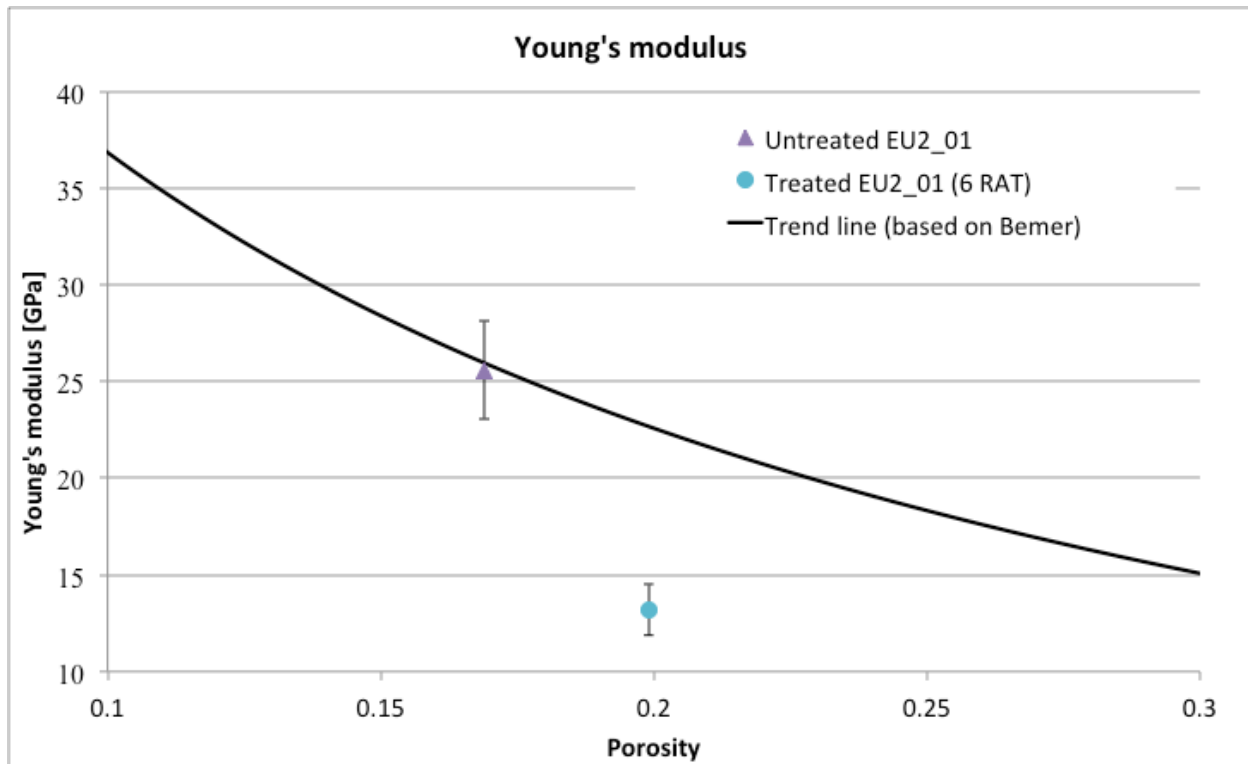
Figure 48: The Young's modulus trend line is calculated based on the bulk and shear moduli trend lines. Measured Young's modulus data from EU2_01 compared to the trend line. There is a clear deviation from the trend line after treatment suggesting chemical effects.

As was discussed earlier in the chapter, inlet and outlet effects are present, where the inlet is much more leached than the rest. This could potentially affect the result significantly, because the rock is not stiffer than its softest point. One possibility is therefore that the strong reduction in stiffness is only representing the inlet. However, as will be discussed later in the acoustic velocity section, dynamic moduli behave the same way. These are based on measurements dependent on the whole core, not the weakest or softest points.

In conclusion, there is clear indication of that acid treatment reduces the stiffness significantly. Higher degree of acid exposure results in more softening, though with a diminishing trend. Fracturing, forming secondary porosity, during the treatments could cause the rock to become softer than the expected porosity trend. The applied models are also based on having natural evolution of the rock's porosity, as evolves during diagenesis (cementing, plastic deformation). Altering the porosity significantly faster could cause a different micro-structure to evolve, suggesting that the additional effects causing, enhanced softening of the rock, are on a micro-pore scale, e.g. alteration of the grain surface. In order to study these effects, more advance imaging techniques are required, such as SEM analysis. The above results should be considered carefully due to few data points. Some degree of scatter should also be expected if the results are tried reproduced. For a more detailed analysis and assessment of the consequences that the acid treatment has, additional experiments and studies are required.

Our results are in line with the trends that IFP also observed in their research, supporting the current project's findings. The reduction in stiffness gives reason to believe that also the

strength is reduced due to acid-rock interaction. This is addressed in more detail in the next section.

8.8   Strength alteration

Since the aim is to investigate whether the strength is affected by the alteration, a reference to the unaltered rock had to be established. Three failure tests according to Table 5 were performed to determine the failure envelope for untreated Euville. Figure 49 shows the plotted data, and the trend line, which makes up the Mohr-Coulomb failure line. As mentioned earlier, the error is assumed $\pm 10\%$.

While the two lowest confining pressures resulted in brittle failure, the 10 MPa confining pressure case ended in a ductile failure. By applying equation (37) and (38), the cohesion (S_o) and the friction angle (ϕ) can be determined. Further on, uniaxial compressive strength (C_o) and failure angle (β) can be determined from equation (32) and (33). The results are listed in Table 24.
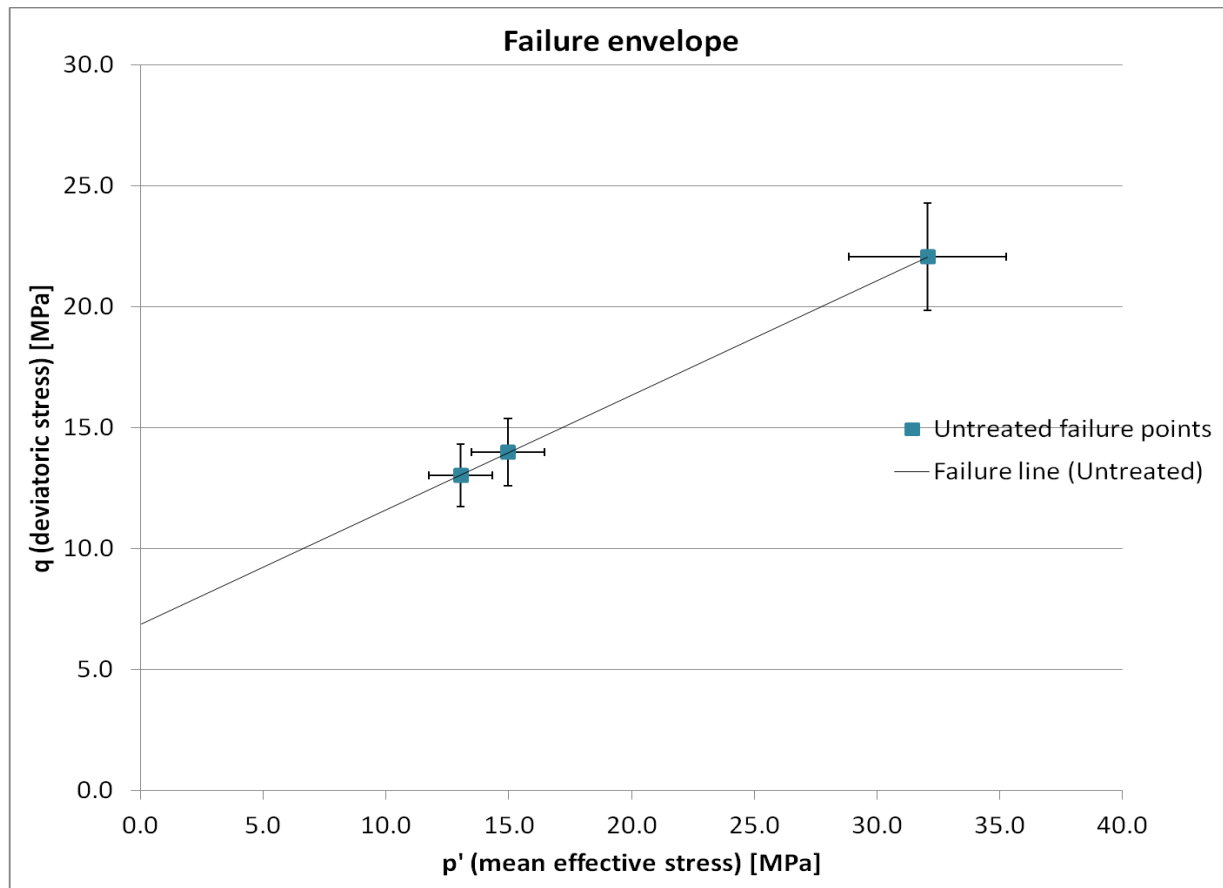
Figure 49: Failure points for the untreated Euville samples. The line represents the failure line for untreated Euville valid for the current experiment.

The failure envelope for treated Euville is determined from the three failure experiments done on samples subjected to 6 RAT. All three experiments were performed at different confining pressures, according to Table 5. Similar to the untreated samples, the two lowest confining pressures resulted in a brittle failure. On the contrary to the untreated 10 MPa sample,

the treated 10 MPa confining pressure case ended in a brittle failure. Here, we already see indication of that something has changed with respect to the strength properties of the rock. The stress path for EU2_02, at the point of failure, is presented in Figure 50, clearly showing the brittle failure.
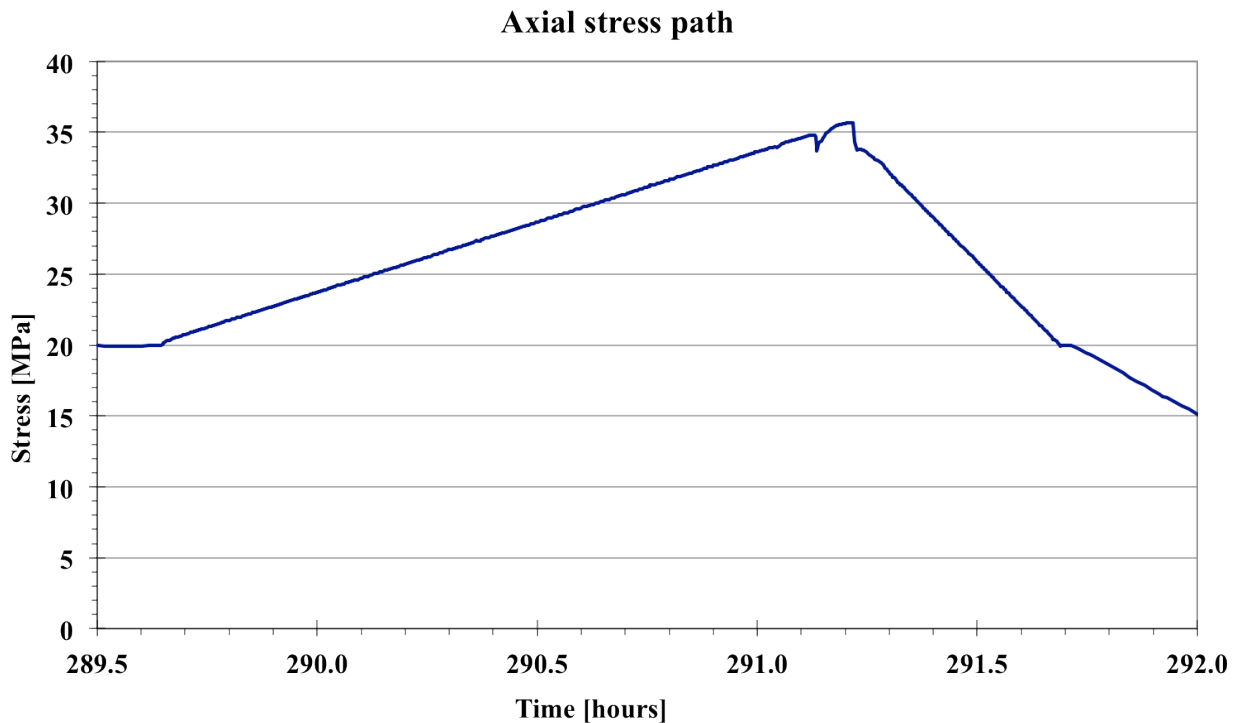
Axial stress path

Figure 50: Axial stress path for EU2_02 at the time of failure. The sharp drop in axial loading indicates a brittle failure.

8.8.1 Mohr – Coulomb for treated Euville

Based on the evolution of the stiffness, and the increase we see in porosity due to the acid treatment, the results from the strength tests are not that unexpected. The failure points for the treated samples are plotted in q - p' space in Figure 51, together with the failure line for the untreated sample. The failure points fall below the failure line, suggesting that the rock is weakened due to the acid treatment. The new Mohr-Coulomb failure line can be determined by drawing a trend line through the failure points (represented as the dashed line in Figure 51), whereas the corresponding parameters are listed in Table 24. It is evident that there is a change in the failure envelope, both in terms of slope and interception with the ordinate axis, implying a change in cohesion and friction angle, which can also be seen in Table 24.
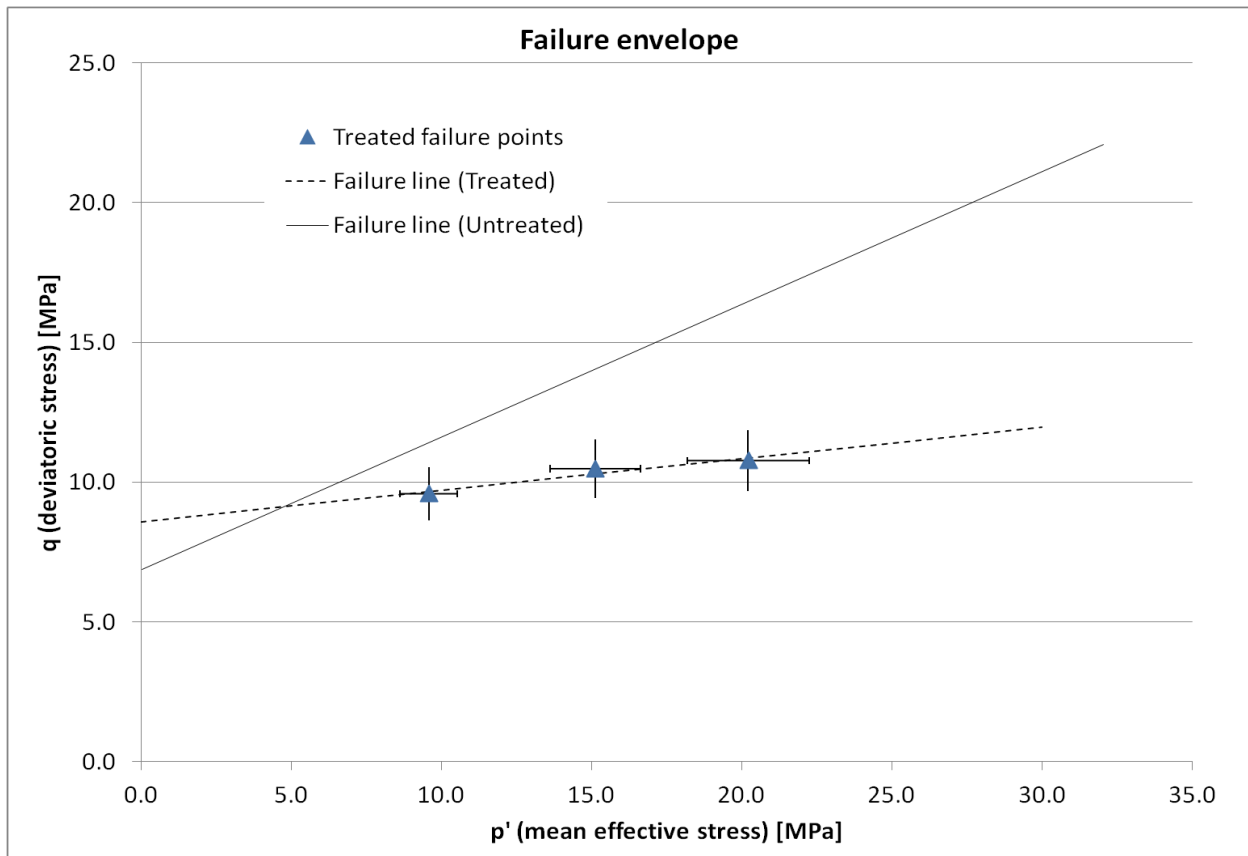
Figure 51: Failure points for the treated samples. Falling below the untreated failure line indicates that the strength is reduced. The dashed line represents the new failure line. Friction angle is clearly reduced, while the cohesion is slightly higher.

Table 24: Strength parameters and Mohr – Coulomb parameters for both untreated and treated (6 RAT) Euville.

Parameter	Untreated Euville	Treated Euville (6 RAT)	Change *[%]*
Cohesion (S_o)[MPa]	7.8 ± 0.8	8.7 ± 0.7	11 %
Friction angle (ϕ) *[deg]*	28.3 ± 2.8	6.5 ± 0.9	77 %
Uniaxial compressive strength (C_o) *[MPa]*	26.1 ± 2.6	19.4 ± 1.9	26 %
Failure angle (β) *[deg]*	59.1 ± 5.9	48.2 ± 4.8	18 %

The new failure Mohr-Coulomb parameters show a clear weakening of the rock. The friction angle is significantly reduced, whereas the cohesion is slightly increased. This increase is well within the error margin and it is therefore likely that the change in cohesion is only cause by scattering, being more or less unchanged. The internal friction angle is a measure on the ability to withstand shear stress. A reduction of 77% in the friction angle is therefore a significant weakening of the rock in terms of withstanding shear forces. Uniaxial compressive strength, the axial loading force that the rock can withstand having zero confining pressure, is also decreased by 35%.

The errors of ±10% in Figure 51 indicate that there is a lot of scattering in the data leading to uncertainties. Despite taking the errors into account, which reduces the change to

some extent, is not enough to justify unaltered rock strength. In general, increasing porosity should result in weakening. Strength, stiffness and porosity are normally related. Having a reduction in stiffness is therefore another indication of weakening, thus one can assume that the above results are reasonable. The current method of assessing the rock strength does not indicate whether other effects are influencing the rock strength. This requires a different approach.

Our results are consistent with IFP observations. However, they assess the results in a different way, which allows them to make assumption in terms of whether there are other effects, which could be of a chemical nature, on the strength. Their conclusion is that the strength is only affected by the porosity increase alone. The consistency in stiffness results between the current project and IFP's work give reason to believe that our strength is following IFP's findings, implying that weakening in our case is also unaffected by a potential chemical aspect and only caused by the increase in porosity.

The main uncertainty for the strength measurements is the differing elastic moduli. EU2_05 and EU2_07 had an initial Young's modulus of 7 GPa less than EU2_02, suggesting a much softer rocks. Also, other heterogeneities in the rock and differences between the samples are all resulting in uncertainties that could affect the result. The uncertainties cause a lot of scattering, making it difficult to draw final conclusions. This applies for both the untreated and treated measurements. Despite the uncertainties, the results are valid in an assessment on whether there are indications of altered strength due to the acid treatment or not.

8.9   Acoustic velocities

From the definitions of the P- and S-waves in Chapter 3, softening should result in a decrease in the velocities. With the exception of the 3 RAT experiment, velocities have been continuously measured throughout the experiments. We are then able to monitor the change in velocities with respect to the treatment number. Figure 52 and Figure 53 show the evolution of the P-wave and S-wave velocities throughout the experiments. Note that in the current project, the absolute values are of less interest.

The acoustic velocities are estimated based on measured arrival times. This introduces the uncertainty of picking the correct first arrival for the respective wave type. The first arrival for the P-waves is not that difficult to determine. It is evident that the velocities are decreasing as a consequence of the acid treatments. The consistency in the trends for the P-waves could indicate that all samples follow the same porosity evolution as well.

Determining the S-wave velocities is significantly more difficult. Some S-waves are converted into P-waves, which arrive before the first S-wave. This creates a lot of noise around the point of arrival for the S-waves and hence, more uncertainties in the estimated S-wave velocities. The latter explains some of the dispersion seen in Figure 53. Despite some artifacts, it is evident that also the S-waves are affected by the alteration.

The reduction in stiffness, strength and bulk density are all directly caused by the increase in porosity, hence the increase in porosity is also causing the velocity changes. From the definition of the P-wave velocity (equation (39)), we see that it depends on the bulk modulus, the shear modulus, and the bulk density. These are all porosity dependent, having that an increase in porosity, decreases the values. Intuitively, this implies that the velocities are also decreasing with increasing porosities. Whether additional effects such as secondary porosity, or alteration on a micro-pore scale has an impact or not, requires the measured velocities to be assessed with respect to velocity-porosity models. This is addressed shortly.
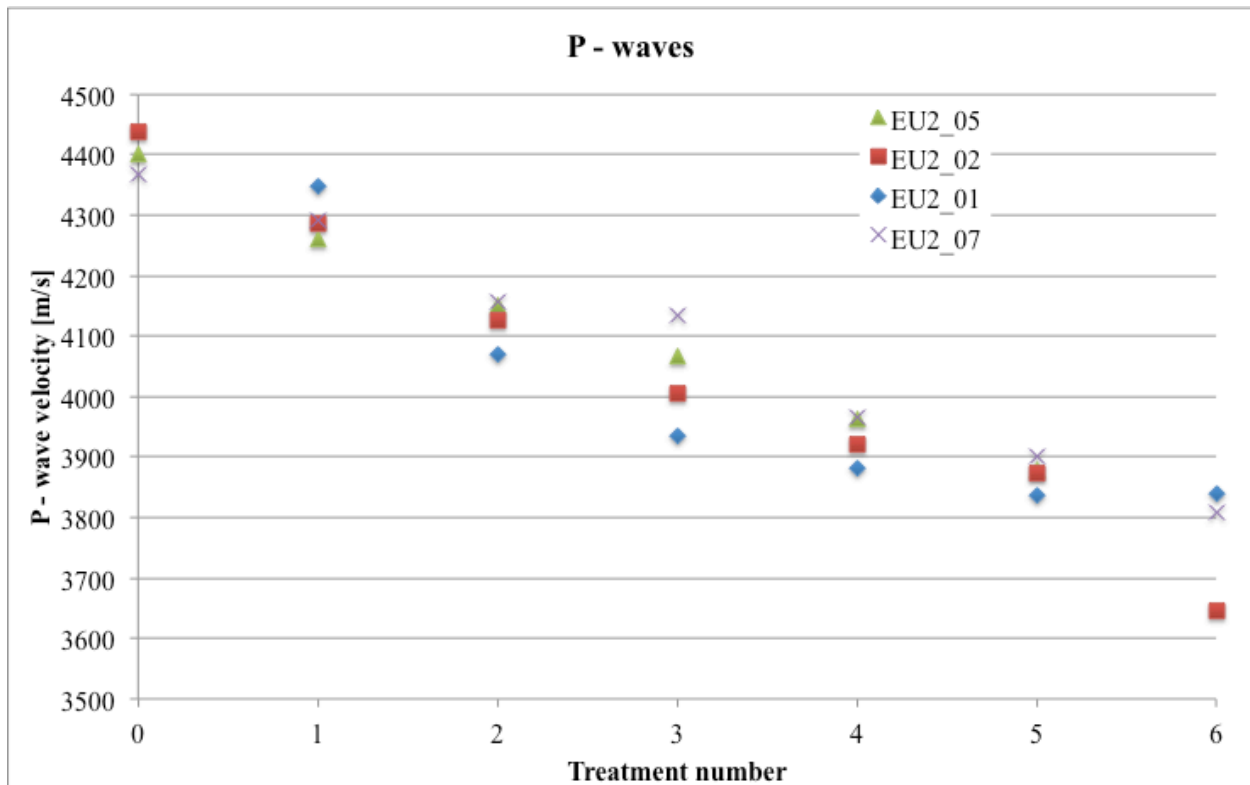
Figure 52: Evolution of the P-wave velocities with respect to treatment number. P-wave velocities are clearly reduced as the rock is treated. The consistency in the trend lines between the samples could indicate that they follow the same porosity evolution trend.
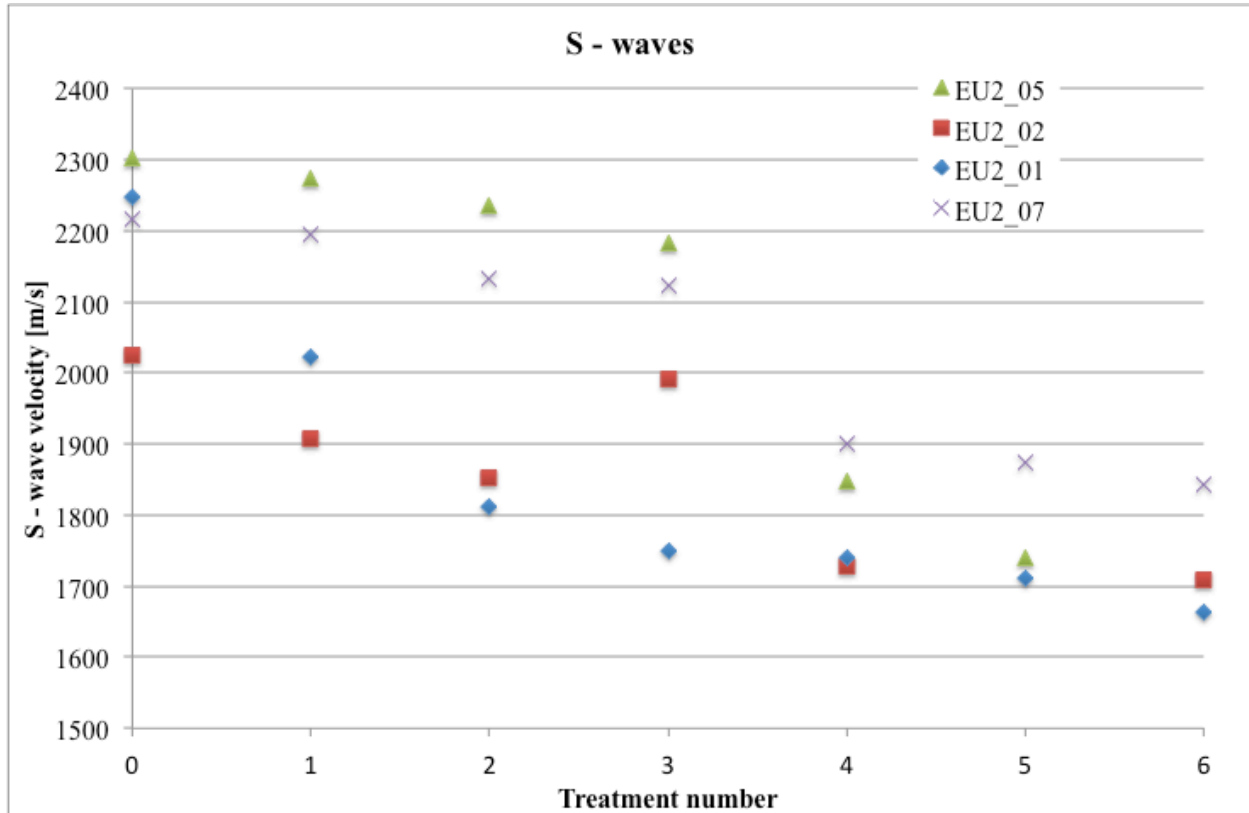
Figure 53: S-wave velocities with respect to treatment number. Despite the dispersion, S-wave velocities are decreasing as a consequence of the acid treatment. The dispersion is most likely explained by the difficulty in estimating correct S-wave velocities because of noise.

8.9.1 Velocity trends with respect to porosity: Wyllie's time average model

Velocities in rocks are sensitive to a number of parameters. It is therefore difficult to find a correct correlation between velocities and porosity. Secondary porosity (vugs, cracks) tends to be stiffer than primary porosity, hence lower the velocity less than what the same primary porosity would have done. It seems that the velocities are more related to the density rather than the porosity [28]. The limestone outcrop material used in the current project (Euville) has a more or less uniform mineralogy. Secondary porosity is of less significance. The criteria for Wyllie's time average equation, equation (49), are more or less fulfilled, and it is therefore reasonable to assume that it can be applied.

Figure 54 shows the trend line for the P-wave velocity with respect to porosity, based on Wyllie's equation, where we have assumed a fluid velocity of $V_{p-fl} = 1500\ m/s$ and a grain velocity of $V_{p-grain} = 6600\ m/s$. Due to the inability to measure final porosity for the failed samples, it is also assumed that the increase in porosity is equal to measured porosity increase for EU2_01, being 3 PU for 6 RAT. According to the consistency in the P-wave velocity evolutions, this assumption is reasonable. Also, because of technical issues during the last treatment of EU2_05, measured velocity after the 6th treatment is unavailable. Final porosity for EU2_05 is corrected accordingly. An error of $\pm 5\%$ has been taken into account and is shown by the error bars, both for the measured velocities and the final porosity.
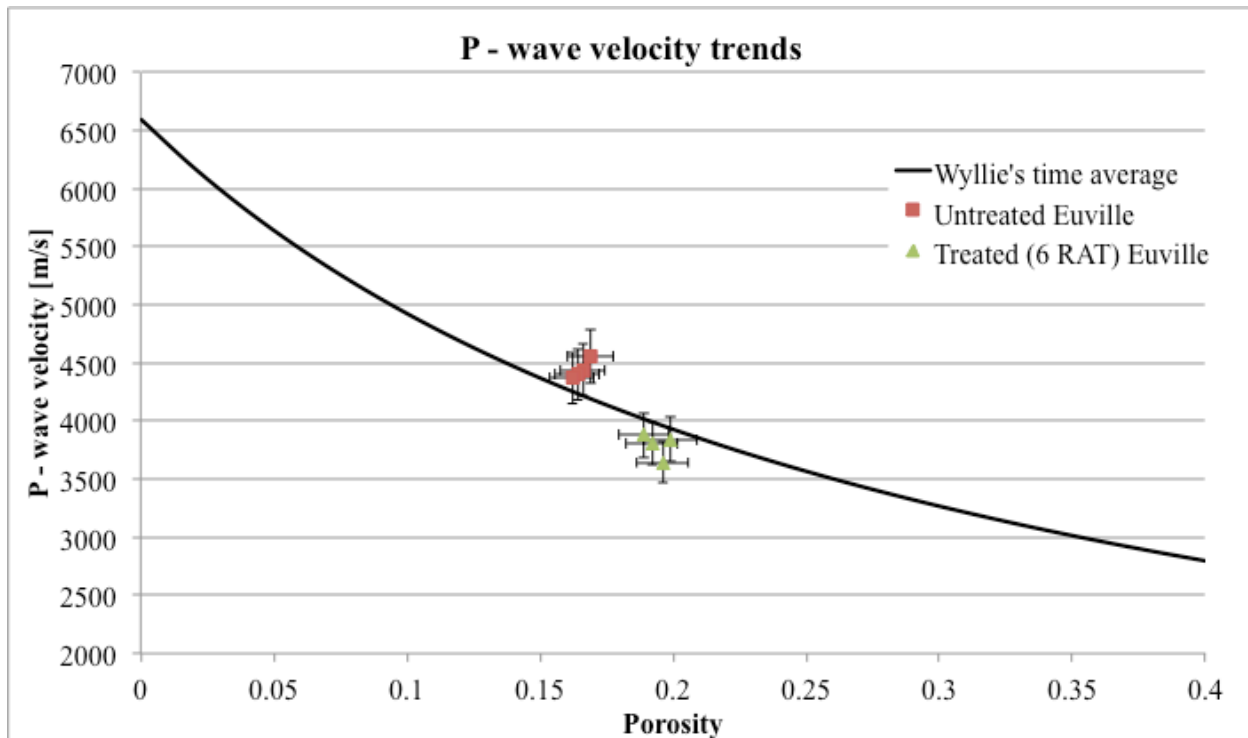
Figure 54: Measured P-wave velocity data for untreated and treated Euville compared to Wyllie's time average. Despite having a mismatch with the untreated data, deviation from the estimated velocity-porosity trend is clear. Additional effects, other than the porosity increase, could be the cause.

From the above figure, we see indications of that the trend line between the untreated and treated data points deviates from the estimated porosity trend. A better fit is achievable by adjusting within the error range. However, this requires a maximum optimization, which is not very likely. The deviation from the trend could be cause by the same effects as was highlighted in the stiffness section, Section 8.7. Considering that there were indications of other effects on the stiffness and that velocities are dependent of the rock's stiffness, implies that these effects could be reflected on the velocities as well. However, as mention in Chapter 3, one should be careful drawing final conclusions based on Wyllie's time average equation because of the limited application and many uncertainties. This also applies with respect to the uncertainties related to the measure velocities.

8.9.2 Velocity trends with respect to porosity: Biot's theory

In Chapter 3, Biot's theory of elastic wave propagation was presented. This approach is most accurate for low frequencies. The current experiment uses 800 kHz, which is considered to be an intermediate frequency. Despite being slightly too high, assessing the measured date with respect to Biot's theory could be useful.

Two models can be derived using equation (50) and (51), one based on the critical porosity model, equation (18) and (19), and one by applying the Bemer [27] model for drained moduli, equation (15) and (16). Both approaches calculate the drained moduli, which are then used in the Gassmann equation, equation (46), to obtain the saturated or undrained moduli. From there, Biot's equation is applied to derive the trend lines. The models are fitted such that the untreated values match the trend lines. Since the models are somewhat different, different values for the parameters are used. For the critical porosity approach the following values are used:

K_s = 50 GPa, G_s = 20 GPa and φ_c = 0.4. For the Bemer approach: K_s = 68 GPa, K_c/K_s = 0.12, G_s = 30 GPa and G_c / G_s = 0.12. Figure 55 show the plotted trend lines for both the critical porosity approach and the Bemer approach. The measured velocities before and after treatment are also plotted. Again, we have assumed an equal porosity change for the 6 RAT failed samples as was measured for EU2_01.
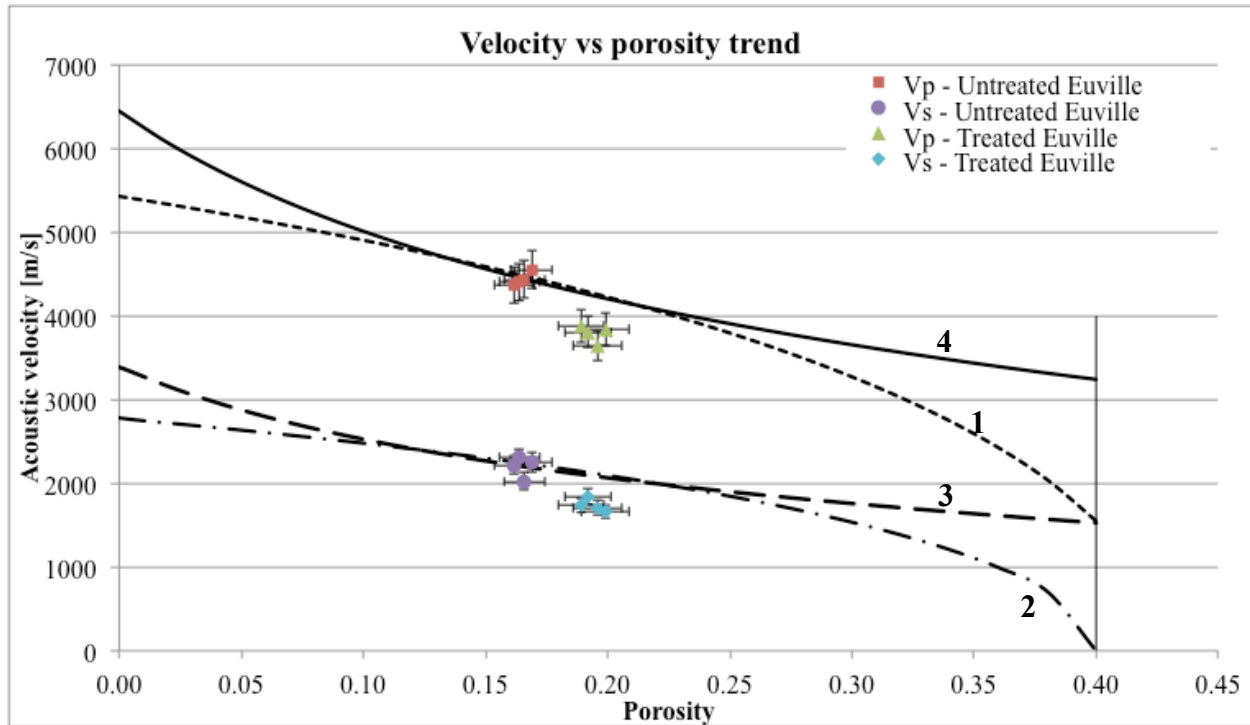
Figure 55: Measured P- and S-wave velocities for untreated and treated Euville compared to Biot's porosity model based on both critical porosity model (line 1 and 2), and the Bemer model (line 3 and 4). Although the two models predict different velocity evolutions with respect to porosity, it is evident that there is a deviation from the trend line between data points and the porosity model. The vertical line represents the critical porosity limit.

Even though the chosen parameters are differing form the literature and between the models, the intension is to show whether there is a deviation from the trend line for the treated samples. We see a good fit for the untreated data with both approaches, however the predicted trend lines are differing from one another. Despite the different model behavior, it is evident that the treated data deviates from the porosity trends, which is consistent with what Wyllie's Time Average also predicted. This applies to both P–waves and S–waves, suggesting the presence of additional effects on the acoustic properties, such as secondary porosity and micro pore alteration. The rapid change in porosity, induced in the current experiments, compared to natural diagenesis (plastic deformation and cementing), could cause a different microstructure to evolve, thus resulting in a somewhat different velocity-porosity trend.

These models should be assessed form a very critical point of view due to the applied frequency in the current experiments. It is not completely in the valid range for the model. For further applications, the models should be verified by velocity measurements for a diverse porosity range of untreated samples. One should also be very critical with respect to the chosen parameter values used for estimating the trend lines.

8.10 Dynamic moduli

The velocities are often used to estimate the dynamic rock moduli. As described in the Chapter 3, these are not equal to the static properties that are obtained during stress cycles. Table 25 shows the pre and post dynamic and static Young's moduli and P-wave moduli for all the treatment experiments. The dynamic moduli are calculated based on equation (42) to (45), whereas the static P-wave modulus is calculated from the last part of equation (45) using static moduli. We will later see that the static and dynamic Young's moduli are more or less equal, which is also the case for the shear moduli. The latter is a rather interesting finding. However, for the time being, we are not able to understand why this is. The P-wave moduli are differing significantly, being close to a factor of 2 higher for the dynamic case. This also applies for the Poisson's ratio and the bulk moduli. EU2_05 and EU2_07 differ from the other samples by having a much higher dynamic Young's modulus than the static one. Having that the dynamic Young's moduli are similar for all the samples, while the static is significantly lower for EU2_05 and EU2_07 could indicate that the static estimates are less good, or that there are soft spots in the samples, causing the lower static moduli. The velocities are less affected by such soft spots, whereas static stiffness measurements are sensitive to these resulting in lower values than the sample average.

The big uncertainty in the determination of first arrival for the S-waves implies an uncertainty in the S-wave velocities. Dynamic moduli estimated based on both P- and S-wave velocities are therefore less accurate than the P-wave modulus, which only depends on the P-wave velocity. The P-wave modulus is therefore considered to be a more reliable modulus to assess in terms of moduli and velocity evolutions. However, one should not disclaim the other moduli with respect to the rock alteration assessment.

Table 25: Pre and post experiment static and dynamic Young's and P-wave moduli.

Sample	E_{fr} [GPa]				H_{fr} [GPa]			
	Pre		Post		Pre		Post	
	Static	Dynamic	Static	Dynamic	Static	Dynamic	Static	Dynamic
EU2_01	25.6	29.9	14.0	16.1	24.6	45.8	16.3	31.1
EU2_02	24.9	24.9	13.2	16.7	25.8	43.5	15.5	28.1
EU2_05*	18.9	31.3	14.2	18.7	15.9	43.3	12.2	33.8
EU2_07	18.3	29.0	14.6	20.3	14.0	42.5	14.0	32.3

Because of technical problems, acoustic measurements were not done after the 6th treatment for EU2_05. The results presented in this table are all after the 5th treatment for this particular experiment.

The difference between dynamic and static moduli is expected. Experience shows that the difference can be close to a factor of 2. However, the results from the evolution of the dynamic moduli are very important in terms of justifying the evolution seen for the static moduli. Figure 56 shows both the dynamic and static Young's moduli with respect to treatment number for EU2_01, while Figure 57 show the P–wave moduli. Similar plots can be seen for the bulk and shear moduli in Figure 58. As before, due to the uncertainty in the final porosity for the failed samples, only the built out sample EU2_01 is assessed and presented. The trend, however, is the same for all the samples. Assuming an error of approximately ±5% does not change the estimated values and the trends of any significance. Common for all the moduli is that the decreasing trend is diminishing.
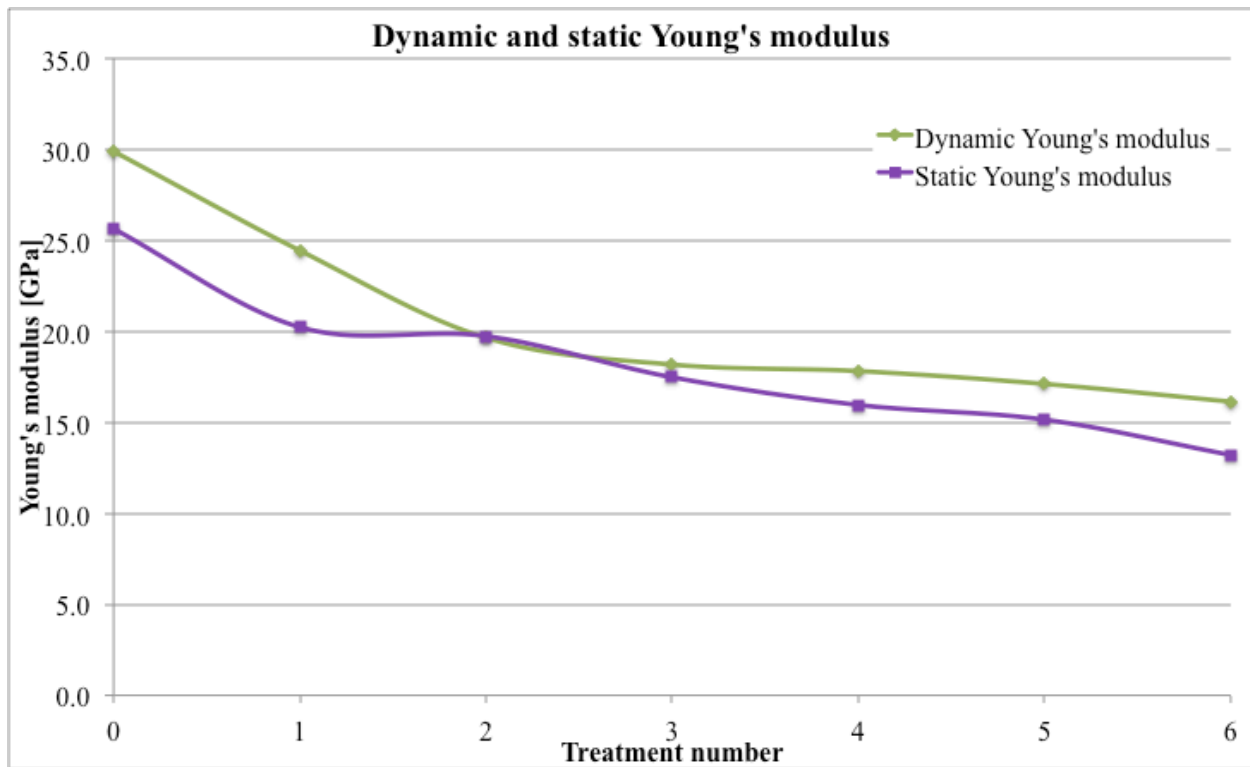
Figure 56: Dynamic and static Young`s modulus for EU2_01. Both the static and dynamic values are more or less equal and show the same trends. Having that two independent methods of estimating the stiffness show similar trend, justifies the observations.
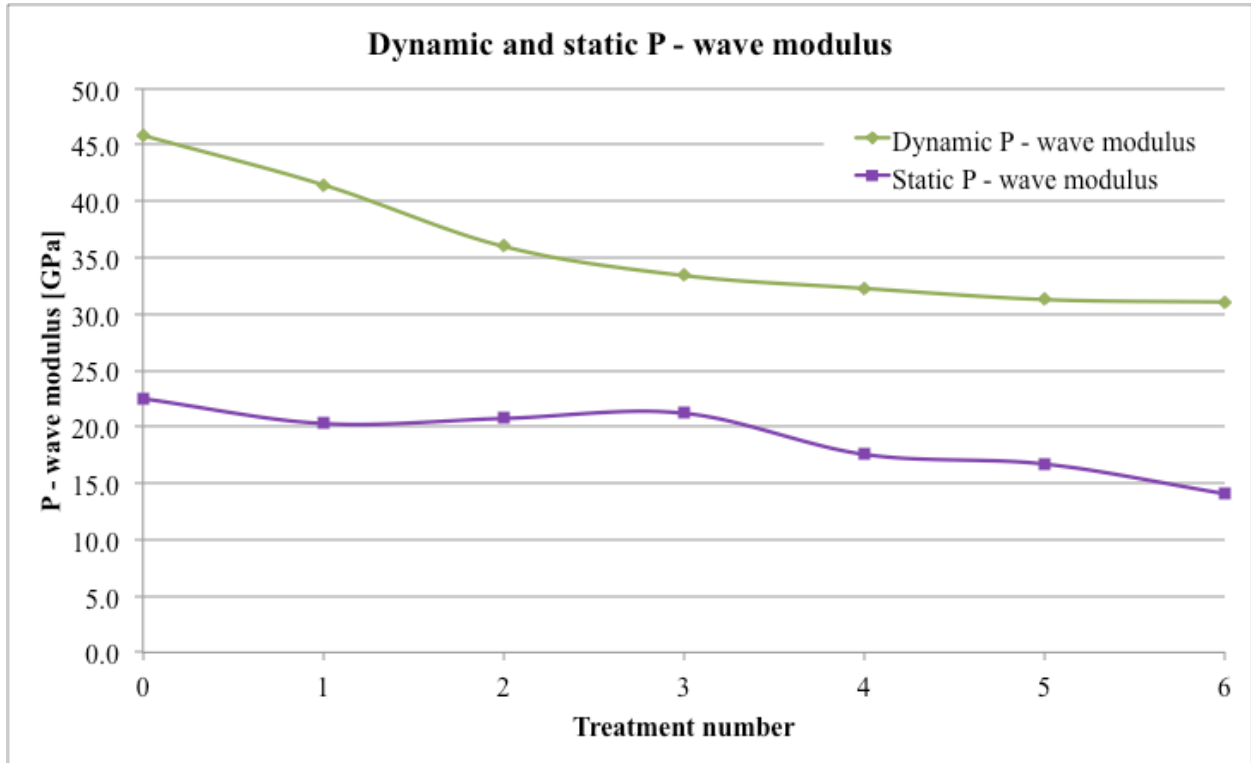
Figure 57: Dynamic and static P-wave modulus for EU2_01. There is a clear difference in the estimated values, which is expected. However, the trend is similar. Having that two independent methods of estimating the stiffness show similar trend, justifies the observations.
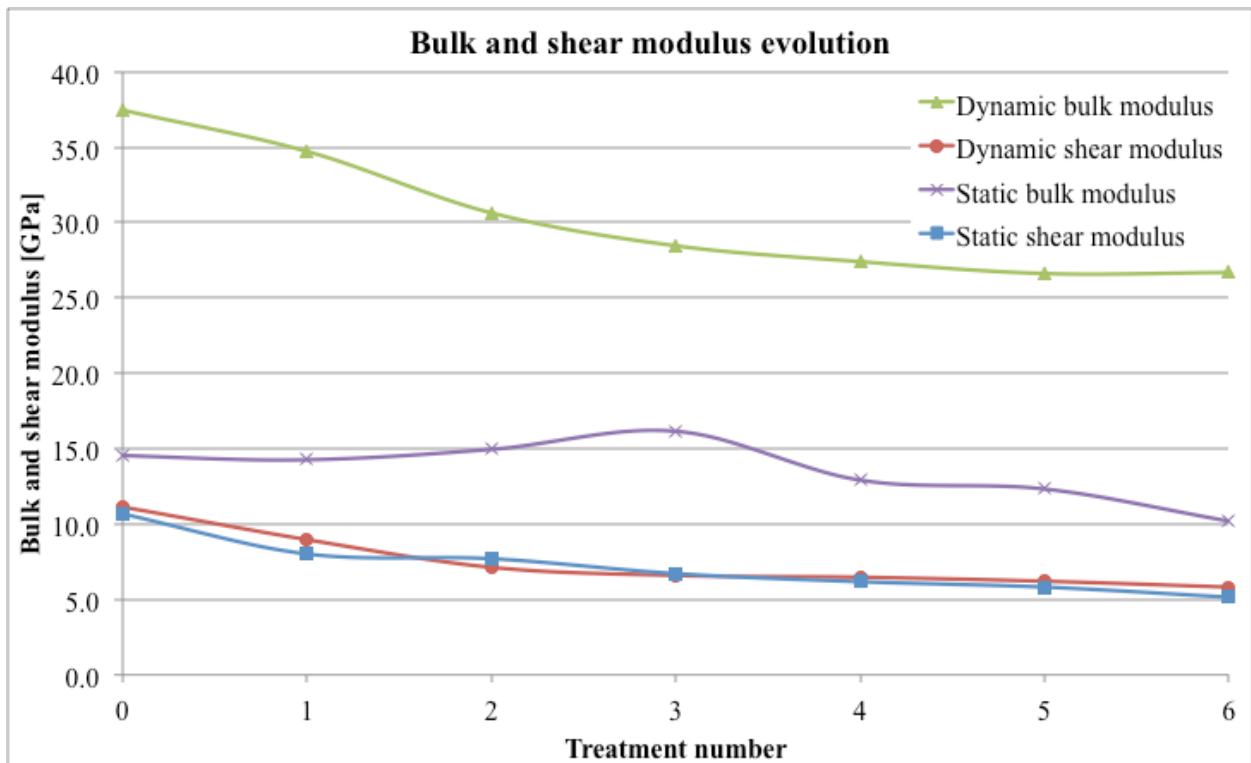
Figure 58: Static and dynamic bulk and shear modulus for EU2_01. Again, the trend lines show similarity to the static trend lines. The shear modulus has similar values for both static and dynamic, whereas the bulk modulus differs in the same range as the P-wave modulus.

Estimating the dynamic moduli is completely independent from the method of determining the static moduli. Although there are clear differences in the absolute values, seeing similar trends for both static and dynamic moduli strengthens the validity of the observations and results in terms of the stiffness evolution.

8.10.1　Reservoir surveillance

Reservoir surveillance becomes more and more important in reservoir management. Monitoring the reservoir can be beneficial for production optimization and very important in carbon capture and storage projects. Acoustic velocities can in theory be utilized for monitoring purposes. However, there are a significant number of factors affecting the velocities, thus understanding the correlation to the fullest is very difficult and requires a lot of study. Saturation is a general problem during seismic monitoring. It is very hard to determine and monitor the saturation levels in the reservoir. In addition, fluid is being substituted during injection, which could cause changes in the velocities. Whether the fluid has a significant effect on the velocities compared to what the change in stiffness has, can be assessed by applying Gassmann's model. Moduli obtained from velocities are valid for undrained condition. Gassmann's model takes the fluid effect into account and gives the drained dynamic modulus. Table 26 shows the dynamic bulk modulus for drained and undrained conditions, both before and after 6 RAT for EU2_01. It is here assumed a bulk modulus for the fluid of $K_f = 2$ GPa, and the grain modulus is set to the estimated value from the CNS loading during the experiment ($K_s = 57.5$ GPa). It is clear that the fluid effect is significantly smaller than the change induced by dissolution.

In conclusion, velocity changes during seismic monitoring of CCS projects could indicate that dissolution occurs. The change in stiffness moduli due to dissolution is significantly higher than what the fluid substitution effect is causing. The fluid effect is also bigger post to the experiment suggesting that the increase in fluid content has some minor influence. One should also note that despite taking the fluid effect into account, the dynamic bulk moduli is still close to a factor of 2 higher than the static moduli.

Table 26: The dynamic bulk modulus for drained and undrained conditions for EU2_01 prior and post to the experiment. Gassmann's model is applied for the fluid effects. There is only a small change in the modulus due to fluid effects.

Sample	Dynamic K_{fr} [GPa] prior		Dynamic K_{fr} [GPa] post	
	Undrained	Drained	Undrained	Drained
EU2_01	37	35	27	23

Although the S-waves are more difficult to assess in terms of first time arrival, observing that S-wave velocities changes could indicate that the shear modulus is changing. According to equation (40), S-waves are dependent of the shear modulus. The shear modulus is not affect by the fluid because the shear modulus for a fluid is zero. From the static measurements, we see that the shear modulus is affected by dissolution. In terms of seismic monitoring, S-waves could therefore also be used as a tool to assess the dissolution in the reservoir.

9.   Conclusion

The current project has performed experiments simulating long-term subsurface processes caused by acid-carbonate interaction. The results have been assessed and interpreted with the intension of investigating the effect that homogeneous dissolution of carbonate rock has on the rock mechanical properties. Strength and stiffness alteration have been assessed both from static and an acoustical point of view.

We have successfully established and verified an experimental protocol for achieving homogeneous dissolution and alteration of the core sample by using retarded acid. The protocol allows rock mechanical testing and assessment of acoustic properties of the core sample. Based on the interpretation of the results, the following conclusions have been drawn:

- Using a retarded acid allows for complete saturation of the core sample before any reaction takes place. Heating activates the acid, resulting in a strong chemical reaction in which homogeneous dissolution of the material is achieved. The established protocol still results in some channeling, which could indicate that this also would occur in the reservoir. Thus the altering of the rock achieved in the current project is considered to represent long-term subsurface processes that could occur in the reservoir during CO_2 storage.
- Enhanced dissolution is achieved by exposing the formation to more acid, implying a significant increase in porosity with a somewhat self-amplifying effect.
- The stiffness of the rock is significantly affected by the dissolution. Although stiffness and porosity is strongly related, at which high porosity implies softer rock, there is reason to believe that additional effects are causing the softening. This could be secondary porosity effects, or evolution of a different microstructure than seen through natural diagenesis, happening over several million years. In terms of reservoir consequences, softening could increase the possibility of compaction and surface subsidence.
- As a result of the porosity increase, the strength of the rock is also affected accordingly. It is evident that the porosity increase causes weakening of the rock. Comparing the failure line for the treated rock with the untreated reference indicates a significant decrease in the friction angle, and strength. Determining whether there are other affects in addition to the porosity increase requires a different test protocol.
- The acoustic properties of the reservoir rock show tendencies of being influenced by other effects, in addition to the porosity increase, as well. Deviation from the natural velocity-porosity trend is evident. These additional effects could be the same as for the stiffness alteration, suggesting secondary porosity or micro-pore scale alteration. The fluid substitution effect is insignificant compared to the effect caused by dissolution on the acoustic properties. These results are of great importance in terms of seismic monitoring of the reservoir and caprock integrity.
- More advanced imaging techniques, such as SEM analysis, are recommended for future studies in order to investigate if alteration of the rock mechanical properties on a micro-pore scale occurs, and understand the effects if present.

The established experimental protocol and the process of analyzing the data from the current project will be applied for future studies on real core material for Qatar. These studies will be an important step towards understanding and being able to store CO_2 in carbonates. The importance of the current project is seen through the workflow for assessing CCS projects.

Reservoir simulation and geochemical modeling estimates the amount of dissolved carbonate. The relationship between dissolved material and the strength, stiffness and acoustic properties is then determined, which has been the topic for the current project. These findings are important input parameters in geomechanical models for assessing reservoir and caprock integrity.

The current topic is new to the industry, thus a lot of research is still to be done. Having that the current project forms a basis for future studies; we recommend that more detailed studies should be performed, *i.e.* including more samples and also different types of carbonates with varying mineralogy.

Nomenclature

A	Area	[m^2]
a_0	Absorption	
C_0	Uniaxial strength	[GPa]
C_{eq}	Equilibrium concentration	[mol/l]
D	Diffusion constant	[m^2/s]
Da	Damköhler number	
E	Young's modulus	[GPa]
E_{stat}	Static Young's modulus	[GPa]
E_{dyn}	Dynamic Young's modulus	[GPa]
E_{fr}	Young's modulus for framework	[GPa]
f	Volume fraction	
G	Shear modulus	[GPa]
G_{fr}	Shear modulus of the framework	[GPa]
G_c	Shear modulus of the cement	[GPa]
G_s	Shear modulus of the grains	[GPa]
H	P-wave modulus	[GPa]
K	Bulk modulus	[GPa]
K_{fl}	Bulk modulus of fluid	[GPa]
K_s	Bulk modulus of the grains	[GPa]
K_{fr}	Bulk modulus of the framework	[GPa]
K_{stat}	Static bulk modulus	[GPa]
K_{dyn}	Dynamic bulk modulus	[GPa]
K_a	Permeability with respect to air	[Darcy]
L	Length	[m]
Pe	Péclet number	
p_f	Pore pressure	[MPa]
P_b	Atmospheric pressure	[Pa]
Q_b	Volumetric flow rate	[m^3/s]
S_0	Cohesion	[GPa]
T_0	Tensile strength	[GPa]
V_g	Grain volume	[m^3]
V_b	Bulk volume	[m^3]
V_p	P-wave velocity	[m/s]
$V_{p\text{-}grain}$	P-wave velocity	[m/s]
$V_{p\text{-}fl}$	P-wave velocity	[m/s]
V_s	S-wave velocity	[m/s]
v	Velocity	[m/s]
φ	Porosity	
φ_c	Critical porosity	
σ'	Effective stress	[MPa]
σ_N	Normal effectiv stress	[MPa]
σ_{rad}	Radial stress	[MPa]

σ_{ax}	Axial stress	[MPa]
σ_z	Stress along direction z	[MPa]
σ_1'	Highest effective principal stress	[MPa]
σ_2'	Second highest effective principal stress	[MPa]
σ_3'	Lowest effective principal stress	[MPa]
β	Failure angle	
ϕ	Friction angle	
μ	Coefficient of internal friction	
ρ	Density	[kg/m^3]
ρ_f	Fluid density	[kg/m^3]
ρ_s	Grain density	[kg/m^3]
τ	Shear stress	[MPa]
τ_{max}	Maximum shear stress	[MPa]
ε_z	Strain along direction z	[mStrain]
ε_{lat}	Lateral strain	[mStrain]
ε_{ax}	Axial strain	[mStrain]
ε_{vol}	Volumetric strain	[mStrain]
λ	Lame's parameter	[GPa]

References

[1]   Pachauri, R.K and Reisinger, A. (Eds.) (2007) '*Climate Change 2007: Synthesis Report*' IPPC, Switzerland.

[2]   Nakicenovic, N. and Swart, R. (Eds.) (2000) '*Emission Scenarios*' IPCC, United Kingdom: Cambridge University Press.

[3] CO_2 Capture Project$^®$ (2010) '*Annual Report 2010 – Preparing For Industrial Deployment*'.

[4]   Metz, B., Davidson, O., de Coninck, H., Loos, M. and Meyer, L. (2005) '*Carbon Dioxide Capture and Storage*' IPCC, United Kingdom: Cambridge University Press.

[5]   Kohl, A.L and Nielsen, R.B. (1997) '*Gas Purification*' 5th edn. Elsevier.

[6]   Skog, T. (2006) '*CO_2 – injeksjon på Sleipner*' Trondheim, Norway, November 17, 2006.

[7]   Kuuskraa, V. and Ferguson, R. (2008) '*Storing CO_2 with Enhanced Oil Recovery*' National Energy Technology Laboratory, the United States.

[8]   Kalfayan, L. (2008) '*Production Enhancement with Acid Stimulation*' 2nd edn. PennWell.

[9]   Bachu, S., Gunter, W.D. and Perkins, E.H. (1993) 'Aquifer Disposal of CO_2: Hydrodynamic and Mineral Trapping', *Energy Convers. Mgmt.,* 35(4), pp. 269 – 279.

[10]   Liro, C. R., Adams, E. E. and Herzog, H. J. (1992) 'Modeling the release of CO_2, in the deep ocean', *Energy Convers. Mgmt.,* 33(5-8), pp. 667 - 674.

[11]   Turkenburg, W.C. (1992) 'CO_2 Removal; Some Conclusions', *Energy Convers. Mgmt.,* 33(5-8), pp. 819 - 823.

[12]   Bachu, S., Bonijoly, D., Bradshaw, J., Burruss, R., Hollowaye, S., Christensen, N.P. and Mathiassen, O.M. (2007) 'CO_2 storage capacity estimation: Methodology and gaps', *International Journal of Greenhouse Gas Control*, 1, pp. 430 – 443.

[13]   Global CCS Institute (2011), 'The *Global Status of CCS: 2011*', Canberra, Australia.

[14]   United Nations Framework Convention on Climate Change.

[15]   United Nations (2008) *Kyoto Protocol to the United Nations Framework Convention on Climate Change*. Available at: http://unfccc.int/resource/docs/convkp/kpeng.pdf (Accessed January 4th 2012).

[16] http://www.lovdata.no/cgi-wift/wiftldles?doc=/usr/www/lovdata/all/nl-19901221-072.html&emne=utslipp*&

[17] http://www.lovdata.no/ltavd1/filer/sf-20111124-1154.html

[18] European Union (2008) *Opinion of the European Economic and Social Committee on the 'Communication from the Commission to the European Parliament, the Council, the European Economic and Social Committee and the Committee of the Regions on Supporting Early Demonstration of Sustainable Power Generation from Fossil Fuels'.* Available at: http://eur-lex.europa.eu/LexUriServ/LexUriServ.do?uri=OJ:C:2011:376:0092:0096:EN:PDF (Accessed January 4th 2012).

[19] CO_2 Capture Project®. Available at: http://www.co2captureproject.org/about_us/what_is_CCP.html (Accessed at: January 4th 2012).

[20] Bettelheim, F.A., Brown, W.H., Campbell, M.K. and Farrell, S.O. (2003), '*Introduction to General, Organic and Biochemistry*', Brooks/Cole.

[21] Eide, K. (2011), '*CO2 induced calcite dissolution in Euville carbonate rock: Formation of wormholes',* Rijswijk, The Netherlands.

[22] Zumdahl, S.S. (2009) '*Chemical Principles'.* Brooks/Cole

[23] Egermann, P., Bekri, S. and Vizika, O. (1995): "*An Integrated Approach to assess the petrophysical properties of rocks altered by rock/fluid interactions (CO_2 injection)*", Institut Français du Pétrole (IFP).

[24] Daccord, G., Touboul, E., Lenormand, R.: "Carbonate acidizing: toward a quantitative model of the wormholing phenomenon", SPE Production Engineering (February 1989), p. 63-68.

[25] Bemer, E. and Lombard, J.M. (2010), 'From Injectivity to Integrity Studies of CO_2 Geological Storage: Chemical Alteration Effects on Carbonates Petrophysical and Geomechanical Properties', *Oil & Gas Science and Technology,* 65(3), pp. 445 – 459.

[26] Holt, R.M., Fjær, E., Horsrud, P., Raaen, A.M., and Risnes, R. (2008) '*Petroleum Related Rock Mechanics'*, 2nd edn. Amsterdam: Elsevier.

[27] Bemer, E., Vincké, O. and Longuemare, P. (2004), 'Geomechanical Log Deduced from Porosity and Mineralogical Content', *Oil & Gas Science and Technology,* 59(4), pp. 405 – 426.

[28] Mavko, G., Mukerji, T. and Dvorkin, J. (1993) '*The Rock Physics Handbook: Tools For Seismic Analysis In Porous Media'*, 1st edn. Cambridge: Cambridge university Press.

[29] Nur, A., Mavko, G., Dvorkin, J., and Galmudi, D. (1998), 'Critical porosity: a key to relating physical properties to porosity in rocks'. *Leading Edge,* 17, pp. 357–362.

[30]   Lambe, T.W. and Whitman, R.V. (1969) *'Soil Mechanics'*, Massachusetts Institute of Technology, John Wiley & Sons, Inc.

[31]   King, M.S. (1970) '*Static and Dynamic Elastic Moduli of Rocks under Pressure*', The 11th U.S. Symposium on Rock Mechanics (USRMS), June 16 - 19, 1969, Berkeley, CA.

[32]   Ledbetter, H. (1993) '*Dynamic vs. static Young's moduli: a case study',* The 11th U.S. Symposium on Rock Mechanics (USRMS), June 16 - 19, 1969, Berkeley, CA, pp. 329 – 351.

[33]   Raymer, L.L., Hunt, E.R. and Gardner, J.S. (1980) *'An improved sonic transit time-to-porosity transform'*, SPWLA 21st Annual Logging Symposium, July 8 – 11, Lafayette, Louisiana.

[34]   Egermann, P., Bekri, S. and Vizika, O. (2005), '*An Integrated Approach to assess the petrophysical properties of rocks altered by rock/fluid interactions (CO_2 injection)*', Institut Français du Pétrole (IFP).

[35]   Eide, K. (2011), '*CO2 induced calcite dissolution in Euville carbonate rock: Formation of wormholes',* Rijswijk, The Netherlands.

[36]   Egermann, P., Bemer, E. and Zinszner, B. (IFP) (2006) '*An Experimental Investigation of the Rock Properties Evolution Associated to Different Levels of CO_2 Injection Like Alteration Processes',* International Symposium of the Society of Core Analysts, September 12th – 16th, 2006, Trondheim, Norway.

[37]   Bemer, E. and Lombard, J.M. (2010), 'From Injectivity to Integrity Studies of CO_2 Geological Storage: Chemical Alteration Effects on Carbonates Petrophysical and Geomechanical Properties', *Oil & Gas Science and Technology,* 65(3), pp. 445 – 459.

[38]   Nguyen, M.T., Bemer, E. and Dormieux, L. (IFP) (2011), '*Micromechanical modeling of carbonate geomechanical properties evolution during acid gas injection'*, 45th US Rock Mechanics/Geomechanics Symposium June 26th – 29th, 2011, San Francisco, CA.

[39]   ImageJ is a freeware developed at the National Institutes of Health by an employee of the Federal Government. The software is not subject to copyright protection.

Appendix

Contact information of contributors

Andreas Bauer, Sintef Petroleumsforskning
Location: Sintef Trondheim
Mobile: +47 93000192
E-mail: akm.bauer@gmail.com

Arjan van der Linden, Researcher, Shell Global Solutions International
Location: Shell Research Center Rijswijk
Mobile: +31 610973571
E-mail: Arjan.VanderLinden@shell.com

Holger Ott, Researcher, Shell Global Solutions International
Location: Shell Research Center Rijswijk
Mobile: +31 704473043
E-mail: Holger.Ott@shell.com

Fons Marcelis, Researcher, Shell Global Solutions International
Location: Shell Research Center Rijswijk
Mobile: +31 704472363
E-mail: Fons.Marcelis@shell.com

Carl van Rijn, Associate Research Technician, Shell Global Solutions International
Location: Shell Research Center Rijswijk
Mobile: +31 610972301
E-mail: Carl.Van-Rijn@shell.com

Ton Blok, Senior Associate Researcher, Shell Global Solutions International
Location: Shell Research Center Rijswijk
Mobile: +31 610972108
E-mail: Ton.Blok@shell.com

Properties

Sample ID	Length [mm]		Diameter [mm]		Bulk volume [cm³]		Weight [g]		Grain volume [cm³]		Pore volume [cm³]		Porosity	
	pre	post	pre	post	pre	post	pre	post	pre	post	pre	post	pre	post*
EU_06	76.28	76.28	37.94	37.93	86.24	86.19	191.758	189.448	71.99	71.64	14.25	14.58	16.5%	16.9%
EU2_01	76.15	76.15	37.88	37.87	85.82	85.77	189.519	180.649	71.34	68.64	14.48	17.10	16.9%	19.9%
EU2_02	76.11	76.11	37.89	37.89	85.82	NOT MEASURED	190.149	NOT MEASURED	71.59	NOT MEASURED	14.23	NOT MEASURED	16.6%	NOT MEASURED
EU2_03	76.12	76.12	37.91	37.91	85.92	NOT MEASURED	190.303	NOT MEASURED	71.68	NOT MEASURED	14.24	NOT MEASURED	16.6%	NOT MEASURED
EU2_05	75.71	75.71	37.87	37.87	85.28	NOT MEASURED	189.603	NOT MEASURED	71.32	NOT MEASURED	13.96	NOT MEASURED	16.4%	NOT MEASURED
EU2_07	75.87	75.87	37.98	37.98	85.95	NOT MEASURED	191.192	NOT MEASURED	72.00	NOT MEASURED	13.95	NOT MEASURED	16.2%	NOT MEASURED
EU2_08	75.87	75.87	37.98	37.98	85.95	NOT MEASURED	190.476	NOT MEASURED	71.73	NOT MEASURED	14.22	NOT MEASURED	16.5%	NOT MEASURED
EU2_09	75.72	75.72	37.96	37.96	85.69	NOT MEASURED	191.883	NOT MEASURED	72.25	NOT MEASURED	13.45	NOT MEASURED	15.7%	NOT MEASURED

*Measured from special core analysis

Effluent data

EU2_01

Effluent id	Ca²⁺ [mg/l]	Ca²⁺ [g]	CaCO₃ [g]	Sample size [ml]
Reference (Water)	51.1	0.003		55
1	1898.0	0.10	0.22	55
2	3660.4	0.20	0.44	55
3	6262.4	0.34	0.76	55
4	5830.5	0.32	0.7	55
5	5214.2	0.28	0.63	55
6	4668.0	0.25	0.56	55
Acid flooding	2212.9	0.12	0.29	55

EU2_02

Effluent id	Ca²⁺ [mg/l]	Ca²⁺ [g]	CaCO₃ [g]	Sample size [ml]
1	4100.99	0.22	0.54	55
2	5157.54	0.28	0.68	55
3	5567.51	0.30	0.74	55
4	5790.99	0.32	0.77	55
5	5832.99	0.32	0.77	55
6	5503.89	0.30	0.73	55

EU2_05

Effluent id	Ca²⁺ [mg/l]	Ca²⁺ [g]	CaCO₃ [g]	Sample size [ml]
1	4850.86	0.26	0.64	55
2	4725.22	0.26	0.63	55
3	4519.83	0.25	0.60	55
4	4550.46	0.25	0.60	55
5	5742.51	0.31	0.76	55
6	Spilled sample			

EU2_07

Effluent id	Ca²⁺ [mg/l]	Ca²⁺ [g]	CaCO₃ [g]	Sample size [ml]
1	3069.50	0.15	0.37	55
2	5993.80	0.30	0.72	55
3	6173.90	0.31	0.74	55
4	6381.20	0.32	0.77	55
5	5892.90	0.29	0.71	55
6	5730.60	0.28	0.69	55

Rock mechanical measurements

Dynamic properties are not available for EU_06 due to no velocity measurements and for EU2_05 after the 6th treatment.

Un denotes unloading cycle, Re denotes reloading cycle, Avg denotes the average, while Dyn denotes the dynamic moduli.

Young's modulus

Sample ID	Prior to treatment				1st treatment				2nd treatment				3rd treatment				4th treatment				5th treatment				6th treatment			
	Un	Re	Avg	Dyn	Un	Re	Avg	Dyn	Un	Re	Avg	Dyn	Un	Re	Avg	Dyn	Un	Re	Avg	Dyn	Un	Re	Avg	Dyn	Un	Re	Avg	Dyn
EU_06	18.5	20.8	19.6	NA	13.9	18.6	16.2	NA	11.6	16.7	14.2	NA	11.2	16.8	14.0						NA							
EU2_01	25.2	26.0	25.6	29.9	17.8	22.7	20.2	24.4	17.1	22.4	19.7	19.6	15.4	19.5	17.5	18.2	13.2	18.7	15.9	17.8	12.6	17.7	15.1	17.1	11.9	14.6	13.2	16.1
EU2_02	24.1	25.7	24.9	30.9	22.0	25.3	23.6	22.0	20.9	23.6	22.3	20.6	19.0	19.2	19.1	22.9	15.2	18.5	16.9	17.7	13.8	17.1	15.4	29.3	13.7	14.2	13.9	16.7
EU2_05	17.9	19.0	18.4	NA	14.5	16.3	15.4	29.9	14.0	14.6	14.3	28.8	12.8	14.8	13.8	27.5	12.0	14.1	13.1	20.7	11.5	13.0	12.3	18.5	7.8	9.5	8.7	NA
EU2_07	18.6	18.3	18.4	29.0	15.5	18.3	16.9	28.3	13.8	16.6	15.2	26.7	13.9	15.9	14.9	26.5	13.7	15.4	14.5	21.7	13.4	16.2	14.8	21.1	13.0	15.2	14.1	20.3

Poisson's ratio

Sample ID	Prior to treatment				1st treatment				2nd treatment				3rd treatment				4th treatment				5th treatment				6th treatment			
	Un	Re	Avg	Dyn	Un	Re	Avg	Dyn	Un	Re	Avg	Dyn	Un	Re	Avg	Dyn	Un	Re	Avg	Dyn	Un	Re	Avg	Dyn	Un	Re	Avg	Dyn
EU_06	0.20	0.09	0.15	NA	0.21	0.23	0.22	NA	0.32	0.14	0.23	NA	0.29	0.16	0.23						NA							
EU2_01	0.19	0.20	0.20	0.34	0.30	0.22	0.26	0.36	0.31	0.25	0.28	0.38	0.37	0.24	0.30	0.38	0.33	0.26	0.29	0.37	0.33	0.26	0.30	0.38	0.32	0.25	0.28	0.38
EU2_02	0.20	0.22	0.21	0.37	0.28	0.28	0.28	0.38	0.30	0.28	0.29	0.37	0.36	0.24	0.30	0.34	0.32	0.27	0.29	0.38	0.30	0.28	0.29	0.18	0.32	0.27	0.29	0.36
EU2_05	0.18	0.19	0.18	0.31	0.22	0.20	0.21	0.30	0.30	0.19	0.25	0.30	0.28	0.24	0.26	0.30	0.26	0.25	0.26	0.36	0.28	0.25	0.26	0.37	0.37	0.30	0.33	NA
EU2_07	0.11	0.11	0.11	0.33	0.15	0.15	0.15	0.32	0.18	0.16	0.17	0.32	0.22	0.17	0.20	0.32	0.23	0.18	0.21	0.35	0.25	0.24	0.24	0.35	0.28	0.25	0.26	0.35

Bulk modulus (calculated)

Sample ID	Prior to treatment				1st treatment				2nd treatment				3rd treatment				4th treatment				5th treatment				6th treatment			
	Un	Re	Avg	Dyn*	Un	Re	Avg	Dyn*	Un	Re	Avg	Dyn*	Un	Re	Avg	Dyn*	Un	Re	Avg	Dyn*	Un	Re	Avg	Dyn*	Un	Re	Avg	Dyn*
EU_06	10.2	8.5	9.3	NA	8.0	11.4	9.6	NA	10.8	7.7	8.7	NA	8.9	8.3	8.6						NA							
EU2_01	13.6	14.7	14.1	37.4	15.0	13.6	14.2	34.7	15.0	15.0	15.0	30.6	19.9	12.4	14.9	28.5	12.9	12.9	12.9	27.4	12.2	12.5	12.4	26.6	10.8	9.7	10.1	26.7
EU2_02	13.6	15.4	14.5	36.8	16.9	19.3	18.1	34.4	17.3	18.2	17.8	31.5	22.4	12.5	16.0	28.3	13.9	13.2	13.5	28.2	11.6	13.2	12.4	22.7	12.4	10.4	11.3	23.5
EU2_05	9.2	10.2	9.7	34.2	8.6	9.2	8.9	31.8	11.5	8.0	9.4	30.0	9.5	9.3	9.4	28.8	8.5	9.5	9.0	29.2	8.7	8.6	8.7	28.4	9.8	7.8	8.6	NA
EU2_07	7.9	7.9	7.9	34.2	7.3	8.8	8.1	32.9	7.2	8.3	7.8	30.8	8.4	8.1	8.2	30.5	8.5	8.1	8.3	28.9	8.8	10.6	9.7	28.0	9.6	10.0	9.8	26.6

*Undrained

Bulk modulus (measured)

Sample ID	Prior to treatment			1st treatment			2nd treatment			3rd treatment			4th treatment			5th treatment			6th treatment		
	Un	Re	Avg	Un	Re	Avg	Un	Re	Avg	Un	Re	Avg	Un	Re	Avg	Un	Re	Avg	Un	Re	Avg
EU_06										*Not measured*											
EU2_01	3.6	5.3	4.4	3.2	4.6	3.9	3.5	5.3	4.4	3.2	4.3	3.8	3.0	4.5	3.7	3.0	4.5	3.7	2.8	4.0	3.4
EU2_02	5.0	4.3	4.6	4.5	4.5	4.5	3.3	4.7	4.0	3.3	4.6	3.9	3.1	4.5	3.8	3.0	4.6	3.8	2.9	4.2	3.6
EU2_05	3.4	3.9	3.7	3.3	3.6	3.4	3.2	3.4	3.3	3.0	3.5	3.2	3.0	3.6	3.3	3.5	3.3	3.4		NA	
EU2_07	3.8	4.3	4.1	3.4	4.1	3.8		NA		6.5	1.6	4.1	3.6	4.3	3.9	3.1	4.1	3.6	2.6	3.5	3.1

Shear modulus

Sample ID	Prior to treatment				1st treatment				2nd treatment				3rd treatment				4th treatment				5th treatment				6th treatment			
	Un	Re	Avg	Dyn	Un	Re	Avg	Dyn	Un	Re	Avg	Dyn	Un	Re	Avg	Dyn	Un	Re	Avg	Dyn	Un	Re	Avg	Dyn	Un	Re	Avg	Dyn
EU_06	7.7	9.5	8.6	NA	5.7	7.6	6.7	NA	4.4	7.3	5.8	NA	4.3	7.2	5.7						NA							
EU2_01	10.6	10.8	10.7	11.2	6.8	9.3	8.0	9.0	6.5	9.0	7.7	7.1	5.6	7.9	6.7	6.6	5.0	7.4	6.2	6.5	4.8	7.0	5.8	6.2	4.5	5.8	5.2	5.8
EU2_02	10.0	10.5	10.3	9.1	8.6	9.9	9.2	8.0	8.1	9.2	8.6	7.5	7.0	7.7	7.3	8.6	5.8	7.3	6.5	6.4	5.3	6.7	6.0	12.4	5.2	5.6	5.4	6.2
EU2_05	7.6	8.0	7.8	11.8	6.0	6.8	6.4	11.5	5.4	6.1	5.8	11.1	5.0	6.0	5.5	10.6	4.7	5.6	5.2	7.6	4.5	5.2	4.9	6.7	2.8	3.7	3.2	NA
EU2_07	8.4	8.2	8.3	10.9	6.7	8.0	7.3	10.7	5.9	7.1	6.5	10.1	5.7	6.8	6.2	10.0	5.5	6.5	6.0	8.0	5.4	6.5	6.0	7.8	5.1	6.1	5.6	7.6

P – wave modulus

Sample ID	Prior to treatment		1st treatment		2nd treatment		3rd treatment		4th treatment		5th treatment		6th treatment	
	Static	Dynamic	Static	Dynamic	Static	Dynamic	Static	Dynamic	Static	Dynamic	Static	Dynamic	Static	Dynamic
EU2_01	22.5	45.8	20.3	41.4	20.7	36.0	21.2	33.4	17.6	32.3	16.7	31.3	14.1	31.1
EU2_02	22.2	43.6	25.0	40.4	24.2	37.1	22.9	34.7	18.4	33.0	16.9	32.0	15.5	28.1
EU2_05	15.9	43.1	14.3	40.4	14.5	38.3	13.8	36.8	13.0	34.9	12.2	33.5	10.7	NA
EU2_07	14.0	42.4	13.5	40.9	12.6	38.4	12.7	38.0	12.8	34.9	14.1	33.8	14.0	32.2

Permeability

Sample ID	Prior to treatment		1st treatment	2nd treatment	3rd treatment	4th treatment	5th treatment	6th treatment	Post
	Isostatic	In situ	In situ	In situ	In situ	In situ	In situ	In situ	Isostatic
EU_06	190.0	92.9	189.8	247.3	280.1		NA		2750.0
EU2_01	266.0	114.9	127.0	125.8	74.2	166.5	300.8	261.7	2798.0
EU2_02	322.0	121.1	105.0	104.8	127.0	124.6	172.6	252.2	NA
EU2_05	267.0	99.0	53.0	NA	123.0	176.0	97.0	NA	
EU2_07	259.0	92.9	76.3	87.3	132.2	302.0	245.5	300.4	

Strength

Sample ID	Porosity	Failure effective stress [MPa]			Peak Deviatoric Eff. Stress [MPa]	q [MPa]	p' [MPa]	Treatments
		Axial	Radial	Mean*				
EU2_02	0.162	25.61	4.65	11.64	20.96	10.48	15.13	6
EU2_03	0.166	54.12	9.99	24.70	44.13	22.07	32.06	0
EU2_05	0.164	19.16	0.00	6.39	19.16	9.58	9.58	6
EU2_07	0.162	30.99	9.45	16.63	21.54	10.77	20.22	6
EU2_08	0.165	28.96	0.98	10.31	27.98	13.99	14.97	0
EU2_09	0.157	26.07	0.00	8.69	26.07	13.04	13.04	0